The Nanogate: Nanoscale Flow Control

by

James R. White

B.A.Sc., Engineering Physics
University of British Columbia, 1998

SUBMITTED TO THE DEPARTMENT OF MECHANICAL ENGINEERING
IN PARTIAL FULFILLMENT OF THE DEGREE OF

DOCTOR OF PHILOSOPHY

at the

MASSACHUSETTS INSTITUTE OF TECHNOLOGY

May 8, 2003

Signature of Author .....
Department of Mechanical Engineering
May 8, 2003

Certified by .....
Professor Alexander H. Slocum
Thesis Supervisor

Accepted by .....
Professor Ain A. Sonin
Chairman, Department Graduate Committee

The Nanogate: Nanoscale Flow Control

by

James R. White

Submitted to the Department of Mechanical Engineering
on May 8, 2003 in Partial Fulfillment of the
Requirements for the Degree of Doctor of Philosophy
at the Massachusetts Institute of Technology

ABSTRACT

The handling of extremely small samples of gases and liquids has long been a subject of research among biologists, chemists and engineers. A few scientific instruments, notably the atomic force microscope and the surface forces apparatus, have been used extensively to investigate very short range molecular phenomena. In this thesis, the design, fabrication and characterization of a novel gas and liquid flow control device called the Nanogate is described. The Nanogate controls liquid flows under very high confinement, wherein the liquid film is, in one dimension, on the scale of nanometers, but is on the scale of hundreds of microns in its other dimensions. The film thickness can be controlled within two Angstroms. Control of helium gas flow rates in the 10^{-9} atm.cc/s range, and sub-nl/s flow rates of water and methanol have been theoretically predicted and experimentally verified. However, these results do not reflect the ultimate limits of the current device, but rather the limitations of the test apparatus. It is predicted that control of flow rates two orders of magnitude smaller can ultimately be achieved. The Nanogate has been successfully produced using standard MEMS techniques. This parallel fabrication process lays the foundation for mass-produced scientific instruments based on the Nanogate. Applications in ultra-fine flow control, gas and liquid separations, and a broad range of experiments with highly confined liquid systems can now be envisioned.

Thesis Supervisor:
Prof. Alexander H. Slocum
Department of Mechanical Engineering

ACKNOWLEDGMENTS

Funding for this research was provided by the National Science Foundation under grant DMI-002394. The author thanks the Fannie and John Hertz Foundation for its generous support. Also, Dennis Ward, Kurt Broderick, and Paul Tierney of MTL, for their tireless assistance in the MTL cleanroom facility. Paudley Zamora, for generously allowing the loan of MTL's Helium Leak Tester for testing of the Nanogate. Hong Ma, who was invaluable in assisting with fabrication and testing of the MEMS Nanogates. Alex Slocum, who inspired the entire project and maintained the author's focus and drive.

Chapter 1

INTRODUCTION

1.1 Motivation

The handling of extremely small samples of gases and liquids has long been a subject of research among biologists, chemists and engineers. Numerous micro-scale techniques [Senturia, 2001] have now been developed to miniaturize conventional processes such as chromatography, separations, and process control. These micro-electromechanical systems (MEMS) typically operate on the length scale of microns to hundreds of microns. Some applications that are entering wider use are micro-electrophoresis systems [Harrison, 1993], micro valves e.g. [Henning, 1997] and [Dubois, 2001], and pumps [Maillefer, 1999]. All of these systems are, for the most part, a miniaturization of an existing conventional mechanism.

At molecular length scales, which are understood to be on the order of nanometers, the physics of fluid flows are substantially altered. For example, in the case of a gaseous mixture flowing in a narrow channel or slit, molecules of different molecular weights flow at different speeds, and this effect can be used to separate gases akin to the separation column in a gas chromatograph. In a fluid system with a very high surface area to volume ratio, the interaction of a molecule or particle with the wall will heavily influence its mobility. For example, solidification, wherein the fluid viscosity increases beyond its bulk value, has been observed using the surface force apparatus, with simple liquids confined between mica sheets separated by less than ten molecular dimensions [Demirel, 2001] and

[Chen, 1985]. Slip flow, where the fluid viscosity appears to decrease below its bulk value, has been observed, again with the surface force apparatus, in non-degassed liquids (both polar and non-polar) between non-wetting mica surfaces, even at relatively large separation distances of 50 nm [Zhu, 2001]. These effects were observed to disappear with increasing surface roughness [Zhu, 2002]. However, the surface force apparatus is not an ideal mechanism for studying fluid flows since it is an indirect approach where the viscosity is inferred from the measurement of surface forces acting over an area that is not precisely defined. An ideal apparatus for verifying these results would allow direct control of the plate separation, a well-defined interaction area, and a direct measurement of the fluid flowrate.

In addition, with a slit of sufficiently small dimensions, one can reasonably conceive of excluding particles based solely on their size. By making the slit height adjustable, a wide range of molecule sizes can be filtered without the loss of larger particles that is characteristic of a conventional porous filter. More generally, one can conceive of mechanically filtering a solution of unknown composition, particle by particle, or introducing minute, well-controlled quantities of liquid or gas into a chemical or biological process. A mechanical filter that operates in this manner would have applications in processes such as drug discovery, where the manipulation of extremely small quantities of liquid is required. The design challenge, then, is to create an adjustable device that can confine liquid flows on nanometer length scales.

A study of manufacturing processes reveals that etched and machined surfaces typically have roughness on the order of hundreds of nm, and, similarly, feature contour and straightness on the order of microns. In comparison, flat surfaces, which are simple to manufacture, can readily have nanometer-scale flatness and surface finish! Nanometer surface finishes can be inexpensively obtained in the form of silicon wafers, glass wafers and optical flats, to name a few. Mounting two polished surfaces in close proximity creates a very long, nanometer-high slit or aperture. Accordingly, a platform technology of "Ultra Surface Finish Effect Mechanisms" (USFEMs) based on this principle has been

proposed [Slocum, 1999]. In a USFEM device, the minimum size of the aperture is limited only by the roughness and local bow and warp of the two opposed surfaces. In a slit with a very large aspect ratio of height to length, (here, greater than 10^5), surface forces strongly influence the liquids that are flowing. Molecules inside the slit find themselves confined between two plates of almost infinite extent in all directions. Therefore the surface chemistry, planarity and roughness can have a disproportionate effect on fluid flow properties.

The Nanogate is a fundamental embodiment of a USFEM mechanism. It incorporates two parallel, polished, ultra-flat surfaces, several hundred microns in diameter, and a flexure and fulcrum mechanism to control their separation. The flexure structure acts as a mechanical transmission, and translates the (relatively) coarse motion of the actuator assembly into fine control over the plate separation. In a sense, the Nanogate acts as a lever, in a linear or circular form. Displacement information is provided by optical interferometry.

The Nanogate is manufactured using conventional MEMS etching and bonding technologies. The flexure and fulcrum structure are etched from a silicon wafer using the Bosch Deep Reactive Ion Etch (DRIE) process. The valve land is then coated with a thin layer of gold, and the finished silicon wafer is anodically bonded to a bare Pyrex wafer with machined interconnection holes. The gold layer prevents bonding in the region where it is applied, and no additional release steps are required after bonding.

This parallel manufacturing approach produces integrated nanoscale fluidic systems with virtually arbitrary interconnections. The ability to add electrical interconnections to this process will also be fundamental to producing integrated scientific instruments.

The Nanogate is packaged by anodically bonding the silicon and glass wafer stack to a polished, machined Pyrex die. Kovar tubes with Swagelok™ connectors are then bonded to the large Pyrex die using a leak sealant epoxy with minimal outgassing in high vacuum. This large, rigid base provides robust, standard connections to external apparatus such as syringe pumps, or high vacuum equipment. The package can be pumped down to 10^{-7} torr,

or pressurized to over 100 psi without any adverse effect. Furthermore, it can be heated to 200 °C without damage.

1.2 Basic Principle

In its initial, undeflected state, the central beam (flexure) seals the Nanogate and does not allow fluid to pass between the inlet and outlet chambers. This is shown in Figure 1.1.

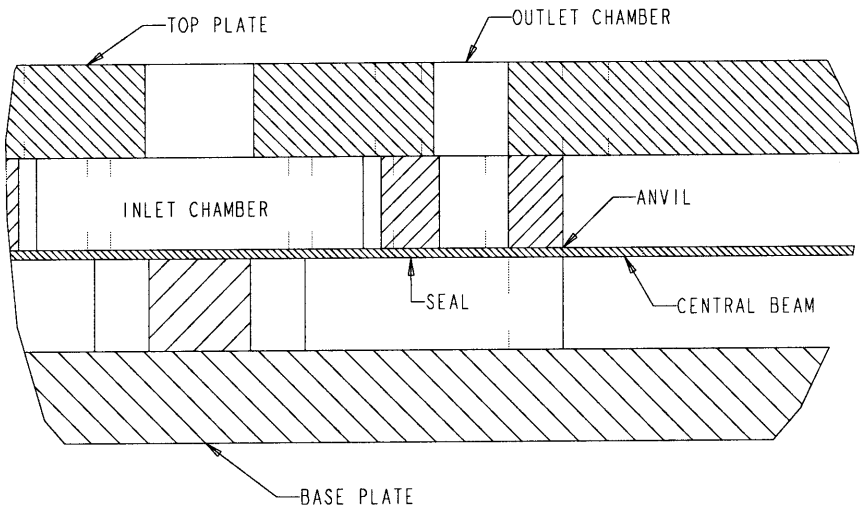

Figure 1.1 Section View - Undeflected

Applying an upward deflection to the end of the central flexure causes it to bend about the anvil, thereby opening a tiny gap between the inlet and outlet chambers. This is the fundamental operating mode of the Nanogate, shown in Figure 1.2.

In another operating mode, a downward deflection is applied to the end of the Nanogate flexure. This opens a significantly larger gap, which could be used for flushing contaminants through the device, as shown in Figure 1.3.

The transmission ratio of the flexure is determined by its geometry. The smallest theoretical opening is determined by the smallest possible movement of the actuator, divided by

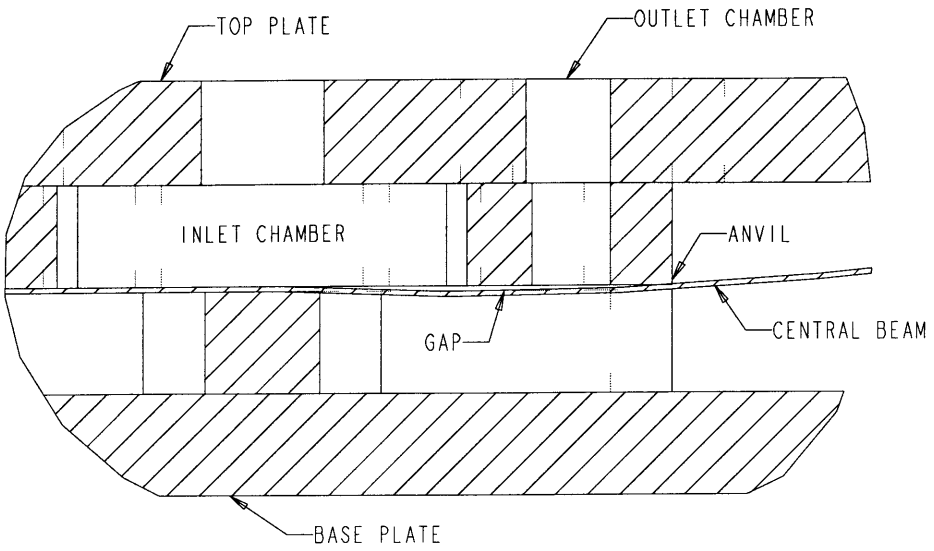

Figure 1.2 Section View - Filtering

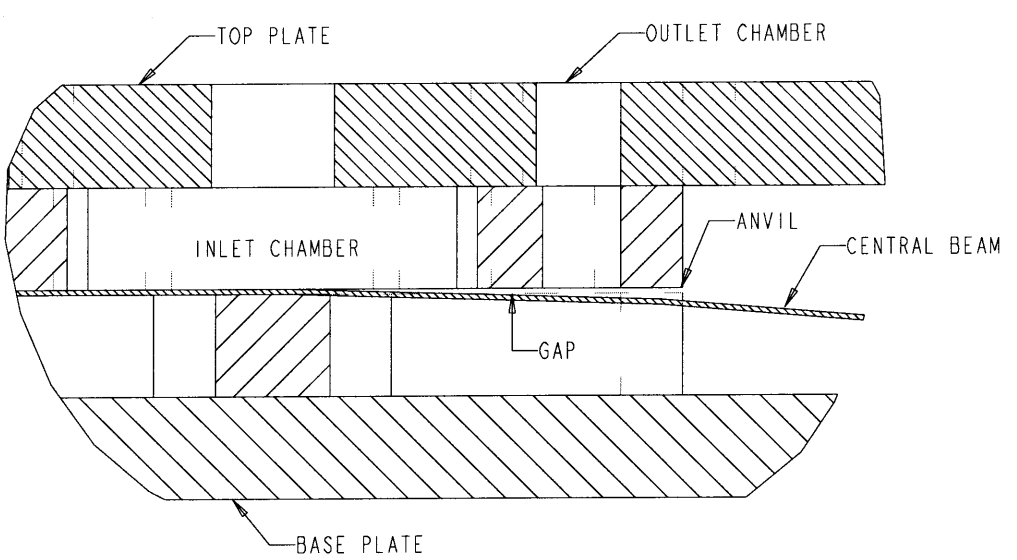

Figure 1.3 Section View - Flushing

the transmission ratio. Therefore, the transmission ratio should be as high as possible, but it is limited by the necessity to include metrology devices and flow connections of finite size. The dynamic range of the device is limited by the yield stress of the flexure; a device with a high transmission ratio will ultimately sacrifice dynamic range. In the limit of

extremely small sub-nanometer openings, effects such as surface tension, van der Waals forces and surface forces (falling off rapidly) come into play. These effects would ultimately limit the smallest possible opening in the case where surface roughness and flatness were of sufficient quality to permit it. The closest approach of the flexure and valve land is dictated by contact between asperities in the mating surfaces. In the current implementations of the Nanogate, this is approximately 5 nm rms due to plastic deformation of the Pyrex valve seat during bonding.

Chapter 2

BACKGROUND

2.1 Gas Flow

It is well known that the Navier-Stokes equations governing gas flow do not adequately model flows at low pressures or at very small length scales. The ratio of the mean free path to the characteristic length, the Knudsen number, gives a quantifiable indication of when a correction to Navier Stokes is required. The Knudsen number is:

$$Kn = \frac{\lambda}{L}, \tag{2.1}$$

where λ is the mean free path of the gas (a function of pressure, shown in Figure 2.1), and L is the height of the gap. The mean free path is calculated by:

$$\lambda = \frac{1}{\sqrt{2}\pi d^2 \rho_n}, \tag{2.2}$$

where d is the diameter of the molecule and ρ_n is the density (N/V, the number of molecules per unit volume). For example, at Knudsen numbers between 0.01 and 0.1, a higher-level approximation to the no-slip boundary condition is required. This is the slip-flow regime, and is of interest to MEMS microchannel designers. The conductance of a long, thin rectangular channel, with the slip boundary condition applied at the wall, was modeled by [Arkilic, 1997]:

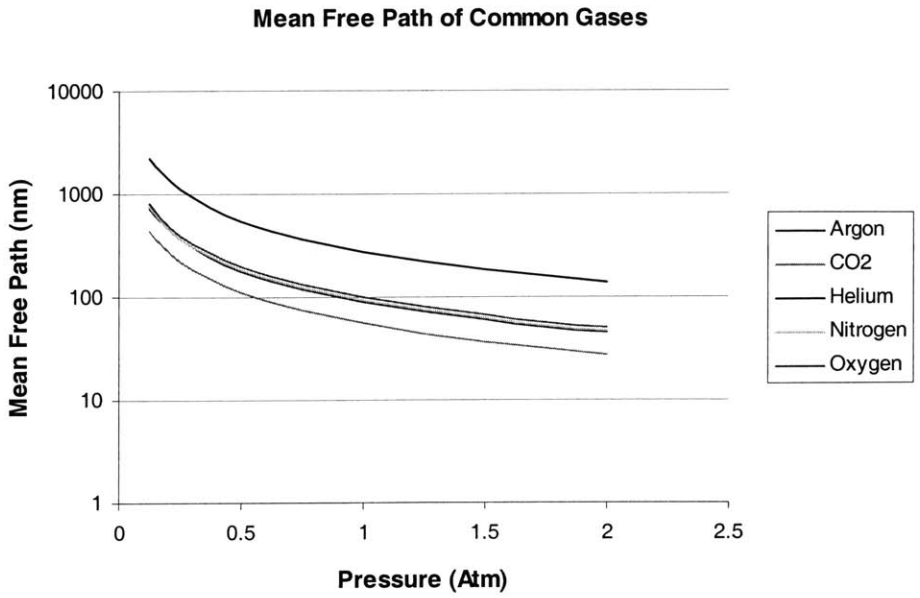

Figure 2.1 Mean free path as a function of pressure for common gases.

$$\frac{\dot{m}}{\Delta P} = \frac{wt^3}{12\mu LRT}\bar{P} + \frac{wt^3}{2\mu LRT}\left(\frac{2-\sigma_m}{\sigma_m}\right)K_o P_o, \tag{2.3}$$

where σ_m is an empirical quantity called the tangential momentum accommodation coefficient which describes the fraction of momentum transferred between the gas and the walls of the channel at a given pressure ratio. Typical values are 0.8 for argon and 0.88 for nitrogen [Arkilic, 1997]. The channel width is w, height t, length L, R is the ideal gas constant, T is temperature, $\bar{P}$ is the average pressure in the channel, μ is viscosity, K_0 and P_0 are the Knudsen number and pressure at the channel outlet. Interestingly, as the flow undergoes a transition from molecular flow to slip flow, there is a minimum in the curve of conductance vs. pressure. This minimum is determined experimentally [Loeb, 1934].

Beyond slip-flow is a transition flow region (Kn > 0.1), where the higher-order boundary conditions for Navier-Stokes equations are no longer valid, and the Boltzmann transport equation governs the flow. This is the region in which the Nanogate will operate.

At very high Knudsen numbers (Kn > 1), the flow is governed by the Boltzmann transport equation. The conductance of the slit then approaches a constant for each different molec-

ular species. Various techniques for approximating the flow in this regime have been demonstrated. However, limited experimental investigations have been performed, due to device constraints. In particular, experiments involving the flow of gases at atmospheric pressure, through nanometer sized channels, are of interest in this case.

For large Knudsen numbers, where the mean free path is comparable to the size of the chamber, one assumes that the molecules do not interact with each other. This leads to Knudsen's equation for molecular flow [Loeb, 1934]:

$$Q_t = \frac{p_1 - p_2}{\sqrt{\rho_1} W}. \tag{2.4}$$

Here,

$$W = \frac{3}{8}\sqrt{\frac{\pi}{2}}\int_0^L \frac{O}{A^2} dl, \tag{2.5}$$

where O is the perimeter and A is the cross-sectional area of the flow geometry, and

$$\rho_1 = \frac{p}{\rho}, \tag{2.6}$$

where ρ is the density and p is pressure. Assuming a torodial geometry, as in Figure 2.3, the shape factor W is:

$$W = \frac{3}{8}\sqrt{\frac{\pi}{2}}\left[\frac{1}{\pi t^2}\ln\left(\frac{r_p + t}{r_p}\right) + \frac{1}{2\pi^2 t}\left(\frac{1}{r_p} - \frac{1}{r_p + t}\right)\right] \tag{2.7}$$

The $1/t^2$ term is dominant for the Nanogate since t, the gap height, is very small. Thus, the flowrate is proportional to t^2. The flowrate sof helium and nitrogen as a function of the gap opening were calculated for molecular flow conditions, as shown in Figure 2.2. For example, for a gap of 10 nm, the flowrate of Helium is 9×10^{-9} atm.cc/s at room temperature.

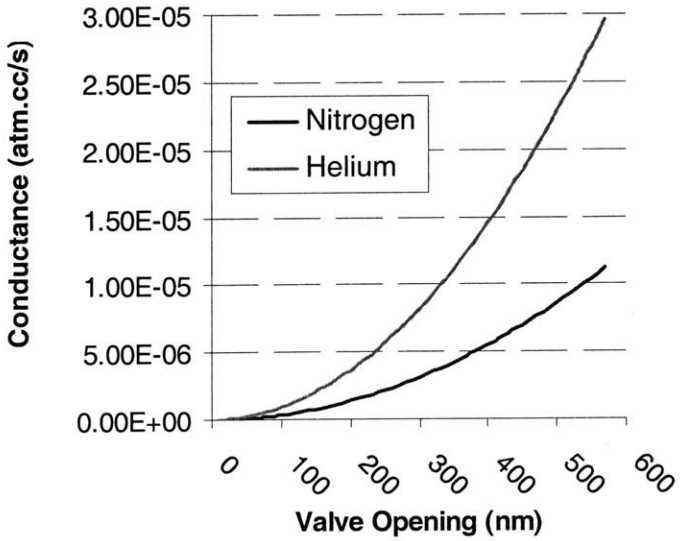

Figure 2.2 Calculated conductance for nitrogen and helium in the molecular flow regime.

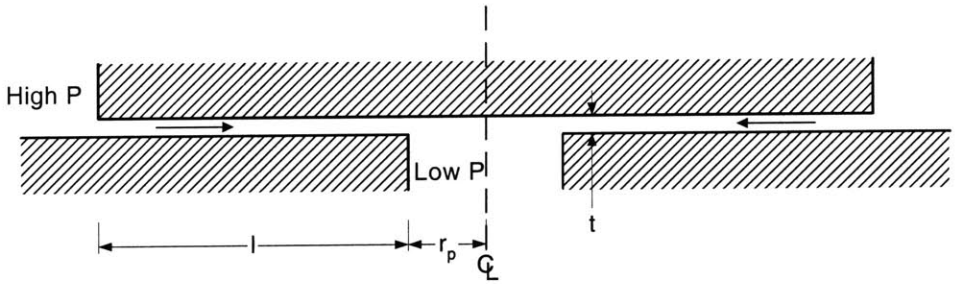

Figure 2.3 Schematic of toroidal flow regime in Nanogate.

The third region of fluid flow is simply Stokes' flow (Kn < 0.01), which is a solution of the Navier-Stokes equations with a no-slip boundary condition. The conductance in this region is:

$$\frac{\dot{m}}{\Delta P} = \frac{wt^3}{12\mu LRT}\bar{P}, \tag{2.8}$$

in the case of a rectangular geometry.

2.2 Liquid Flow

The flow of liquids through the Nanogate is also of interest. Here, the flow is easily modeled as Stokes flow. However, the effects of surface tension and wetting cannot be neglected i.e. if a fluid is non-wetting, it must be forced through the microchannel at high pressure. The flowrate is given by (2.9):

$$\dot{Q} = \frac{\pi t^3}{6\mu} \ln\left(\frac{r_p + l}{r_p}\right)(p_2 - p_1) \tag{2.9}$$

Therefore, the mass flow rate has the characteristic t^3 dependence of slip flow. At extremely small length scales, on the order of the intra-molecular distance in a fluid, quantized fluid flow has been observed, particularly in atomic force microscopy (AFM) experiments in organic solvents on graphite surfaces [Lindsay, 2000]. Fluid flow at extremely short length scales is an area of interest for further study, i.e. 'nano-rheology'.

In liquids, the intermolecular spacing is substantially smaller than in a gas, typically on the order of a few angstroms, or a few nanometers in the case of a large organic solvent (e.g. benzene). However, in special cases, with non-wetting walls, and some non-degassed liquids, slip flow can be observed in a channel on the order of tens of nm [Granick, 2001; Granick, 2000]. In other cases, in particular when the fluid is confined to a channel with a height of less than eight molecular diameters [Chen, 1985], phase transitions and a subsequent increase in viscosity due to (presumed) short-range ordering of the liquid have been observed. However, these effects disappear at the larger length scales and higher roughnesses that are present in the Nanogate.

Chapter 3

DESIGN

The Nanogate's purpose is the control of a long, wide, nanometer-scale slit with sub-nm precision, using the principle of an "ultra surface finish effect mechanism." A wide range of geometries and manufacturing techniques can be conceived of which will satisfy this requirement. More specifically, the functional requirements are summarized in Table 3.1.

TABLE 3.1 Functional Requirements

Functional requirements	Design parameters	Physics
Open sub-nanometer gap	- flexure transmission ratio - actuator resolution	At lower limit, van der Waals forces, and surface tension limit smallest approach.
Robust vacuum seal	- elastic sealing layer - high Hertz contact stresses - fine surface polish and flatness.	Relative stiffness of flexure and sealing layer. Valve land geometry Flatness and polish, closest approach.
Nanometer resolution metrology	- Metrology equipment - Fixturing and enclosures.	Interferometry or capacitance. Isolation from thermal gradients, vibration and air currents.

The design space that was considered here can be broadly categorized by geometry, assembly technique and size. Initially, a Nanogate mechanism with a square flexure ele-

ment was proposed, as in Figure 3.1. Then, a circularly symmetric mechanism as in

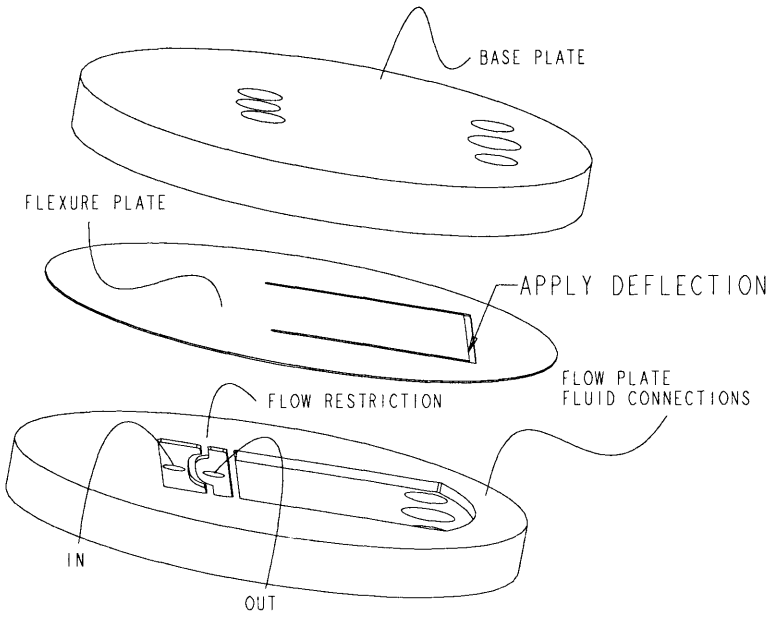

Figure 3.1 Macroscopic Nanogate with Square Flexure

Figure 3.2 was developed to counter some of the anticipated design shortcomings of the square Nanogate. The initial, macroscopic Nanogates used plates and flexures which were separable to preserve expensive machined and polished glass parts in the (likely) event that the flexure failed in some capacity. This then dictated the use of disposable flexure elements, such as a silicon wafer, and required that the flexure not be irreversibly bonded to the glass plate, as shown in Figure 3.4. However, a shift to MEMS manufacturing techniques, where the final devices are mass-produced, in parallel, opened the possibility of using a bonded, flexible fulcrum structure as in Figure 3.3. The final design of the Nanogate represents the culmination of extensive development which ultimately generated a tremendous improvement in the performance, manufacturability, and isolation of the Nanogate from its environment. A summary of the three designs that will be discussed in detail is given in Table 3.2.

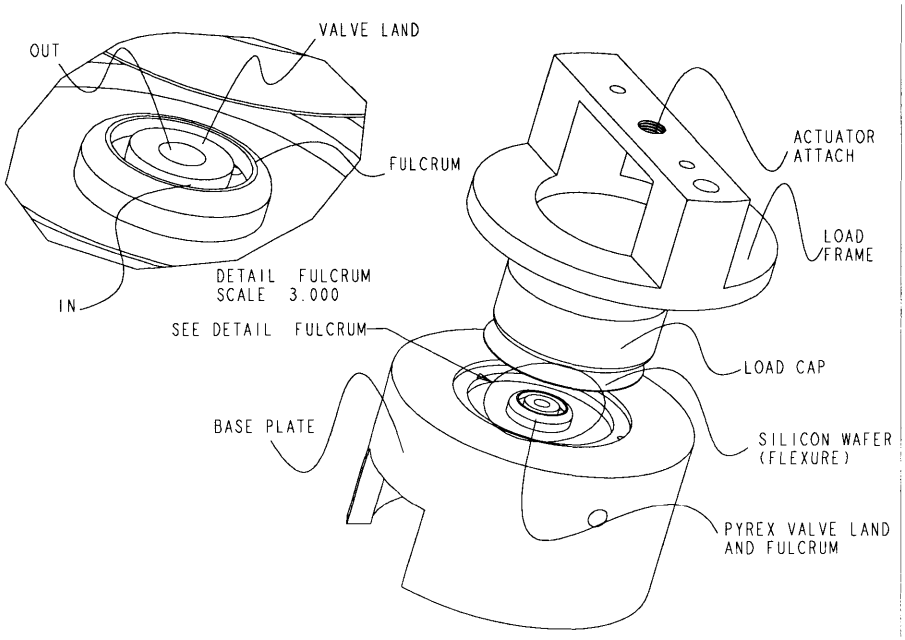

Figure 3.2 Circularly Symmetric Nanogate (Free Fulcrum)

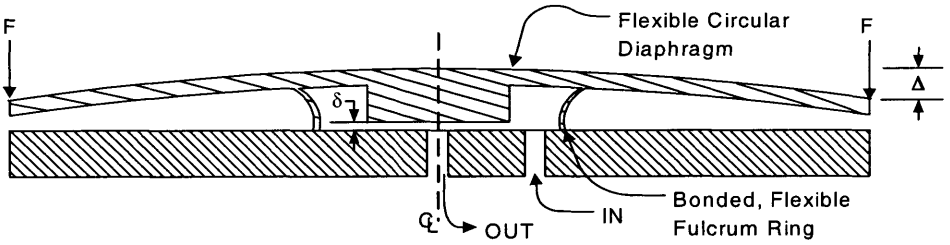

Figure 3.3 Bonded, circularly symmetric MEMS Nanogate concept.

TABLE 3.2 Summary of Detailed Design Cases

Case #	Flexure Shape	Fulcrum Type	Scale
1	Square	Free, rigid	Macro
2	Round	Free, rigid	Macro
3	Round	Bonded, flexible	Micro

3.1 Case 1: Square, Free, Macroscopic

The first proposed embodiment of the Nanogate was a macroscopic, square "paddle" geometry with line contact between the fulcrum and the flexure as shown in Figure 3.4 [Slocum, 1999]. The flexure is thereby free to rotate about the rigid fulcrum, which imposes no bending moment on the flexure. This is to be distinguished from future designs where the flexure and fulcrum were rigidly bonded, and the fulcrum structure is flexible in bending. The valve land structure was curved (note the 'flow restriction' in Figure 3.1) to conform to iso-displacement curves determined by finite element analysis, thereby guaranteeing a uniform aperture across the width of the device. The transmission ratio of the device could be designed by positioning the valve land appropriately with respect to the fulcrum.

Two modes of operation were possible with this design. The first was a 'filtering' mode, as shown in Figure 1.2, whereby the flexure element was bent up, against the fulcrum. The transmission ratio of the Nanogate in this mode was consequently very high. The second mode was 'flushing,' whereby the flexure was bent down, and a large slit opened, to flush out impurities or particles trapped in the gap, as shown in Figure 1.3.

Two challenges existed with this device: first, the dimension of the aperture was not constant, i.e. the channel had some slope due to the curvature of the flexure. Second, it was uncertain how to adequately constrain the silicon wafer against the machined glass flats to prevent leaks around the flexure edges (where strains are highest). These leaks could conceivably circumvent the valve land entirely. This led to a proposed circularly symmetric design, which would guarantee that there were no secondary leaks between the inlet and outlet ports.

3.2 Case 2: Circular, Free, Macroscopic

The second prototype embodiment of the Nanogate was a macroscopic, circularly symmetry geometry with a free-rotating fulcrum as shown in Figure 3.2. In this embodiment,

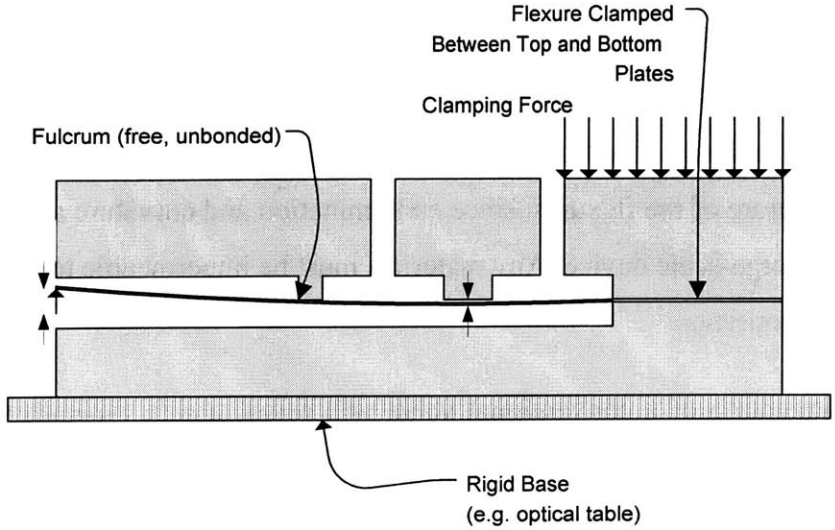

Figure 3.4 Basic Operation of Nanogate (free fulcrum)

three approaches were pursued in fabricating the valve land structure. The flexure structure was a standard double-side polished 2" silicon wafer. Initially, diamond-turning of a nickel-plated aluminum blank was attempted. Regrettably, the nickel plating failed to adhere to the aluminum, and eventually began to delaminate, eliminating any possibility of creating a seal. A second approach was to use a ground and polished Pyrex glass valve seat and fulcrum, which were bonded with leak sealant epoxy to the aluminum base (see detail, Figure 3.2). This was a more viable approach since the glass could be very finely polished, to create a good sealing surface. However, the order of machining and polishing is important! Initially, the valve land was polished and then the fulcrum and inlet/outlet ports were machined into it. However, the edges of the machined glass now had excessive positive skewness, i.e. protruding spikes approximately 100nm in height, which prevented sealing. Last, a second machined and polished glass flat was made which solved the problem of positive skewness by rounding the edges of the device, and which had a flatness of approximately $\lambda/30$. This final implementation was used to successfully demonstrate a seal (after suitable cleaning processes) against 5 psi of dry nitrogen, using a bubble test. However, the cost to develop this first working prototype was nearly $20,000; clearly this was not an economical approach.

3.3 Materials Selection - Macroscopic Valve

By far the overriding requirement of the Nanogate is that it can form a reliable seal, even in a high vacuum environment. This places stringent requirements on material selection and processing. The design of a macroscopic device must be tolerant of contamination and the inherent curvature of the flexures, since contamination and curvature are very difficult to eliminate in a large-scale device. Any materials must be impermeable to gases and have low outgassing properties.

A cursory examination of a conventional valve will reveal a soft, typically elastomeric, sealing material that provides an elastically averaged seal when compressed against the valve land. In high vacuum equipment, valves typically employ a rigid knife-edge that is compressed against a relatively compliant, polished plate beyond the elastic limit of the plate material. Nonetheless, the underlying principle is the same: deformations of the sealing layer are required for reliable sealing. This can be accomplished either through material selection or geometry: either one must select compliant materials, or design a structure that can exert high Hertzian stresses in the sealing region. The initial conception of the Nanogate precludes the latter. Therefore, the task is reduced to selecting an appropriate vacuum-compatible material that is also compliant! The requirement of vacuum compatibility immediately excludes all conventional sealing materials such as Buna rubber or Viton. Two materials that were identified as potential candidates are Spectralon and Vespel. Both are relatively compliant polymer materials widely used in space systems due to their low outgassing properties, and mechanical stability over a wide range of temperatures and in a high vacuum environment. As an added benefit, Spectralon is highly reflective; it is used as a diffuse reflection standard. Table 3.3 gives a list of material properties.

To minimize the inherent curvature of compliant flexures, special processing is required. The range of flexure materials is quite large: silicon wafers, aluminum discs, glass flats, and stainless steel shim stock were all possibilities. However, to minimize the sealing force, the flexure must be as flat and uniform as possible. Conventional design rules for

ultra-flat structures require the thickness of the plate to be at least 1/6th of its diameter. To make a compliant flexure that is ultra-flat therefore necessitates special processing. Residual stresses due to manufacturing and cutting must be relieved, and the polishing process must not cause any elastic deformation of the flexure. Due to the amount of development that has been focused on silicon wafers, these were selected. The conventional 2" silicon wafers that were used initially, had typical bow and warp on the order of 25 microns across the diameter of the wafer. In addition, the wafers are not warped into a uniform saddle or bowl shape. Rather, they are wavy and highly non-uniform. Double-sided polishing, or processes such as cold blocking have been proposed to alleviate this bow and warp.

3.4 Metrology

Two types of high resolution measuring equipment were considered: capacitance probes and interferometry. Capacitance probes must be placed within 10 microns of the target in order to achieve nanometer resolution. This requirement precludes direct measurement of the gap. Rather, one would have to measure the backside of the wafer as it is deformed. This is unsatisfactory for precise determination of nanometer-scale deflections. Interferometry, by contrast, allows direct measurement of the gap through a vacuum-sealed window. Furthermore, the interferometer can measure large displacements with high accuracy. Since the physical constraints of the apparatus preclude the use of a conventional two-beam interferometer, a single-beam 'optical probe' is used, with a resolution of 2.4 nm and a range of 5 mm. A schematic of the optical probe is shown in Figure 3.5. The focusing lens is necessary to allow alignment; without it, the probe has excessive sensitivity to the tilt of the test optic and cannot be aligned.

3.5 Material Selection

A summary of the materials considered for each component of the macroscopic Nanogate is given in Table 3.3 below. The materials were evaluated on the basis of machinability,

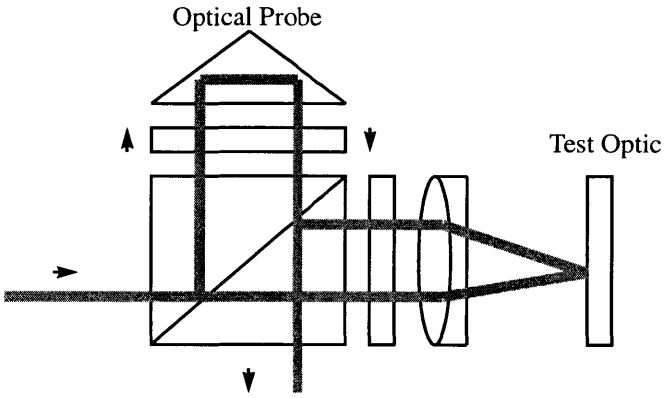

Figure 3.5 Optical probe

vacuum stability, outgassing rate and chemical permeability, but not cost. Since this was a prototype, the machining costs far exceeded material costs.

3.6 Actuation

A number of actuators were considered. Precision micrometers, with a resolution of 1 micron, were initially employed due to low cost and ease of mounting. However, the New Focus Picomotor was ultimately selected since it can provide 30 nm motion resolution (or less, depending on load) steps, and is controllable from Labview. It is also significantly less expensive than comparable linear actuators. It should be noted that when the picomotor is actuated, however, it induces significant vibrations in the experimental setup, which reduce the accuracy of measurements. Also, the size of the steps is not repeatable; the picomotor is actuated by a piezoelectric ball screw which has hysteresis. The Picomotor does not have built-in closed-loop control; this must also be implemented externally if desired.

3.7 Solid Mechanics

The bending of a circular plate with radially symmetric loading can be modeled as:

TABLE 3.3 Material Selection

Component	Materials Considered *(Selected)*	Reasons
Frame	Aluminum 6061	• Easily machined, can be diamond turned to obtain finish required for vacuum chuck.
Load cap	Aluminum 6061	• Easily machined, can be diamond turned for critical regions.
Base plate	Stainless Steel	• Vacuum compatible; low outgassing. • Cannot be diamond turned; for high quality surface must be lapped.
	Zerodur	• Vacuum compatible, low outgassing. • Optically transparent (simplifies metrology). • Must be polished, therefore only flat surfaces can have high quality surface finish cheaply.
	Aluminum 6061 with Nickel Phosphorous plating.	• Vacuum compatible, resistant to corrosion due to nickel plating. • Easily machined, and can be diamond turned.
Flexure	Silicon Wafer	• Can be purchased cheaply with highly polished surfaces. • Bow and warp prevents reliable sealing.
	Silicon Wafer with Silicone RTV sealing layer	• Silicone provides elastically averaged seal. • Silicone is not vacuum compatible due to gas permeability and outgassing. • Could be appropriate for fluid valve applications.
	Silicon wafer with Spectralon or Vespel sealing layer	• Spectralon and Vespel are different polymer materials that are vacuum compatible. • They are relatively soft compared to silicon, and therefore can form an elastic sealing layer.
	Glass flat	• Glass flats are flat to $\lambda/20$, and highly polished. However, they are also very thick, which gives a very tiny range of motion. • Elastic sealing is precluded since the flat is rigid. Thus the seal is not robust to contamination.
	Mirrored glass	• "ultra-flat" glass mirror, made by Polaroid. • Thickness (hence stiffness) precludes elastic seal. However, glass is bowed more than 3 microns.

TABLE 3.3 Material Selection

Sealant	Kurt Lesker KL-5	• Vacuum sealant with no outgassing and low viscosity to fill tiny gaps. • Bonds rigidly to metal, glass and ceramics. • Dissolves in solvents.

$$\frac{d}{dr}\left[\frac{1}{r}\frac{d}{dr}\left(r\frac{dw}{dr}\right)\right] = \frac{Q(r)}{D}, \tag{3.1}$$

where r is the radius, w is the deflection, Q(r) is the applied shear force, and D is the bending stiffness of the plate.

3.7.1 Deflection

The loading of the flexure plate for in the Nanogate is shown in Figure 3.6 (a). The deflection of this structure can be determined using the principle of superposition, as shown in Figure 3.6 (b), (c) and (d) below. First, the deflection due to the preload pressure q is determined, then the deflection due to the reaction $P + q\pi c^2$ is subtracted. Last, the effect of the curvature of the wafer is added, in the form of a moment per unit length M_0 (units of N.m/m, total moment = $M_0 2\pi a$) at the edge. The resulting deflection is [Roark, 1943], for r > b:

$$w = -\frac{3qc^2(1-\nu^2)}{16Eh^3}\left[\frac{(12+4\nu)(a^2-r^2)}{(1+\nu)} - \frac{2(1-\nu)c^2(a^2-r^2)}{(1+\nu)a^2} - (8r^2+4c^2)\ln\frac{a}{r}\right] \tag{3.2}$$
$$+\frac{3(P+q\pi c^2)(1-\nu^2)}{2\pi Eh^3}\left[\frac{(3+\nu)(a^2-r^2)}{2(1+\nu)} - (r^2+b^2)\ln\frac{a}{r} - \frac{(1-\nu)b^2(a^2-r^2)}{2(1+\nu)a^2}\right]$$
$$+\frac{6(1-\nu)}{Eh^3}M_o(a^2-r^2)$$

and for c < r < b:

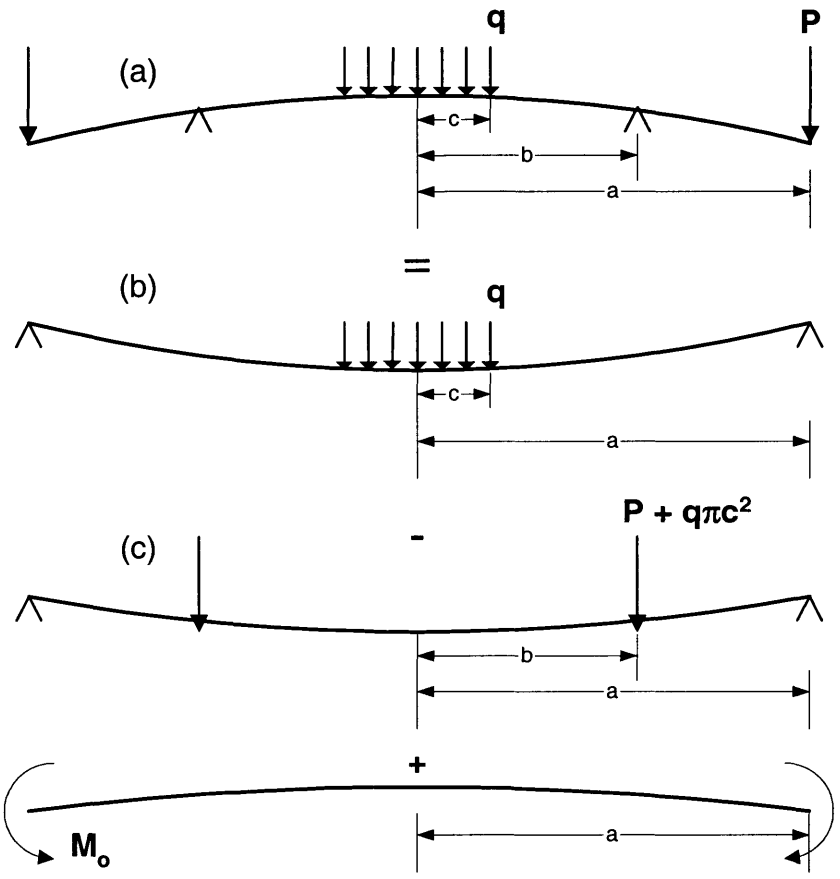

Figure 3.6 Superposition of loads to determine deformed shape (M_0 is bow/warp).

$$w = -\frac{3qc^2(1-\nu^2)}{16Eh^3}\left[\frac{(12+4\nu)(a^2-r^2)}{(1+\nu)} - \frac{2(1-\nu)c^2(a^2-r^2)}{(1+\nu)a^2} - (8r^2+4c^2)\ln\frac{a}{r}\right] \quad (3.3)$$
$$+\frac{3(P+q\pi c^2)(1-\nu^2)}{2\pi Eh^3}\left[\frac{(3+\nu)(a^2-r^2)}{2(1+\nu)} - (r^2+b^2)\ln\frac{a}{b} + (r^2-b^2)\right.$$
$$\left. - \frac{(1-\nu)b^2(a^2-r^2)}{2(1+\nu)a^2}\right] + \frac{6(1-\nu)}{Eh^3}M_o(a^2-r^2)$$

and for r < c:

$$w = -\frac{3qc^2(1-\nu^2)}{16Eh^3}\left[4a^2 - 5c^2 + \frac{r^4}{c^2} - (8r^2 + 4c^2)\ln\frac{a}{c} - 2\frac{(1-\nu)c^2}{1+\nu}\frac{}{a^2}(a^2 - r^2) + \frac{8}{1+\nu}(a^2 - r^2)\right] + \frac{3(P + q\pi c^2)(1-\nu^2)}{2\pi Eh^3}\left[\frac{(3+\nu)(a^2 - r^2)}{2(1+\nu)} - (r^2 + b^2)\ln\frac{a}{b} + (r^2 - b^2) - \frac{(1-\nu)b^2(a^2 - r^2)}{2(1+\nu)a^2}\right] + \frac{6(1-\nu)}{Eh^3}M_o(a^2 - r^2) \quad (3.4)$$

where $q\pi c^2$ is the applied preload force, and P is the total end loading that controls the Nanogate opening. This calculation assumes that the deformed wafer does not contact the rigid foundation; this case is treated separately below. The deformed shape of one-half of the wafer (0 < r < a) is shown in Figure 3.7. The geometry and material properties for the ensuing calculations are summarized in Table 3.4. Material properties for single crystal

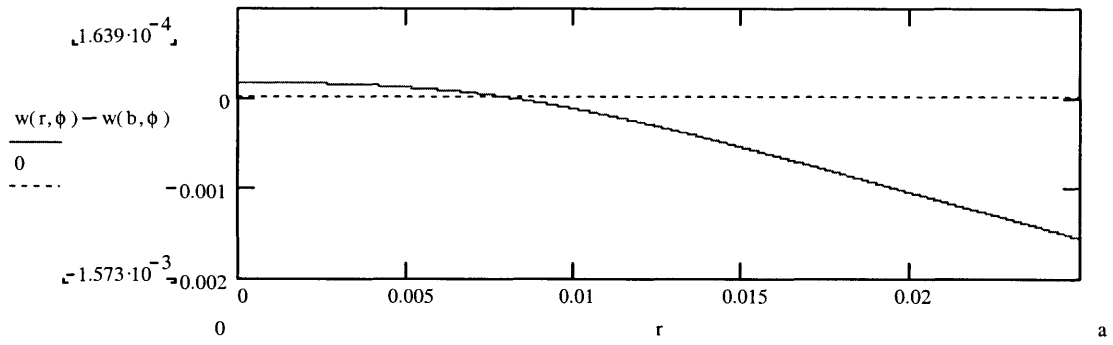

Figure 3.7 Deformed shape of the Nanogate wafer (P=10 N, q = 100 kPa)

silicon are taken from [Senturia, 2001].

The transmission ratio is defined as the deflection of the edge of the valve land, located at r = c, compared to the deflection of the edge of the flexure, at r = a. This definition is used because the minimum opening of the slit is the parameter of interest, and due to the curvature of the flexure plate, the measured opening is not equal to the minimum opening.

TABLE 3.4 Geometry and material constants for Nanogate

Variable	Value	Units
E	150	GPa
η	300	μm
a	25	mm
b	8.0	mm
c	5.5	mm
q	100	kPa
ν	0.25	
P	10	N

Therefore, for small values of P (i.e. deflections for which the device was subsequently tested), the actual transmission ratio is calculated as:

$$T = \frac{w(c)}{w(a)} = 22.23, \tag{3.5}$$

as compared to the measured transmission ratio of

$$T = \frac{w(0)}{w(a)} = 16.7, \tag{3.6}$$

from which one concludes that the actual gap height is in fact 0.750 times the measured gap height. Note that the calculated transmission ratio from 3.6 and the experimental measurement of the transmission ratio are in agreement.

3.7.2 Stress

The maximum stresses must be determined since they limit the deflections that can be imposed without brittle failure of the flexure. This in turn limits the amount of preload force that can be applied without causing the Nanogate to be clamped shut. The condition for opening is that the center of the flexure ($r < c$) has no negative displacement, while the maximum tensile stress is below the tensile yield stress (250 MPa for double-side polished silicon wafers). For example, for a preload q of 100 kPa and an imposed displacement of

0.522 mm, the stresses are shown in Figure 3.8. The maximum stress is 107.3 MPa, which is 43% of the failure stress of the flexure, although the actual failure stress can vary depending on imperfections in wafers.

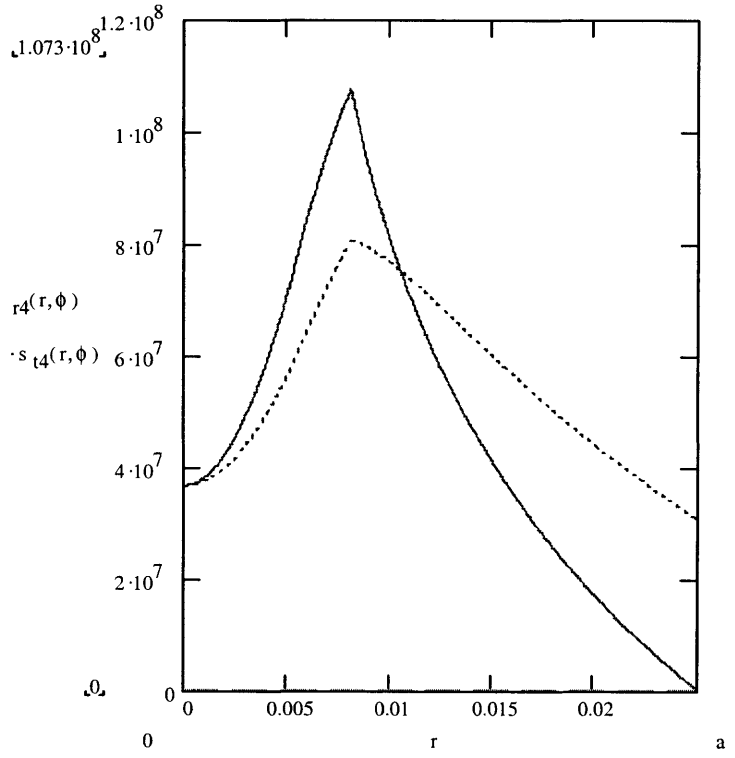

Figure 3.8 Radial and tangential stresses in Nanogate flexure plate.

For an elastically averaged seal, as described in Section 3.8 below, the preload force must be increased substantially to 290 kPa. With this preload force applied, the tensile stresses when opening increase substantially to 164 MPa, which effectively limits the range of the Nanogate, and would cause breakage in single-sided wafers where the maximum stress is approximately 150 MPa due to surface imperfections on the unpolished side of the wafer. Therefore, it is clearly of interest to minimize the preload force required for sealing (and hence the curvature of the wafer). This optimization will allow a wide operating range without the risk of a sudden failure of the flexure.

3.8 Elastically Averaged Seal

An elastically averaged seal can be modeled as a nonlinear plate bending problem. First, a moment is applied to the edge of a plate; this gives it curvature, thereby modeling a real plate. Second, a preload is applied uniformly to the surface of the plate, which compresses the plate against a rigid foundation, as shown in Figure 3.9. Since the conditions at the support change with deflection, this is a nonlinear problem.

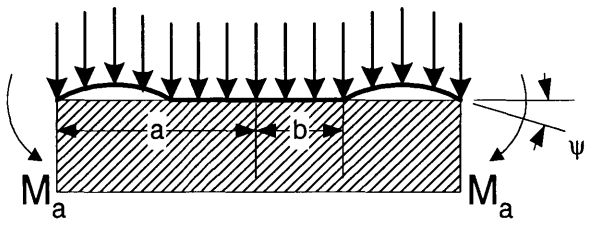

Figure 3.9 Model of elastically averaged seal

The general solution for this type of problem is [Timoshenko, 1940]:

$$w = C_1 + C_2 \ln r + C_3 r^2 + C_4 r^2 \ln r + \frac{qr^4}{64D} \tag{3.7}$$

It is helpful to nondimensionalize (3.7) by substituting $\rho = \frac{r}{a}$. To determine the constants of integration, one applies boundary conditions at r = a:

$$(w)_{\rho = 1} = 0, (M_r)_{\rho = 1} = -M_a \tag{3.8}$$

and at r = b:

$$(w)_{\rho = \frac{b}{a}} = 0, \left(\frac{dw}{dr}\right)_{\rho = \frac{b}{a}} = 0, (M_r)_{\rho = \frac{b}{a}} = 0. \tag{3.9}$$

The condition of zero displacement, zero slope and zero moment at b causes the inside circle to rest flat against the foundation. This is the condition required for an elastically aver-

aged seal as in the Nanogate. Numerically evaluating the constants of integration C_1 through C_4 gives a first-order equation in q (the preload force), given b, as shown in Appendix A. This is then useful as a design parameter, since b is a geometric parameter, and q can be scaled as necessary. In the particular case of the Nanogate, assuming a wafer that is uniformly bowed 25 microns, a preload pressure of 290 kPa is required, applied uniformly over a circle 8 mm in diameter.

3.9 Scaling

Miniaturization of the Nanogate is of great interest. Therefore, the scaling parameters of the device must be established to guide future designs. Depending on the application, the stiffness, the flowrate or the transmission ratio are of interest. One limitation of testing a macroscopic prototype, however, is that not all potential problems scale with length -- for example, the scale of contaminant particles does not scale with the device. Therefore, particulates which do not cause problems for a large device with high preload forces, may be extremely problematic at small scales. Conversely, during assembly, the probability of a particle falling between the mating surfaces of the Nanogate is significantly reduced.

3.9.1 Stiffness

For the purpose of measuring pressures in the flow channel, or overcoming attractive forces due to surface tension, the stiffness is defined as the ratio of the force P applied at the end to the displacement at the point c, the start of the valve land:

$$k = \left(\frac{dw}{dP}\right)^{-1}\Bigg|_{r=0}, \tag{3.10}$$

where w(r) is given by equation 3.3. Therefore,

$$k = \frac{2\pi E h^3}{3(1-\nu^2)a^2\left[\frac{3(1-\nu^2)}{2(1+\nu)} - \beta^2\left(\ln\beta - 1 - \frac{(1-\nu)}{2(1+\nu)}\right)\right]}, \tag{3.11}$$

where $\beta = \frac{b}{a}$.

Examining equation 3.11 shows that the stiffness is proportional to the plate thickness cubed ($k \propto h^3$), and inversely proportional to the plate dimensions squared. The relationship to the individual geometric parameters a and b is not as straightforward. It is convenient to nondimensionalize these parameters as $\beta = \frac{b}{a}$, and then evaluate the stiffness for multiple values of β, as shown in Figure 3.10 for a constant wafer radius of a = 25 mm.

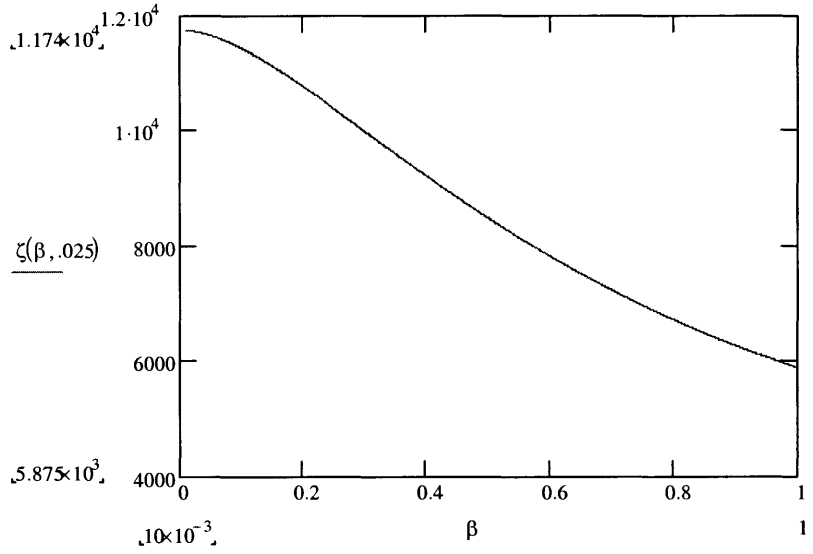

Figure 3.10 Stiffness, as a function of β, for a 50 mm-diameter wafer.

To make a highly sensitive force measurement apparatus, the stiffness must be very small, on the order of 1 N/m. Therefore it is necessary to, for example, reduce the thickness by a larger factor than the lateral dimensions. For example, reducing the diaphragm thickness to 2 microns and the diaphragm diameter to 1 mm gives a stiffness of 1.8 N/m, for β = 0.3. Such a device would, of course, be impossible to operate due to stiction between the mating surfaces. An optimum between stiffness and force sensitivity would need to be found as part of the design process for a surface force sensing device. This strongly motivates the need to produce micromachined Nanogate structures so that the design can be applied to

fluid flow experiments where precise information about the pressure forces acting on the surfaces is needed.

3.9.2 Flowrate

The equations governing the gas flowrate are the same at small length scales as in the macroscopic region. Gas flowrate remains proportional to the gap height squared as long as the opening is on the order of the mean free path. The flowrate remains a function of the resolution of the actuator and the (non dimensional) transmission ratio and irrespective of the scale of the device, provided the ratio between the inlet and outlet dimensions of the gap is preserved.

3.9.3 Sealing Force

The sealing pressure is calculated using equations 3.7 to 3.9, solved using the technique of Appendix A. The equations are dominated by the applied moment (hence the initial curvature) of the wafer-- the preload pressure varies linearly with the initial curvature. Given a constant initial curvature, the required preload pressure remains a constant with the length scale of the device.

The optimal design of the Nanogate used MEMS technology extensively. This led to radical improvements in cost, ease-of-manufacture and performance. This final approach used a bonded, flexible fulcrum structure as shown in Figure 3.11, coupled to external metrology and actuation apparatus. These are described in detail in Section 3.10.

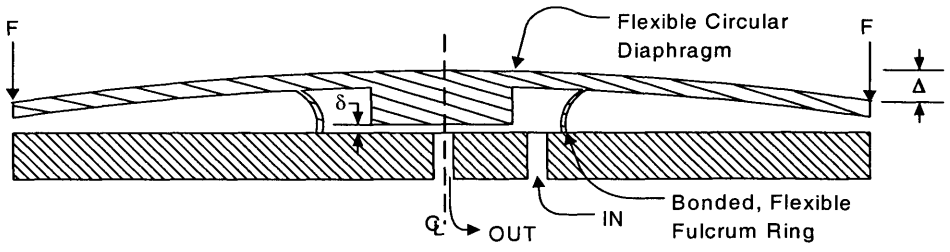

Figure 3.11 Bonded, circularly symmetric MEMS Nanogate concept.

3.10 Case 3: Circular, Bonded, Microscopic

The shift to MEMS (Micro Electro Mechanical Systems) technology was a great leap forward in the manufacturability of the Nanogate. By moving to a simple MEMS design, without integrated actuation or displacement sensing, it was possible to create, at low cost, arrays of structures that were reliably sealed against leakage across the fulcrum (now a flexible ring), and where both fine surface flatness and polish came at no additional cost. This structure, shown in Figure 3.12, was then used to demonstrate the fine control, sealing and flow properties of the Nanogate.

MEMS fabrication techniques, in general, allow the fabrication of large arrays of high precision planar structures, which can then be combined by wafer bonding techniques into three-dimensional structures. The wide spectrum of available fabrication technologies are too numerous to discuss here in any detail, although a useful summary can be found in [Senturia, 2001]. However, they can be broadly categorized into material removal (etching) processes, material addition (deposition), and bonding processes. In the context of this thesis, two enabling technologies are particularly important. The first is Deep Reactive Ion Etching (DRIE) whereby silicon is etched in deep trenches using a reactive ion etching and passivation process. The second is aligned wafer bonding, whereby two wafers are positioned with several micron precision and then fixed in permanent contact. Without these two techniques, large aspect ratio three-dimensional silicon structures would be very difficult, if not impossible, to manufacture.

3.10.1 Description

The basic MEMS Nanogate is a bonded assembly of a deep RIE etched silicon wafer, anodically bonded to a machined Pyrex 7740 wafer, as shown in Figure 3.12. The surface roughness of each of these surfaces is in the 3-5 nm range, with overall flatness (bow/warp) of similar order. The valve land of the silicon wafer is coated with a layer of metal, in this case gold, which prevents bonding in that region during assembly. Therefore the valve is fabricated "normally closed" without the need for any release process. Further-

more, the intervening layer of gold, about 200 nm total, provides a preload force that aids in sealing the device. A deflection is applied to the outer periphery of the Nanogate diaphragm, using an external apparatus as shown in Figure 3.14.

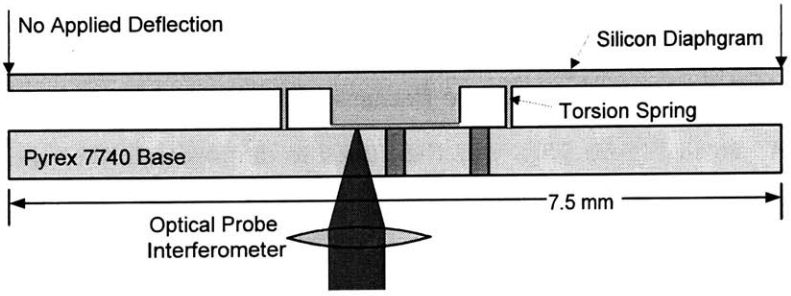

Figure 3.12 Undeflected MEMS Nanogate (x-sec 3-3)

In the final implementation of the MEMS Nanogate, no attempts were made to integrate the displacement sensing and actuation functions of the device. Integrated actuation and displacement sensing are highly advantageous (for example, the creation of parallel arrays of active devices), however, and are the subject of ongoing development. Deflections were imposed using a Picomotor piezoelectric actuator, attached to an EDM-machined Super Invar flexure. Displacement was sensed with a single-point interferometer with a resolution of 2.4 nm. A Buna rubber O-ring 7.0 mm in diameter was used to transfer displacements from the super invar flexure assembly to the outer periphery of the Nanogate diaphragm, as described in detail in section 6.2.1. One benefit of making a device that is relatively large is that the interface to macroscopic external actuators, interferometry and packaging can be simplified, without the loss of performance.

3.10.2 Mechanics

The solid mechanics of the MEMS Nanogate are not fundamentally dissimilar from the mechanics of the macroscopic, circular Nanogate discussed in detail above. However, the bonded, flexible fulcrum structure, did change the mechanics of the structure somewhat. The flexible fulcrum was modeled as a torsion spring, which applied a moment to the dia-

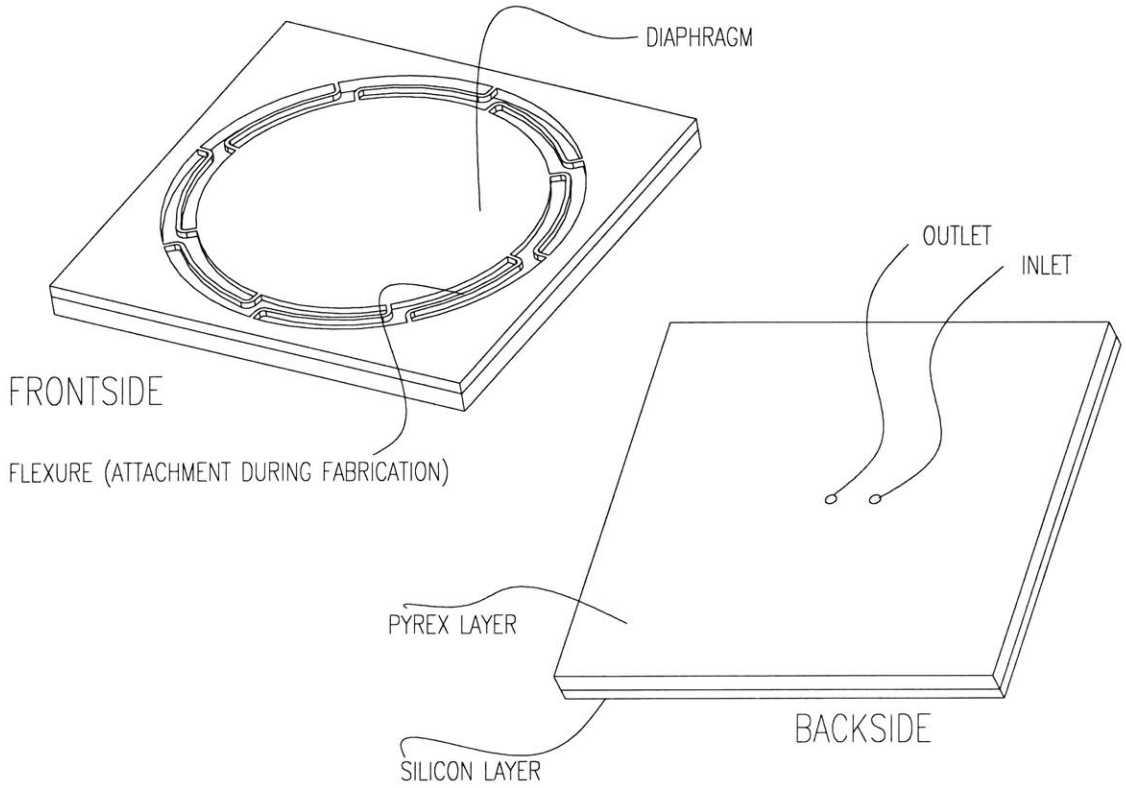

Figure 3.13 MEMS Nanogate Assembly, Top (Fig. 1) and Bottom (Fig. 2) Isometric Views

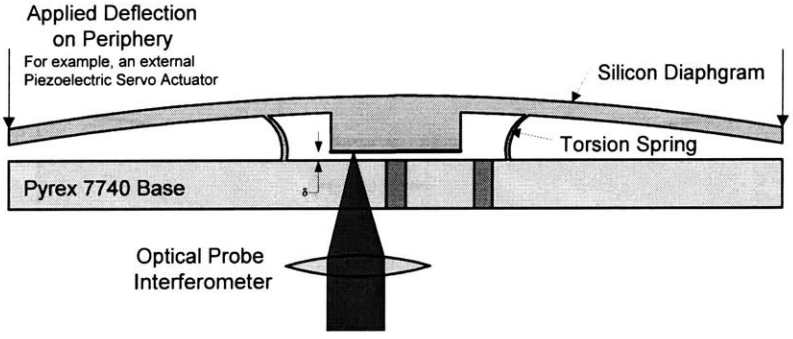

Figure 3.14 Nanogate cross-section, in operating mode.

phragm at its attachment point, as shown in Figure 3.15. The flexible fulcrum can be modeled as a cylindrical shell. The torsional stiffness of the fulcrum is [Roark, 1943]:

$$\tau = \frac{M_2}{\phi} = \lambda D, \tag{3.12}$$

where D is the plate stiffness of the shell,

$$D_1 = \frac{Et^3}{12(1-\nu^2)}, \tag{3.13}$$

E is Young's modulus, ν is Poisson's ratio, t is the shell thickness, and a is the radius of the fulcrum. λ is defined as:

$$\lambda = \sqrt[4]{\frac{3(1-\nu^2)}{R^2t^2}}, \tag{3.14}$$

The deformation of the Nanogate can thus be solved by superposition, neglecting any deflections at the attachment of the diaphragm to the fulcrum.

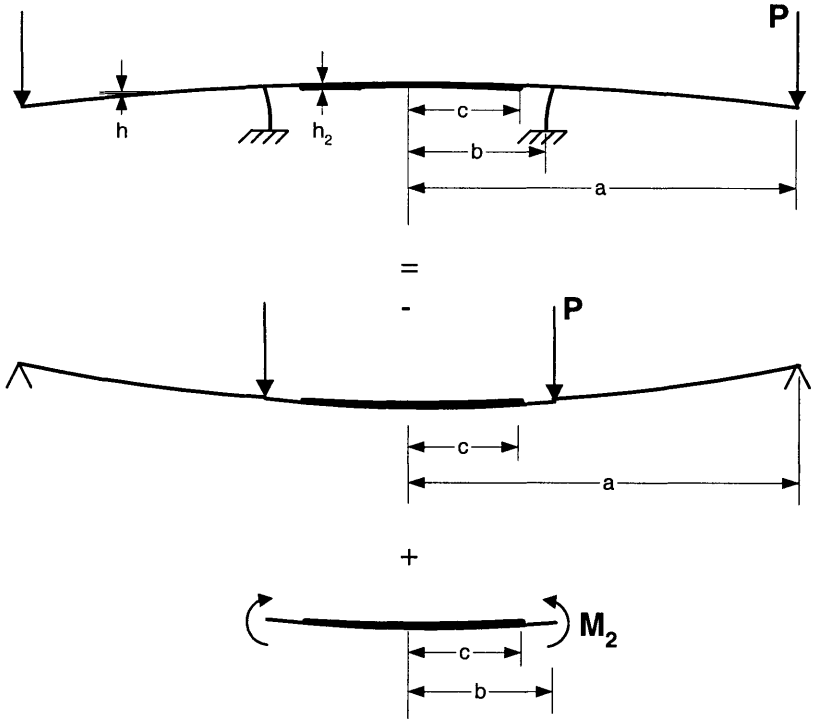

Figure 3.15 Mechanics of Bonded Nanogate

At the attachment point of the flexible fulcrum to the diaphragm (at r = b in Figure 3.15), the bending moment in the plate undergoes a discontinuity. The flexible fulcrum has the effect of stiffening the center diaphragm. The moment required to deform the fulcrum can be determined by equating the angular deformation of the diaphragm to the angular deformation of the fulcrum at their attachment point:

$$M|_{b_-} - M|_{b_+} = \lambda D_1 \left(\frac{dw}{dr}\right)\Big|_b \tag{3.15}$$

Notwithstanding, the stiffness of the diaphragm is 50x greater than that of the fulcrum. Therefore, the effect of the fulcrum can be largely neglected in the analysis.

The center of the Nanogate, r < c, is twice the thickness of the diaphragm region. In this analysis, it will be assumed to be rigid, as a simplification, although in reality, it has approximately 10x the stiffness of the region a > r > c.

The deflection of the Nanogate diaphragm in the region c < r < a due to the applied load P is given by [Timoshenko, 1940]:

$$w(r) = \frac{Pr^2}{8\pi D}\left[\ln\left(\frac{r}{a}\right) - 1\right] - \frac{D_1 r^2}{4} - D_2 \ln\left(\frac{r}{a}\right) + \frac{c^2 M_1}{2(1+\nu)D(a^2 - c^2)}(a^2 - r^2) + \frac{a^2 c^2 M_1}{(1-\nu)D(a^2 - c^2)} \ln\left(\frac{r}{a}\right) + D_3 \tag{3.16}$$

where M_1 is the moment applied per unit length due to the built-in edge at c, and is determined numerically such that the slope at c is zero. The constants D_1, D_2 and D_3 are given by:

$$D_1 = \frac{P}{4\pi D}\left(\frac{1-\nu}{1+\nu} - \frac{2b^2}{a^2 - b^2}\ln\left(\frac{b}{a}\right)\right), \tag{3.17}$$

$$D_2 = \frac{-(1+\nu)P}{(1-\nu)4\pi D}\frac{a^2 b^2}{a^2 - b^2}\ln\left(\frac{b}{a}\right), \tag{3.18}$$

and

$$D_3 = \frac{Pa^2}{8\pi D}\left(1 + \frac{(1-\nu)}{2(1+\nu)} - \frac{b^2}{a^2-b^2}\ln\left(\frac{b}{a}\right)\right). \tag{3.19}$$

The deflection of the Nanogate diaphragm due to the moment applied by the fulcrum in the region c < r < b is:

$$w_f(r) = \frac{M_2}{2D}\left(\frac{1}{(1+\nu)+(c^2/b^2)(1-\nu)}\right)\left[(c^2-r^2)+2\ln\left(\frac{r}{c}\right)\right], \tag{3.20}$$

where M_2 is determined from the slope at b and 3.12. The stiffening effect due to the fulcrum is negligible in this case, however.

Dimensions of the MEMS Nanogate are listed in Table 3.5. The deflected shape of the

TABLE 3.5 Dimensions of MEMS Nanogate

Parameter	Value	Units
Diaphragm		
a	3.75	mm
b	1.25	mm
c	0.75	mm
h	150	μm
h_2	300	μm
Fulcrum		
R	1.25	mm
t	25	μm
Material		
ν	0.25	
E	150	GPa

MEMS Nanogate is shown in Figure 3.16.

The transmission ratio of the Nanogate, which is defined as the ratio of deflection applied to the outer periphery of the diaphragm to the deflection in the center, is calculated as:

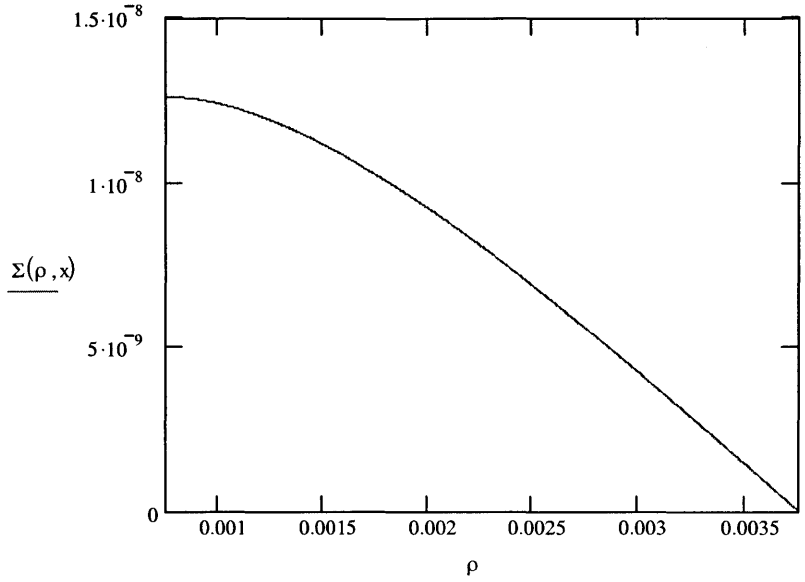

Figure 3.16 Deflected shape of Nanogate

$$T = \frac{w(0)}{w(a)} = 16.9. \tag{3.21}$$

The stresses in the Nanogate are concentrated at the attachment point of the diaphragm to the fulcrum. The actual stresses are also a function of the manufacturing process, since footing causes a fillet to form at that point. Finite element analysis was used to estimate the internal stress, and the maximum deflection of the Nanogate. The results of this analysis, shown in Figure 3.17, indicate that, assuming a yield stress of 1 GPa for silicon, the maximum deflection of the periphery is 125 microns. The maximum stress at the top of the fulcrum was also calculated analytically, since in the FEA model, that region represents a stress concentration. Analytically, the stress is given by [Roark, 1943]:

$$\sigma_{max} = \frac{2M_o}{t}\lambda^2 R = \frac{2\lambda^3 DR}{t}\theta \ . \tag{3.22}$$

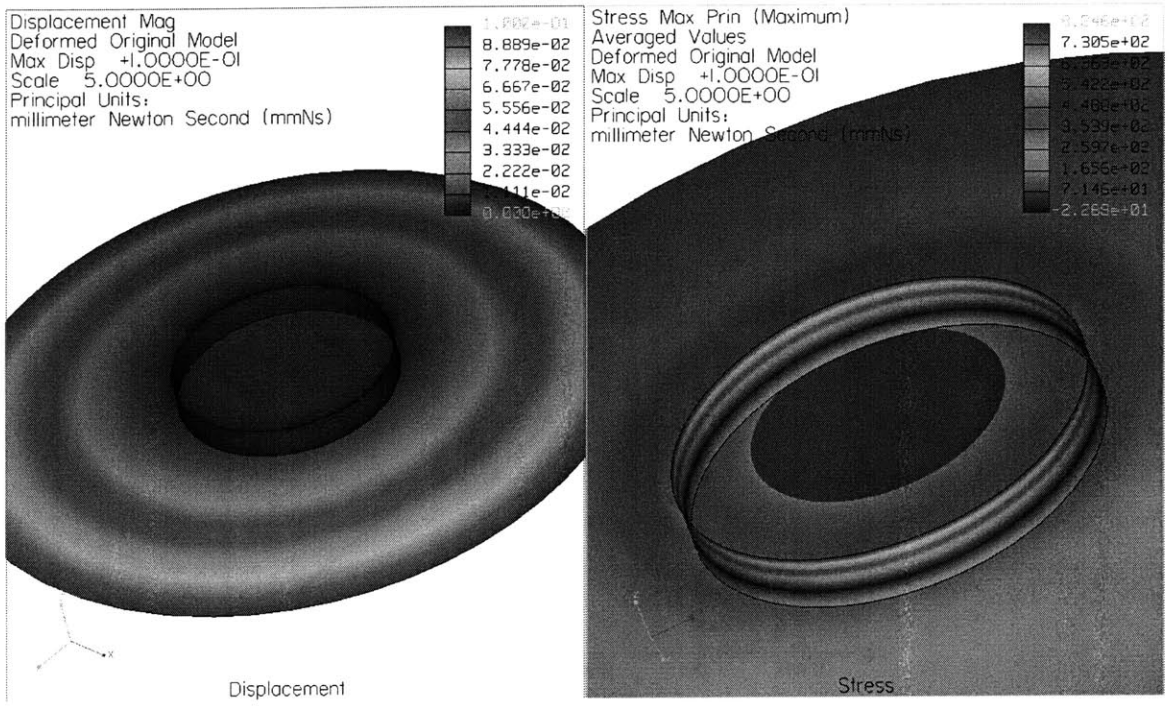

Figure 3.17 Deflection and stress for Nanogate

For the Nanogate, assuming the maximum stress in the fulcrum can be 1 GPa, the maximum deflection on the periphery is 71 μm. The maximum deflection in the center is 4.2 μm, while the minimum deflection is nominally less than 1 nm. The dynamic range of the Nanogate is on the order of 10^3 in terms of deflection, or 10^6 in terms of flowrate for gas flow, and 10^9 for liquid flows.

3.11 Final Dimensions of Nanogate

The final dimensions of the Nanogate were driven by several factors, including:

1. The minimum size of fluid interconnections (ultrasonically drilled holes in Pyrex) is 250 microns.
2. Alignment tolerances during assembly and bonding, for edge-alignment (original technique was die-level bonding) were 100 microns.
3. The necessity to include optical access for the interferometer beam, which had a minimum waist size of 170 microns -- the desired alignment region was approximately 500 microns.

4. Manufacturing limitations, specifically the use of transparency masks with a minimum useful feature size of 70 microns (although this dimension was successfully shrunk down to ~7-10 microns with the stepper). Also, there are aspect-ratio limitations of the STS DRIE process when etching thin features in open fields.
5. Stresses in the fulcrum and diaphragm, and the desired dynamic range of the device, which required the fulcrum thickness to be minimized.
6. The minimum step size of the actuator, and the desired minimum step size of the Nanogate, nominally 30nm and 2.4nm each, so a transmission ratio of at least 15 was required.
7. The total thickness of the Nanogate (diaphragm + fulcrum) was driven by the thickness of readily available silicon wafers. The practical lower limit on wafer thickness is 250-300 microns, below which handling and manufacturing are more difficult. However, the stiffness of the fulcrum is not dependent on the fulcrum height as long as the ratio of fulcrum height to thickness was greater than ~3. Diaphragm stiffness is proportional to diaphragm thickness

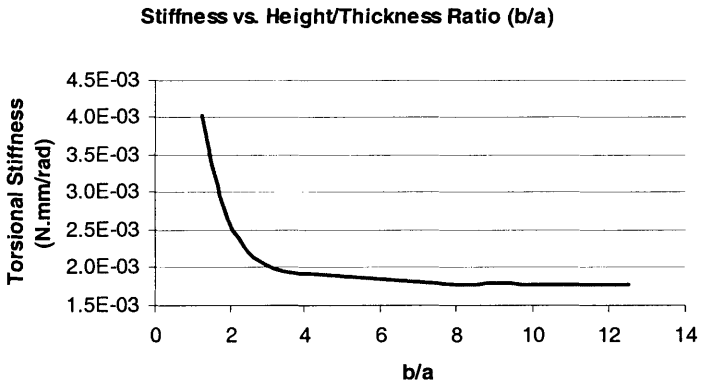

Figure 3.18 Design study of fulcrum stiffness.

cubed, but the piezoelectric actuator strength is large enough to overcome any variations in this parameter. Thus, the exact etch depths and ratio of fulcrum height to diaphragm thickness are not germane to the final operation of the device.

Figure 3.19 shows the final dimensions of the Nanogate. This final iteration of the Nanogate were optimized for manufacturability, insensitivity to manufacturing variations, and simplicity in terms of interfaces to macroscopic external actuation, metrology and fluid

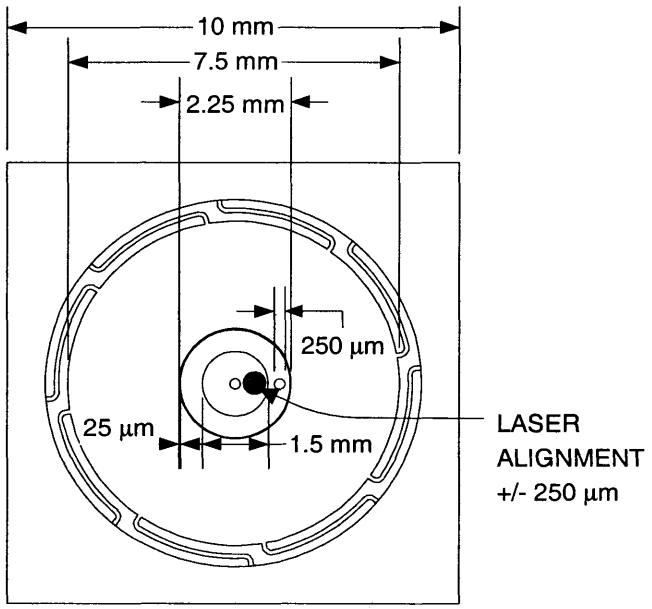

Figure 3.19 Nanogate Dimensions

connections. Application-specific optimizations, incorporating for example integrated actuators, displacement metrology and interfaces to other microfluidic systems are not precluded by this design. Rather, the final Nanogate shown here represents a platform technology for future development!

Chapter 4

FABRICATION

4.1 Process Flow

The primary challenge in fabrication of the Nanogate was to preserve the surface finish of the valve mating surfaces. Corning Pyrex 7740[1] glass wafers were used as-bought, with ultrasonically drilled holes for fluid connections. The silicon wafers had 1.0 micron of thermal oxide grown as a hard mask, which was effective in preserving their surface finish through all of the etching and cleaning steps in the process flow. This oxide mask was removed prior to metallization and bonding. Of particular note are the cleaning steps prior to metallization and bonding, since these are the only steps which affect the valve mating surfaces directly, and special care must be taken at these steps to preserve the integrity of the exposed surfaces.

An equally important fabrication technique is the use of a selective anodic bond to alleviate the need for a post-processing release. Anodic bonding is a process whereby a silicon and a Pyrex wafer are mounted in intimate contact, heated to 325°C, and high voltage (800-1000 V depending on the thickness of the Pyrex wafer) is applied across the wafer stack. At elevated temperatures, the sodium ions in the Pyrex become mobile. The applied electric field causes the sodium ions to migrate away from the bond interface, establishing a large electrostatic attraction at the interface. Furthermore, the silicon and pyrex form an

1. http://www.corning.com/lightingmaterials/products/waferglass.html

intermediate layer of silicon dioxide [Ayon, 1998]. Therefore, the anodic bond is formed by both electrostatic attraction and a chemical bond. The presence of a metal film (which must also be unreactive with Pyrex glass and silicon dioxide) on either the Pyrex or the silicon surface prevents this bond from forming, a feature which is very useful in the current application. Furthermore, the metal film gives a preload which causes plastic deformation of the Pyrex glass during bonding, and gives a small preload stress that helps sealing when the valve is shut. The anodic bond is much less sensitive to particulate contaminants than, for example, a silicon direct wafer bond. This dramatically increased the device yield in prototype runs.

Anodic bonding can be performed on large stacks of alternating glass and silicon wafers. The current application uses two silicon wafers, with one glass wafer sandwiched between them. The three-wafer stack is diced, and individual dies are bonded to thick machined Pyrex bases which retain the macroscopic fluid connections. Other devices [Roberts, 2002] have been successfully demonstrated with nine alternating layers, although in principle there is no limit to how many could be assembled. The final process flow is documented in Figure 4.1, Figure 4.2 and Table 4.1.

4.2 Fabrication Results

It was especially important to determine the final surface finish, bow and warp, and skew in order to evaluate the manufacturing results. A Zygo NewView 5032 optical profilometer and a LEO scanning electron microscope were used for this purpose. The optical profilometer is especially suited for measuring flat surfaces (either reflective or transparent), and can resolve up to 3 Angstroms in the vertical dimension, with lateral resolution up to 0.5 microns. A typical scan of the surface of a machined Pyrex wafer is shown in Figure 4.3. The roughness of this wafer is 12 nm, somewhat higher that expected. However, it is also important to note that the holes have been drilled such that they exhibit negative skewness: there are no upward protrusions on the wafer surface. This is essential for the valve seal. A positive skewness defect is akin to an (immovable) particle in the chan-

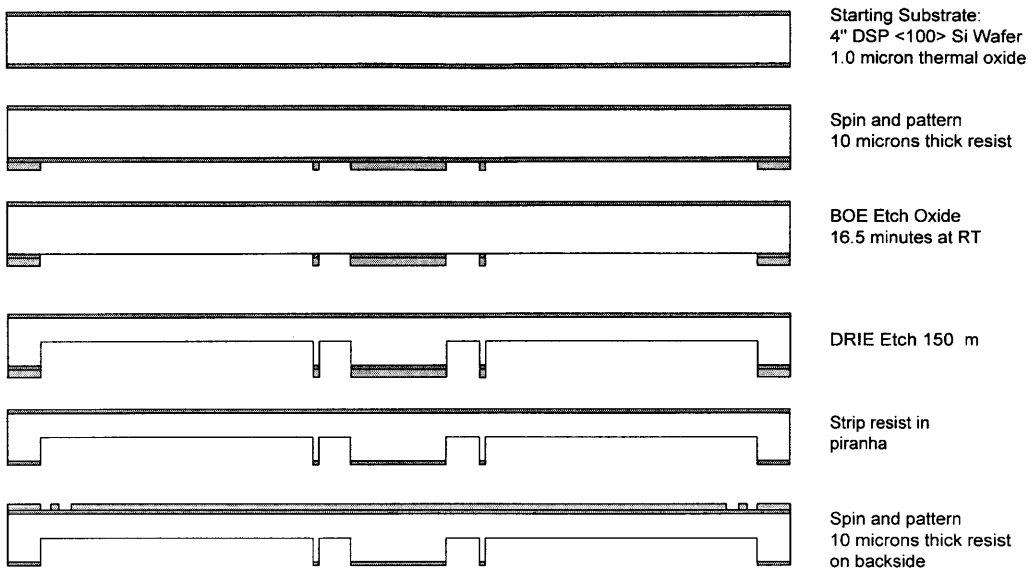

Figure 4.1 Nanogate bottomside process flow.

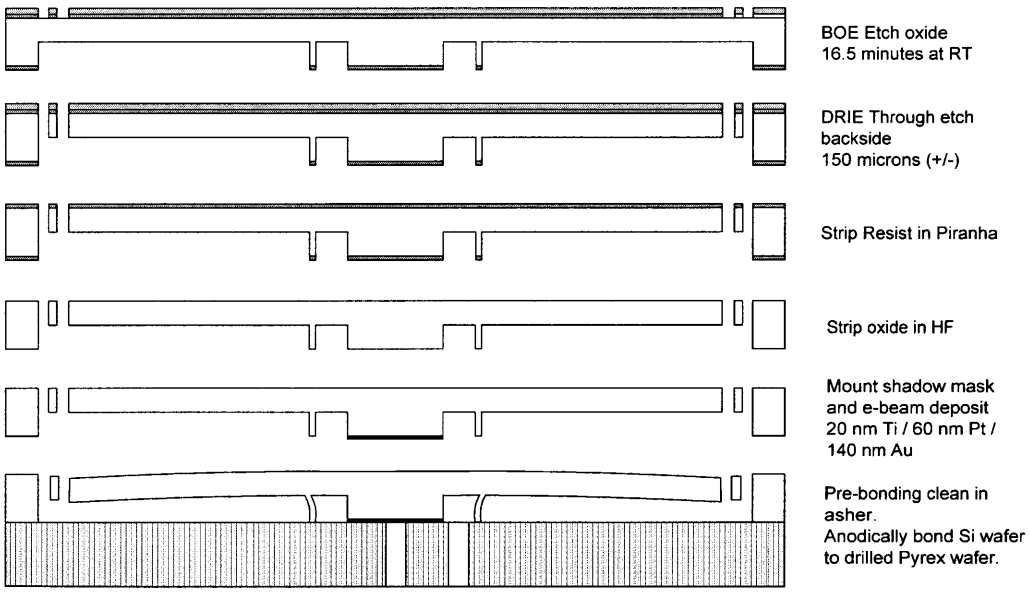

Figure 4.2 MEMS Nanogate process flow: topside and bonding

nel, and will most often preclude sealing in the absence of large preload forces and deformable seating surfaces, or a complementary defect (pit) on the top mating surface.

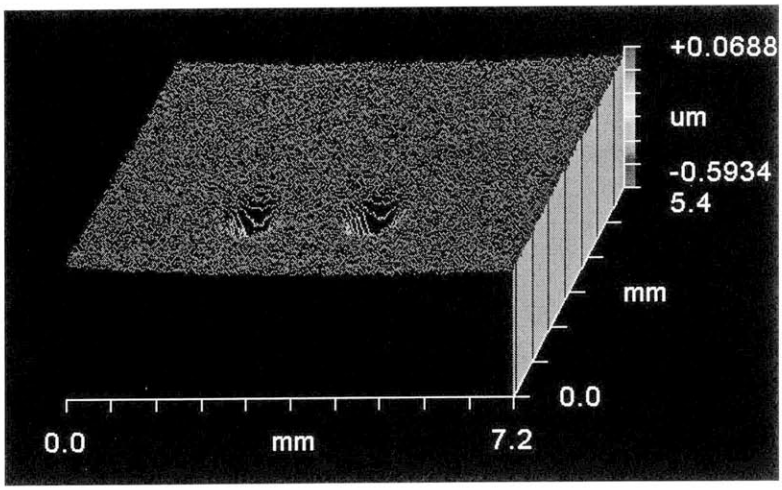

Figure 4.3 Zygo scan of surface of machined Pyrex wafer.

Metrology on the surfaces of Nanogates that were fabricated and then pried apart are discussed extensively in Section 4.3.

TABLE 4.1 Nanogate Process Flow

Step #	Lab	Machine	Notes
1	TRL	HMDS	
2	TRL	Coater	Thick resist 10 microns
3	TRL	Prebake	1.0 hours at 90 C
4	TRL	EV1	Expose frontside mask, 2 intervals, 15s expose x 15s interval.
5	TRL		Develop with AZ440 until pattern is clear, about 3 minutes.
6	TRL	Postbake	30 mins at 90 C
7	TRL	Acid-hood	BOE etch oxide hard mask for 16:30 at room temperature.
8	TRL	Coater	Mount wafer on 6" quartz carrier for STS 2
9	TRL	STS2	Etch 150 microns, MIT69, ~1:20, end on isotropic
10	TRL	Acid-hood2	Piranha dismount, H2O2/H2SO4

11	TRL	HMDS	
12	TRL	Coater	Thick resist 10 microns backside
13	TRL	Prebake	1 hour at 90 C
14	TRL	EV1	Backside mask, 2 intervals, 15s expose x 15s interval.
15	TRL	Develop	Develop in AZ440, approx. 3 minutes.
16	TRL	Postbake	30 mins at 90 C
17	TRL	Acid-hood	BOE etch oxide hard mask for 16:30 at room temperature.
18	TRL	Coater	Mount wafer on carrier for STS
19	TRL	STS2	Etch through backside pattern, MIT69, 1:20
20	TRL	Acid-hood2	Piranha dismount
21	TRL	Acid-hood2	BOE strip oxide
22	TRL	EV Align-Bond	Mount shadow mask wafer in aligner (with tiny drop of resist)
23	TRL	e-beam	Evaporate 20 nm Ti (adhesion) / 60 nm Pt (diffusion barrier) / 140 nm Au film on valve lands.
24	TRL		Dismount in acetone, isopropanol clean
25	TRL	Asher	Ash wafers in barrel asher for 2h, immediately prior to bonding
26	TRL	EV Align-Bond	Wafer bond finished, cleaned Nanogate wafer to Pyrex/Si substrate wafer stack. (bonding temperature, 340 C)
27	ICL	Diesaw	Dice finished wafer stack into dies, 20 mm x 20 mm
28	EML		Anodically bond finished dies onto drilled Pyrex base (bonding temperature, 340 C).
29	EML		Epoxy Kovar fluid connections into finished die and cure in oven at 130 C for 24 hours.

4.3 Fabrication Results

A finished MEMS Nanogate was sacrificed, and surface metrology was conducted on the mating surfaces. The Pyrex and gold mating surfaces were first imaged with scanning electron microscopy, shown in Figure 4.4 and Figure 4.5. These images reveal qualitatively that there are no gross defects on the mating surfaces, and also that the bond

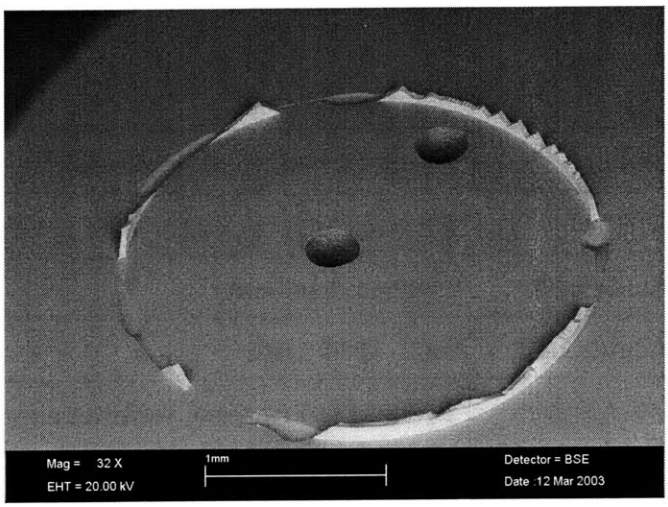

Figure 4.4 SEM Image of Pyrex Base

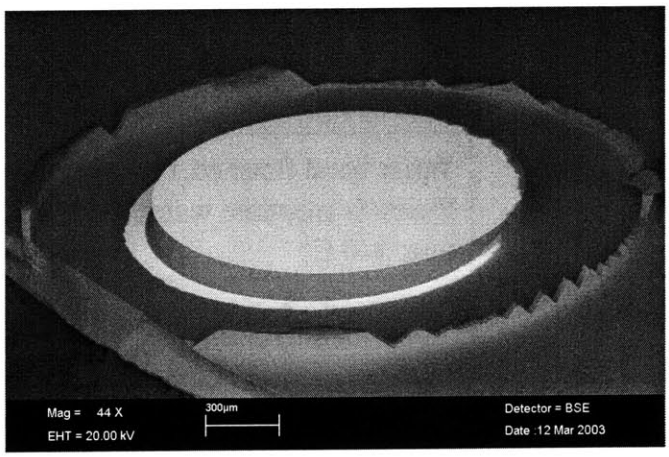

Figure 4.5 SEM of Silicon/Gold Valve Land

strength of the fulcrum to the Pyrex base is extremely strong (it exceeds the fracture

strength of the silicon fulcrum and the Pyrex glass base). Therefore, the isolation of the Nanogate flow chamber from the outside world is assured.

A closer examination of the mating surfaces reveals that there is a slight depression in the Pyrex that corresponds to the location of the silicon valve boss. This is indicated in Figure 4.6. A high magnification view of the edge of the silicon valve land (Figure 4.7)

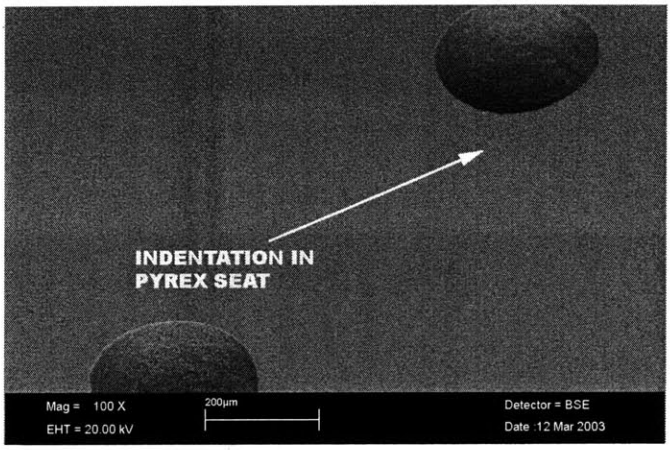

Figure 4.6 Indentation in Pyrex due to silicon boss.

shows that the gold layer there has a very rough edge, which would not be expected unless there was some adhesion during bonding between the Pyrex valve seat and the gold film applied to the silicon boss.

Quantitative information about the quality of the mating surfaces was obtained by optical profilometry. The Pyrex base is shown in Figure 4.8. A more detailed examination of the valve seat alone (Figure 4.9) indicated that the surface roughness was on the order of 3-4 nm rms (excluding the effect of the center hole), and the peak to valley bow / warp is approximately 20 nm (excluding dust particles) although the plastic deformation of the Pyrex seat during bonding likely deformed the Pyrex seat so that it was complementary to the silicon boss.

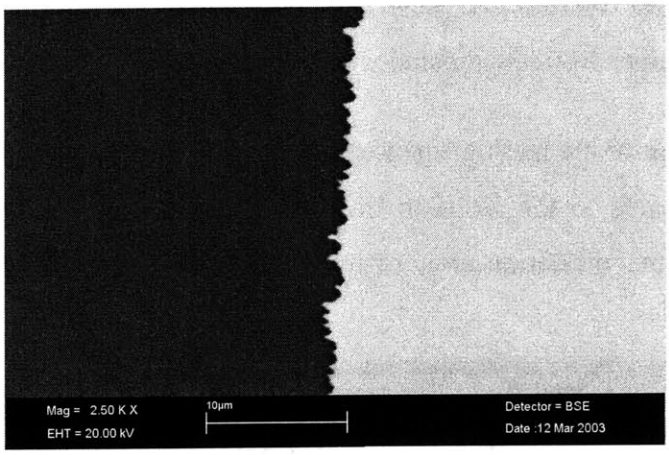

Figure 4.7 Roughness on edge of gold coated silicon boss.

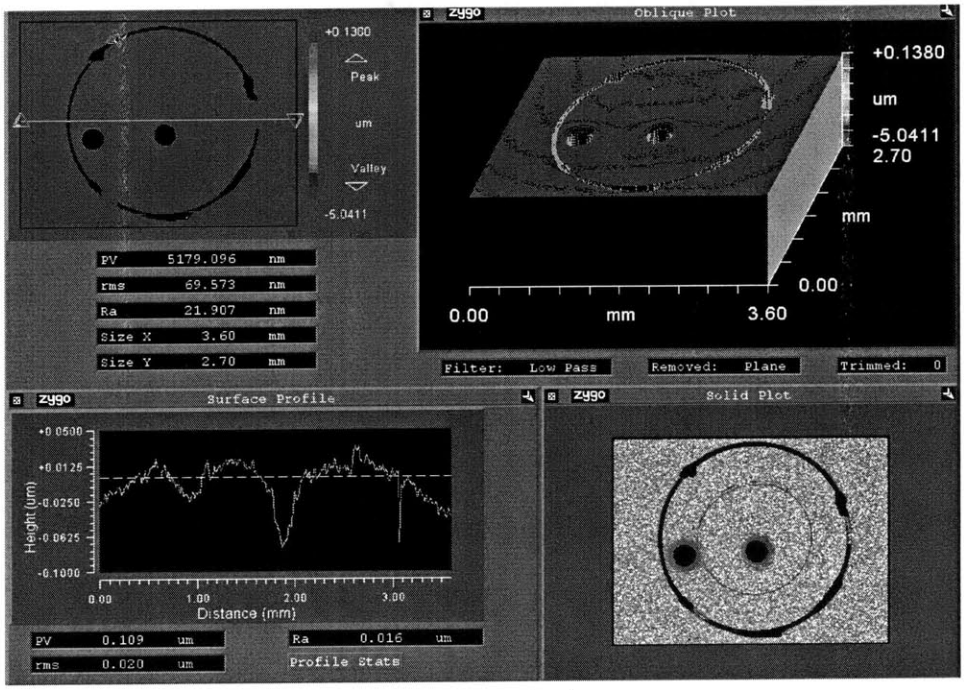

Figure 4.8 Optical profilometry of Pyrex valve land.

Examining the silicon boss yielded similar data. A scan of the entire boss is shown in Figure 4.10, with two regions of interest. One is a depression that encircles the location of the inlet hole (when the Nanogate is assembled), another is a region that is not completely covered with gold due to defects in the shadow mask. Examining the valve mating surfaces directly, shown in Figure 4.11, the surface roughness is 3 nm rms and the surface

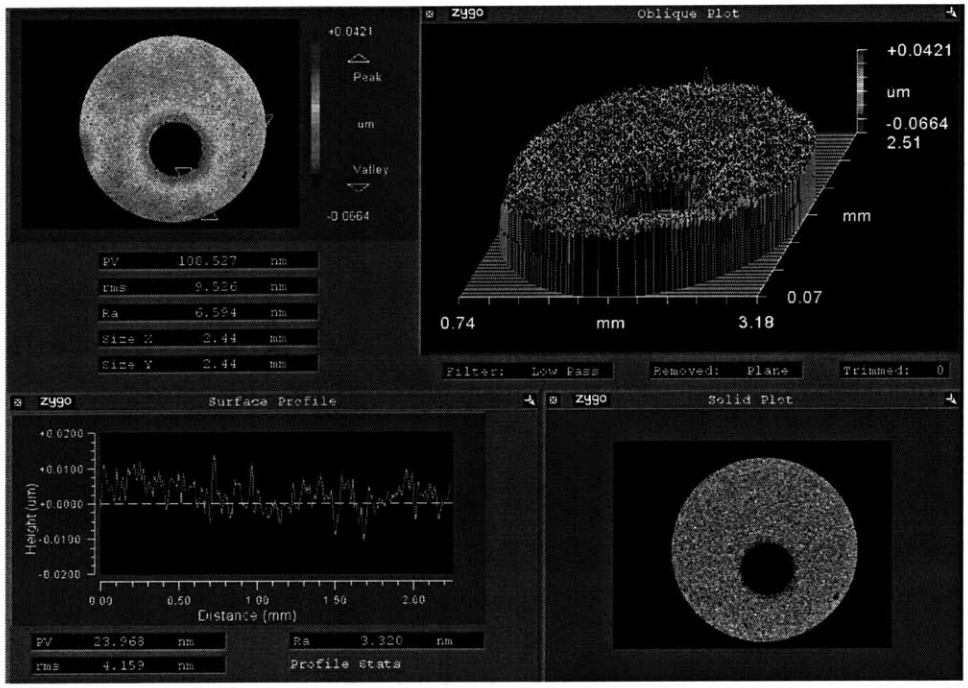

Figure 4.9 Detail of Pyrex valve seat

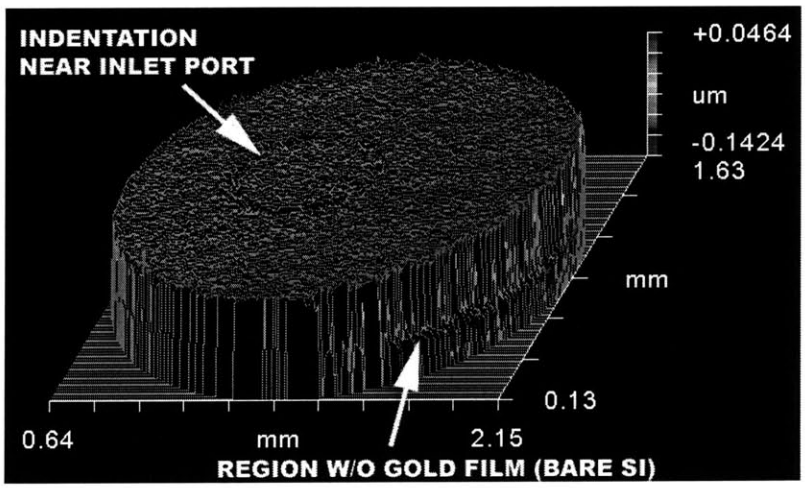

Figure 4.10 Profile of silicon boss.

flatness is 12 nm. The negative skewness defects approximately 100 nm in depth were examined in more detail in Figure 4.12. It is speculated that these defects are regions where AuSi eutectics have formed, which are brittle and also have some chemical affinity for Pyrex. Examining the corresponding regions on the Pyrex wafer reveals that comple-

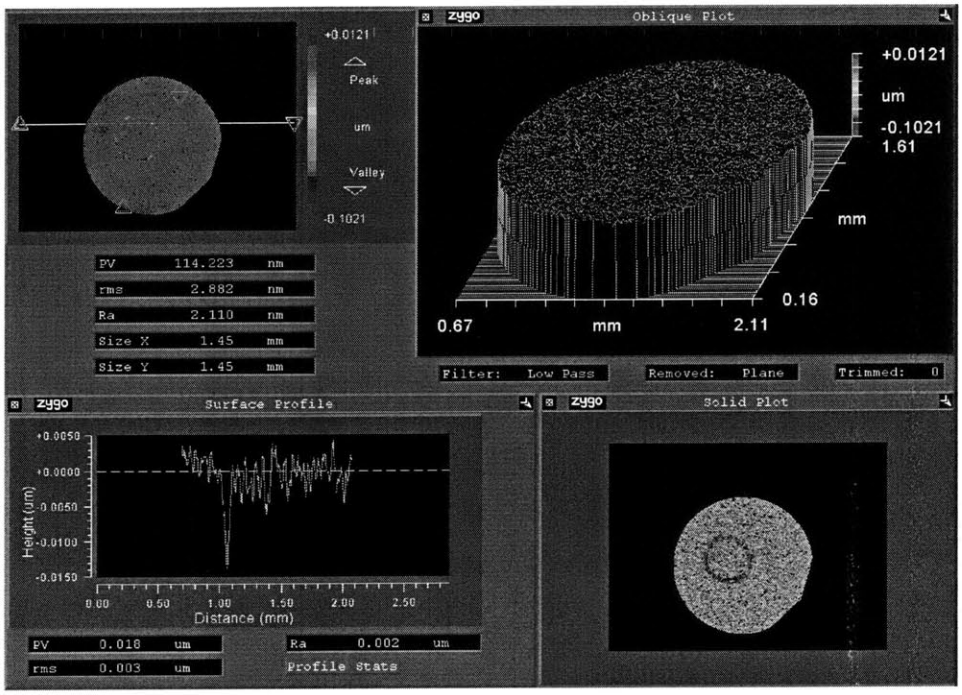

Figure 4.11 Detail of silicon boss.

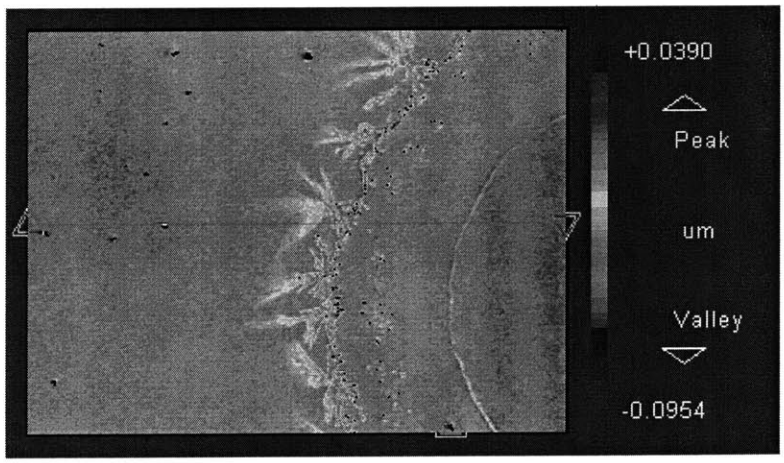

Figure 4.12 Detail of AuSi eutectic

mentary structures exist there, as in Figure 4.13. These formations will not preclude sealing, provided that the motion of the Nanogate is completely repeatable, and lateral displacements of the silicon boss are precluded. Mechanically, the stiffness of the gate in lateral deformation is many times greater than for vertical deformations, so this assump-

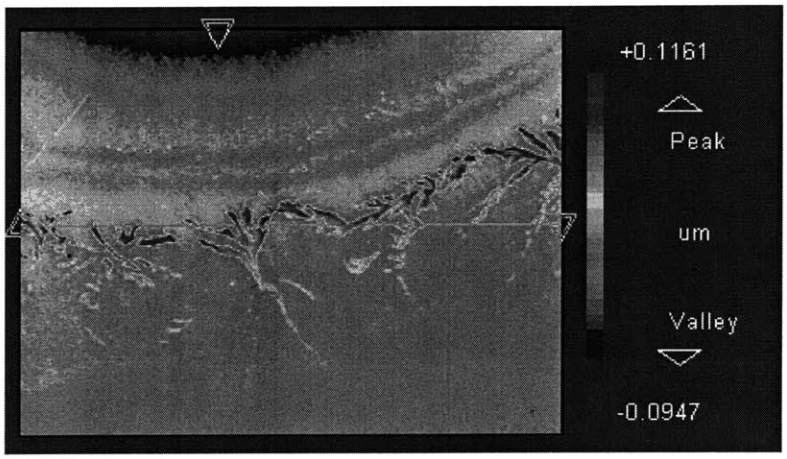

Figure 4.13 Detail of complementary AuSi deposits on Pyrex surface

tion is not unreasonable. A simple countermeasure to this effect is to substitute platinum instead of gold as the metal film. Platinum silicide is normally formed by annealing a platinum film deposited on a silicon wafer at 800 ^{o}C. Therefore, no eutectic is expected to form during anodic bonding.

4.4 Macroscopic Nanogate - Fabrication

The entire Nanogate assembly, including the alignment tube is shown in Figure 4.14. All of the Nanogate parts were machined from 6160 Aluminum. Parts where the surface finish was critical were diamond turned to a roughness of 10 nm. In the vicinity of the valve land, corrosion was also anticipated to be a problem, therefore that region was plated with a nickel-phosphorous alloy that was then diamond-turned. This coating improved the scratch tolerance and surface finish slightly over the diamond-turned aluminum alloy. The manufacturing drawings for each part are included in Appendix D. Pictures of the finished parts are shown in Figure 4.15, Figure 4.16 and Figure 4.17. Three 2.5 mm drill blanks were used for alignment of the wafer and load cap during assembly and operation. However, these proved inadequate in controlling the tilt of the wafer and load cap, which is a weakness in the design that will be addressed in the future.

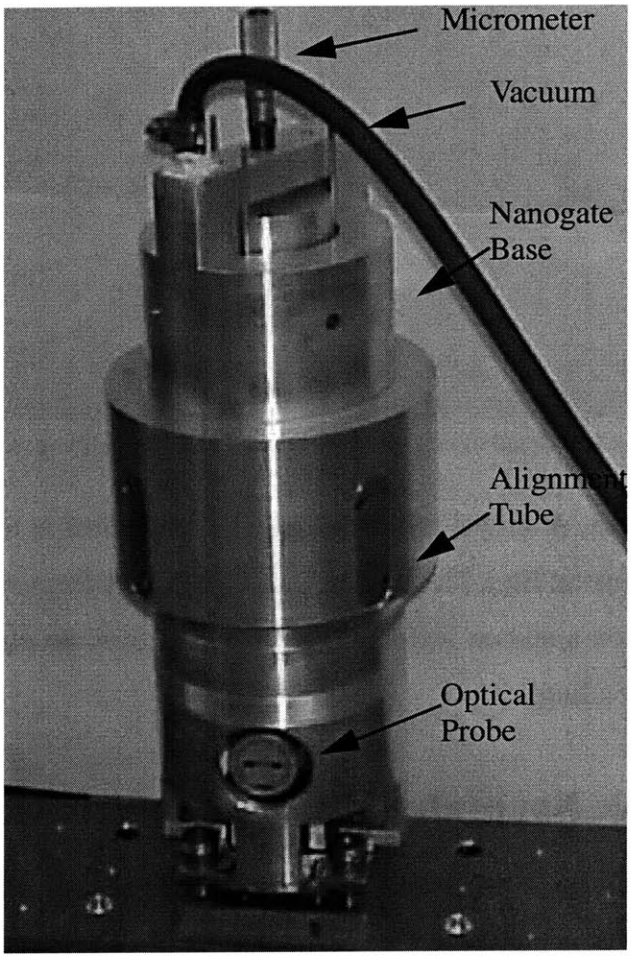

Figure 4.14 Macroscopic Nanogate assembly.

4.4.1 Flexure Selection

Numerous flexures were investigated since sealing in the macroscopic Nanogate was problematic. Initially, conventional single-side polished 2" diameter silicon wafers were used, with poor results. First, the strength of the silicon wafers was significantly lower than expected, likely due to stress concentrations on the unpolished backside of the wafer. Second, the inherent bow and warp (nominally 25 microns over the diameter), combined with the thickness variation (nominally 7 microns over the diameter) prevented sealing. A third issue was the mounting of the preload spring. Mounting the preload spring against the bare silicon wafer was totally ineffective. An intervening foam disc distributed the

Figure 4.15 Diamond turned Nanogate load cap with spring.

Figure 4.16 Diamond turned base plate.

load such that sealing could be partially implemented. However, an effective method of mounting the preload spring would need to be done; however, given the success of the MEMS Nanogate, it is unlikely to be developed.

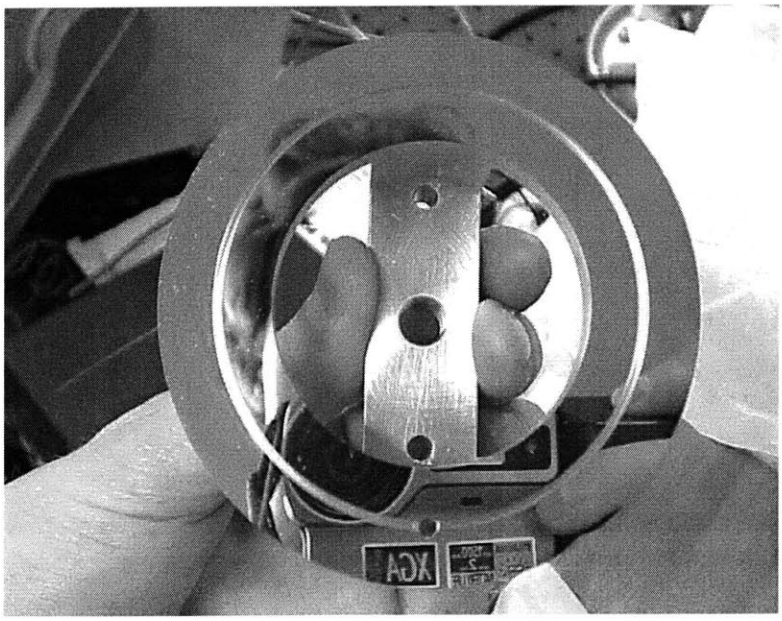

Figure 4.17 Diamond turned Nanogate frame.

The second flexure that was attempted was a double-side polished, ultra-flat silicon wafer. For these wafers, the total thickness variation across the diameter was less than 1 micron. The bow/warp specification was not improved. Double-sided polishing improved the strength of the wafers, but sealing was not satisfactory.

The third type of 'flexure' that was attempted was a 1.5 mm 'ultra-flat,' mirrored glass disc. The flatness of these discs was on the order of 5 microns bow/warp. However, the smaller bow/warp specification was obtained at the expense of flexural stiffness. Therefore, the preload force was unable to seal the flexure, so this was an unsatisfactory solution.

The fourth flexure prototype employed a compliant intervening layer between the 'hard' silicon flexure and the valve land. This presented a great challenge in material selection, since, as mentioned in Table 2.3 on page 27, most soft polymers are highly permeable to gases. Once a suitable material was identified (Spectralon and Vespel were both candidates), thin 1/16", 2" diameter discs of the materials were machined. These discs were then mounted on the frontside of a silicon wafer. It was postulated that the compliance of

these materials would cause them to seal effectively against the valve land. However, more detailed analysis of the manufacturing of compound wafers, and application of pre-load forces would be needed before this could be asserted conclusively.

Chapter 5

PACKAGING

Packaging is possibly the most significant obstacle to the use and commercialization of many MEMS devices. A well-designed package should be thermally and mechanically stable, protect the silicon device from impact, provide optical, electrical and fluidic interconnects as needed, and hermetically encapsulate as necessary parts of the device. In the case of the Nanogate, designing and fabricating a suitable package was a major obstacle since microfluidic interconnects are almost entirely non-standard components.

For the Nanogate, the broad range of tests and applications that were envisioned also put substantial constraints on the types of packages that could be considered. The final package had to withstand high vacuum, pressures up to 100 psi, with both gases and liquids. The package had to be mechanically robust, to withstand clamping forces, and thermally stable, to prevent distortion of the MEMS components and thermal drift in the measurement apparatus. A means to provide optical access for the laser interferometer was also necessary. An interface to standardized macro-fluidic interconnects was optional, but proved very useful in practice.

Three approaches were considered, each derived from commonly used microfluidic packaging techniques. The first approach employed silicone (PDMS) microchannels, bonded to the Nanogate diaphragm, as shown in Figure 5.1. The second approach used eutectic bonding to mate the finished silicon and Pyrex die to a machined Kovar manifold, as in Figure 5.2 and Figure 5.3. The last, and most robust approach, used Pyrex optical flats that

were machined to accommodate standardized 1/8" tubing. These machined Pyrex flats were then anodically bonded to the finished silicon Nanogate dies, creating a leak-tight, irreversible seal.

5.1 PDMS Manifold

This technique reproduced the methods commonly referred to as soft lithography [Duffy, 1998]. Soft lithography typically involves casting a PDMS replica of a machined or etched master, and then bonding this PDMS microfluidic master to a glass slide or other smooth, chemically suitable surface. The exposed PDMS is etched briefly in an oxygen plasma, which creates a hydrophilic surface with dangling OH^- molecules. These then bond strongly to the glass surface, assuming that the PDMS is sufficiently smooth and flat, and that both surfaces are clean and particle-free.

One weakness of the PDMS/soft lithography approach is that only liquids that do not attack the silicone could flow in the system. Water, buffer solutions and some solvents (e.g. methanol) are acceptable; however acids and strong solvents cannot be used, for example. Furthermore, silicone is highly permeable to gases and cannot withstand high vacuum without outgassing. This packaging technique would therefore only be suitable for water or buffer solutions, and gases at atmospheric pressure where cross-contamination between samples to due outgassing was not a concern. This restriction is not typically a great concern for applications in the handling of biological samples, and given its apparently simplicity and utility, it was decided to implement this technique for the Nanogate.

Interconnect holes were DRIE etched in the top of the Nanogate diaphragm. A 3mm diameter silicone 'cork,' with 300 micron flexible quartz capillary tubes embedded into it, was cast, cured, and then bonded to the top silicon diaphragm, as shown in Figure 5.1. The silicone 'corks' were prepared according to the standard process given in Appendix A. In the case of the Nanogate, the bond strength of the PDMS-to-silicon interface was very weak, and a robust seal could not be formed. It is speculated that this was due to higher surface roughness, despite the silicone being molded against the surface of a glass slide, as well as

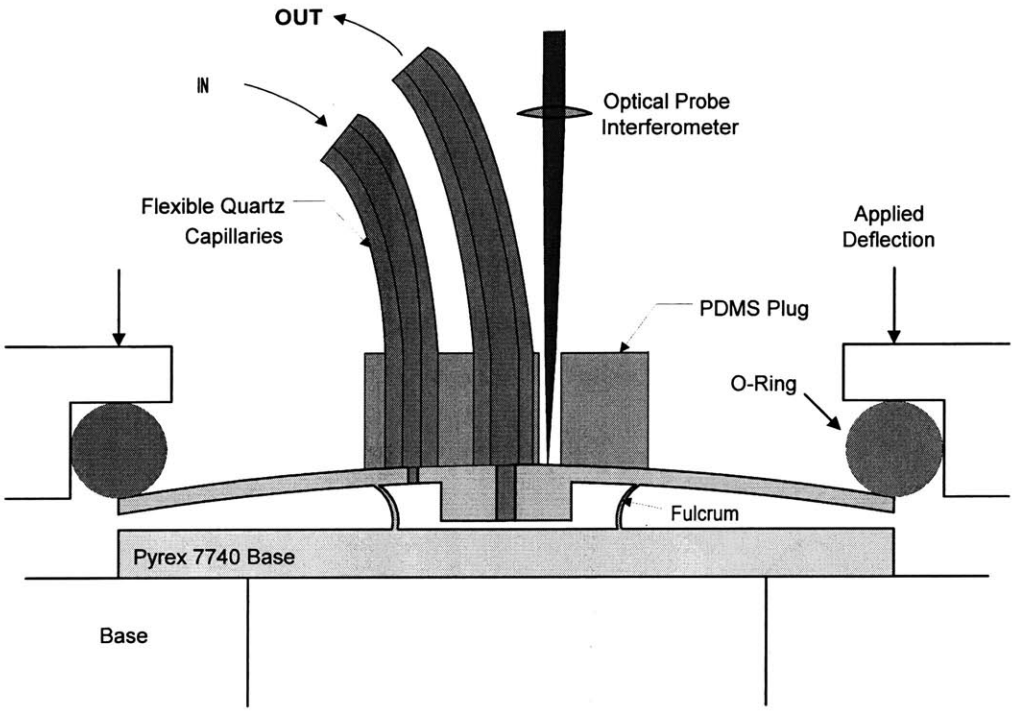

Figure 5.1 Cross-section of PDMS microfluidic package design.

the small size (high aspect ratio) of the cork, i.e. it was too stiff compared to the surface energy of bonding.

5.2 Eutectic Bonding to Kovar Manifold

This packaging technique is widely employed in military electronics and optics applications which require very robust, hermetic encapsulation. Kovar is an alloy of Iron, Nickel and Cobalt whose thermal expansion coefficient is very close to Pyrex glass and silicon. Therefore, it is an ideal choice for packaging silicon devices. Another big advantage is that Kovar can be machined, threaded, welded, stamped, etc. which simplifies the interface between the package and other systems. In this system, electrical connections through the gold plated Kovar package are typically formed by bonding the wire into the Kovar with a glass frit. Then a Kovar cap (drawn or machined), is eutectically bonded to the

Kovar base with a gold and tin (AuSn 80/20) alloy preform. The AuSn preform melts at 280°C, and the cap and base are hermetically sealed together.

Machined Kovar parts were fabricated as shown in Figure 5.2 and Figure 5.3, and plated with nickel, then gold. Fabrication drawings are in Appendix D. The drilled Pyrex die was sputtered with an adhesion layer of Cr (100 nm)/Ni (1.5 um)/Au (3 um). AuSn 80/20 eutectic performs were positioned at the interface between the Kovar manifold and the Pyrex/Si die, and the assembly was put through a thermal cycle to melt the eutectic and seal the package.

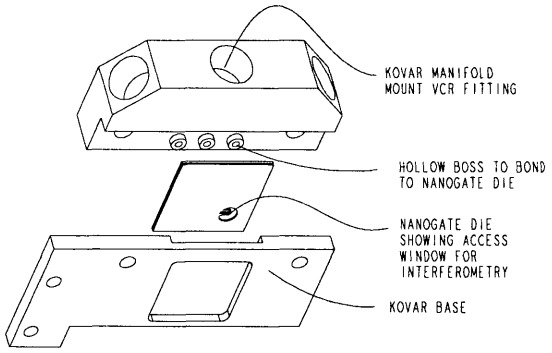

Figure 5.2 Exploded view Kovar Package

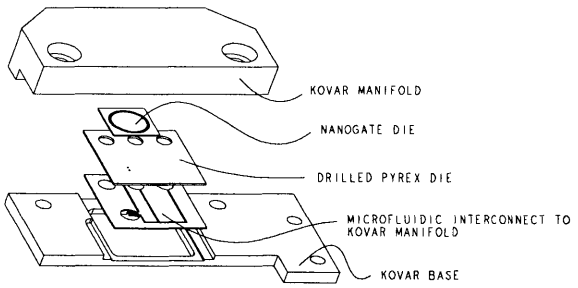

Figure 5.3 Exploded View Nanogate Package and Die

The large thermal mass of the machined Kovar parts, combined with the poor adhesion of the sputtered Cr/Ni/Au film to the Pyrex glass die resulted in a failure of this technique for this application. Furthermore, the machining tolerances required to preserve an adequately close fit between the Pyrex die and the Kovar manifold added substantial expense. To successfully mate Pyrex or silicon to Kovar, a ground surface finish would be required, along with a long thermal cycle and adequate clamping to ensure that the preform would melt completely and occupy the void between the die and the metal. It was determined that we should immediately move towards a lower risk approach using machined Pyrex glass manifolds, discussed in Section 5.3.

5.3 Anodic bonding to Machined Pyrex Manifold

Anodic bonding is a technique whereby silicon and Pyrex 7740 glass, which have matched thermal expansion coefficients, are permanently bonded through the application of high temperature (350 to 400 ^{o}C) and high voltage (800-1000 V). This technique has the benefit that it is robust in the presence of surface irregularities and particulates, and provides an irreversible, hermetic seal. It is therefore ideal for a packaging process which must be undertaken after die sawing where small particles may be present due to the slurry residue. Furthermore, anodically bonded parts are leak tight, robust in the presence of thermal fluctuations and mechanically stable.

A commercial grade 1" x 1" x 1/4" Pyrex glass window was purchased from Esco Products, Inc. (New Jersey). Three ports were drilled into the Pyrex window to make fluid connections from the silicon die to the 1/8" Kovar tubing, as shown in Appendix D. The machined Pyrex glass manifolds were cleaned in "Piranha" (3:1 H_2SO_4:H_2O_2) for 10 minutes to remove organic contaminants, rinsed in DI water for 10 minutes, then dried. The bonding surfaces of the Nanogate die and the Pyrex manifold were cleaned with a lens tissue and a few drops of methanol, then mounted in contact using a Macor alignment jig. These were then heated and anodically bonded at 350^{o}C with 1000V for 5 minutes. 1/8" diameter Kovar tubes were cut to length, deburred and fitted with standard 1/8" Swagelok fittings. Kurt Lesker KL-5 leak sealant epoxy was used to bond the Kovar tube into the Pyrex base. The finished assembly was cured in an oven at 135^{o}C overnight.

During testing, the final packaged device was able to maintain high vacuum (10^{-7} Torr), high pressure (over 100 psi), and withstand high temperatures, up to 200 ^{o}C without degradation. It is also mechanically stable and resistant to shock. One shortcoming is that the leak sealant epoxy dissolves in methanol or other solvents. Therefore, the use of these liquids is restricted to short intervals. A new epoxy which has superior solvent resistance but similarly good outgassing properties is currently under investigation. Another possibility is to frit bond the Kovar to Pyrex glass as is common practice in industry. This packaging

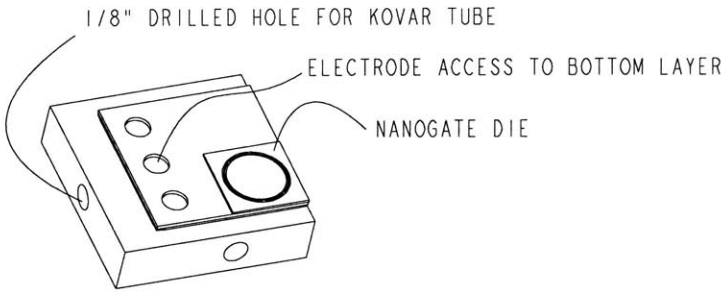

Figure 5.4 Nanogate die bonded to Pyrex Base

technique was accepted as the "optimal solution." A finished, packaged device is shown in Figure 5.5 and Figure 5.6.

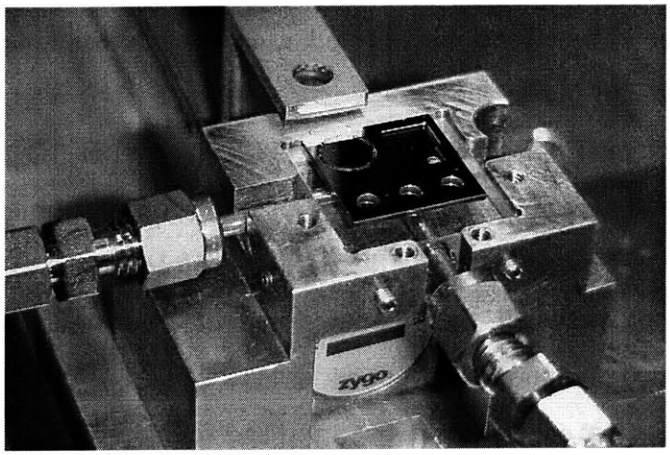

Figure 5.5 Photograph of packaged Nanogate in test apparatus.

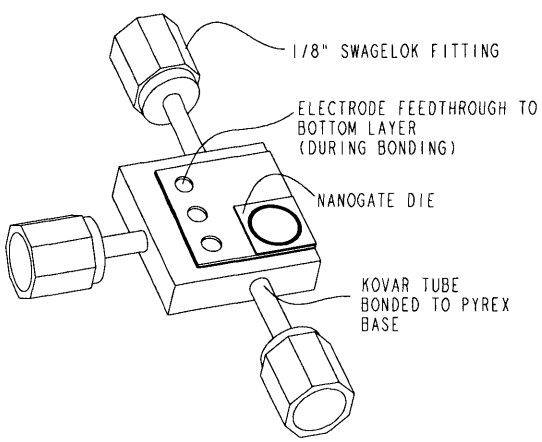

Figure 5.6 Packaged Nanogate (3-port device).

Chapter 6

INSTRUMENTATION

The testing of the Nanogate was a challenge. To make measurements on a nanometer length scale, the apparatus must be extremely stable. Disturbances such as air currents, vibrations, thermal fluctuations, pressure spikes in fluid channels, and particulates must all be mitigated. Furthermore, the functions of actuation, displacement sensing and fluid connections must all be integrated into a mechanically rigid, thermally stable apparatus. The final design, which relied extensively on Super Invar components, was able to achieve thermal drift of less than 30 nm per hour, and vibration stability which was far below the detection limit of the interferometer.

6.1 Macroscopic Nanogate

The macroscopic Nanogate was not subjected to extensive testing because of the previously indicated leak problems. However, preliminary testing was done to confirm the expected performance of the device. Displacement was measured with the Zygo optical probe. This measured the displacement of the reflection of a focused beam with a resolution of 2.4 nm. The primary difficulty associated with setting up this measurement apparatus was alignment of the reflective wafer to the interferometer optics. This was accomplished by mounting both the Nanogate and the interferometer in a threaded alignment tube, shown in Figure 6.1. The Nanogate base plate was brought into focus by advancing the threaded tube. The thread on the tube is an extremely fine 80 pitch, so this

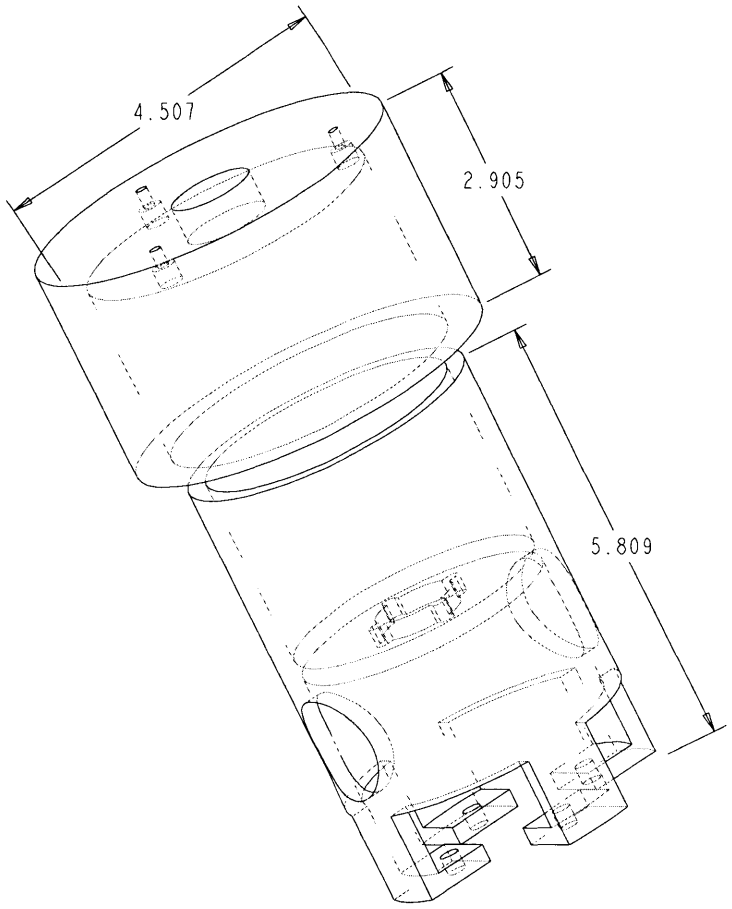

Figure 6.1 Threaded alignment assembly.

provided accurate focusing. Since the flowrate measurement apparatus require a thermally isolated enclosure, this entire assembly was then bolted to an igloo cooler. The thermal drift of this apparatus, due to its aluminum construction, was on the order of 200 nm/hr. This, combined with the many fundamental leakage flaws of the macroscopic Nanogate, led to the development of the much stiffer, more easily assembled, and more thermally stable MEMS test apparatus described below.

6.2 MEMS Nanogate Test Apparatus

The first prototype of the Nanogate test apparatus was machined from Aluminum parts that were bolted together. This arrangement proved to be a failure since the thermal expan-

sion of Aluminum contributed to huge thermal drifts of 225 nm/min, that could not be prevented by insulation in test cases! Furthermore, the mechanical rigidity of the initial design was insufficient to reduce vibration noises below the 2.4 nm sensitivity of the interferometer. The second iteration of the Nanogate test apparatus was designed to have two rigid structural loops which decoupled the displacement (interferometry) sensing from the actuation. All components were machined from Super Invar, which has a thermal expansion coefficient of 6 x 10^{-7}/°C, lower than any other commonly available metal. The basic components of the final test apparatus are shown in Figure 6.2.

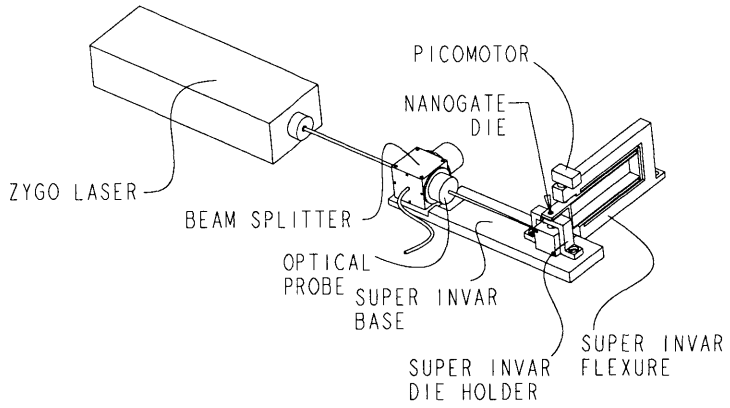

Figure 6.2 Nanogate Test Apparatus

This apparatus, when stable and housed in its thermal isolation enclosure, has thermal drift of less than 30 nm/hr in the measurement loop, and no measurable change in the applied displacement over time other than transient relaxation of the elastomer O-ring that sits between the Nanogate diaphragm and the flexure. Furthermore, the stiffness of the fixture assembly, when damped with a sheet of viscoelastic material, is sufficient to prevent vibrations that can be detected by the interferometer. A 1L stainless steel vessel with an attached pressure sensor is used to provide a steady pressure to the inlet of the Nanogate in the Helium leak test. 1/8" stainless steel tubing and Swagelok fittings are used for all other fluid connections. For liquid flow tests, a syringe pump drives the flow into the Nanogate, and a pressure tap in the inlet line sets the inlet liquid pressure.

6.2.1 Design of Picomotor-Flexure Assembly

The design of the Super Invar flexure used to transfer displacements from a New Focus[1] Picomotor to the Nanogate diaphragm will be discussed in detail. The goal was to translate tiny motions from the ball end of the picomotor driver to the O-ring mounted over the Nanogate. It was necessary to optimize the flexure for purely linear motion, avoiding any arcuate motion that is characteristic of a flexure element, and it was also necessary to provide a sufficient range of motion to allow for variations in the vertical dimensions of the Nanogate (due to changes in the process flow, wafer dimensions, etc.).

The basic structure is shown in Figure 6.3. It has a range of motion of 3.2 mm (1/8"), and

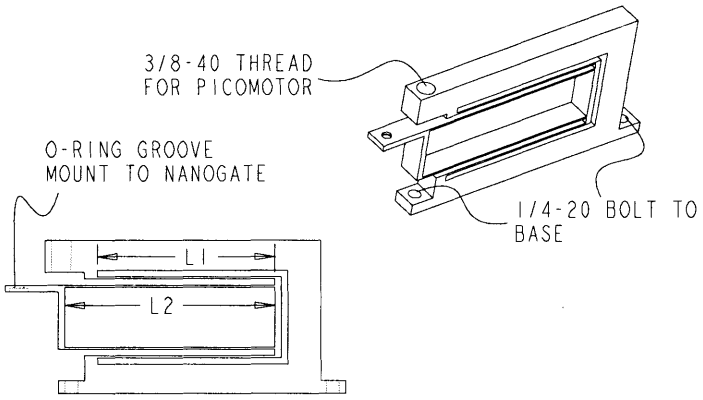

Figure 6.3 Super Invar Flexure

an angular tilt of 1 x 10^{-5} degrees per 100 microns of travel. An ideal design would have no angular tilt at the Nanogate mount, but this was precluded by the geometric constraints of the apparatus. The angular tilt was determined by finite element analysis, and also by simple mechanics, as shown below. The bending of a rectangular beam for an applied force (F) or moment (M) is given by the equations in Table 6.1, where E is Young's modulus and I is the area moment of inertia about the bending axis.

1. New Focus, Inc. www.newfocus.com

The flexure used in the Nanogate can be idealized as two parallelogram-type linkages con-

TABLE 6.1 Vertical and Angular Deflection of a Beam Under Various Loadings

	F	M
δ	$\frac{FL^3}{3EI}$	$\frac{ML^2}{2EI}$
θ	$\frac{FL^2}{2EI}$	$\frac{-ML}{EI}$

nected in series, and is shown in Figure 6.4. The relevant dimensions of the flexure are

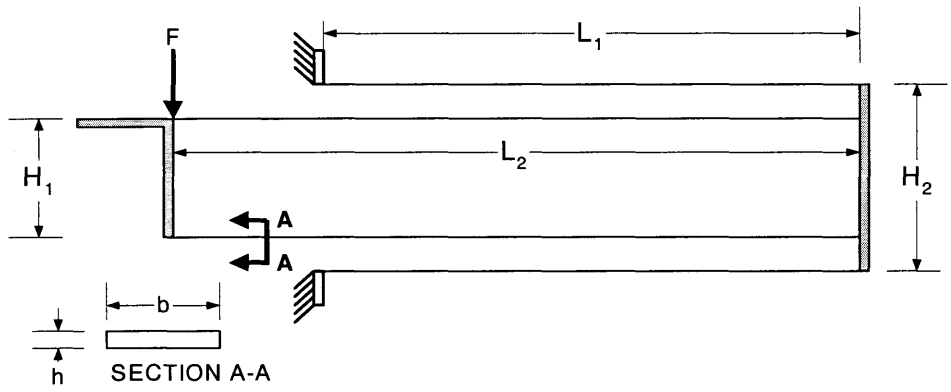

Figure 6.4 Super Invar flexure schematic.

summarized in Table 6.2. The maximum deflection of each parallelogram structure is given by:

$$\delta = \frac{-FL_2^3}{12EI}, \tag{6.1}$$

where F is the applied force, E is Young's modulus (150 GPa for Super Invar), and I is the moment of inertia of each flexure arm, given by:

TABLE 6.2 Dimensions of flexure

Parameter	Value (mm)
L_1	84.3
L_2	101.4
H_1	39.1
H_2	30.0
b	12.7
h	1.0

$$I = \frac{bh^3}{12}. \tag{6.2}$$

The maximum deflection of the flexure, for an applied load of 1N, is 0.433 mm. There is also a small rotation of the flexure due to the moment FL_2 applied to the end of the short flexure L_1. This is compensated for by the separation H_2 of the two flexure arms, and is insignificant in this case ($\theta = 6.0 \times 10^{-6}$ rad). A more detailed analysis by finite element methods gives a total deflection of 0.451 mm and a rotation of 1.0×10^{-5} rad, as shown in Figure 6.6 and Figure 6.7. The larger rotation is obtained by accounting for the deformation of the C-shaped base of the flexure, but the results are otherwise in good agreement with theory.

In practice, the Super Invar flexure will vibrate and oscillate with very little damping given the slightest disturbance. Therefore, it is essential to apply a layer of visocoelastic damping tape[1] to the entire flexure to dissipate these vibrations and give a stable structure, as shown in Figure 6.5. This viscoelastic damping tape will also add to the stiffness of the structure, but creep of the visocoelastic material is not an issue, since the Picomotor applies a fixed displacement, as opposed to a force, to the flexure structure. Thus, the applied displacement remains constant even as the tape relaxes over time.

1. EAR C1002, www.confor-med.com

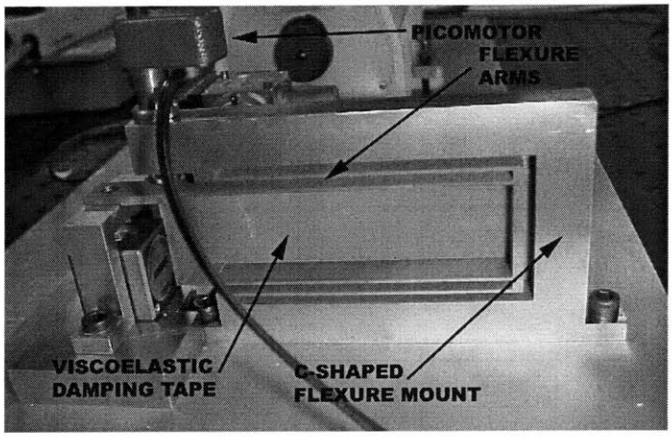

Figure 6.5 Super invar flexure, as fabricated.

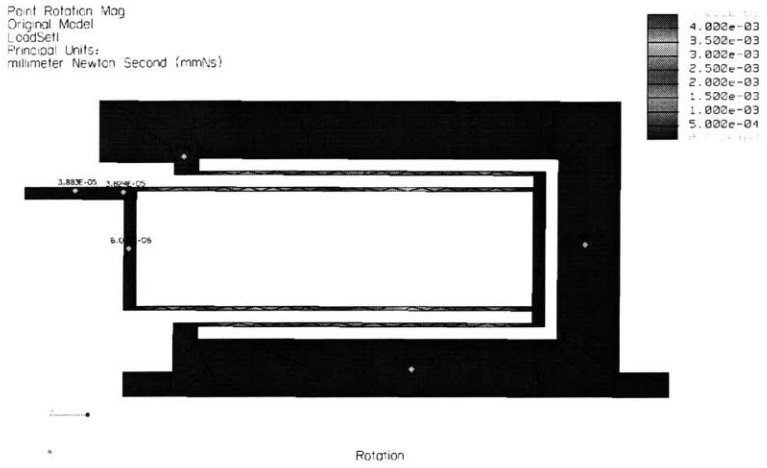

Figure 6.6 Rotations of Super Invar flexure

6.2.2 Sensitivity and Stability of Interferometer

The refractive index of air is a function of both temperature and air pressure. Given the 6" deadpath of the Zygo single-point interferometer, this is a substantial source of error in the displacement measurement. Nominally, the refractive index of air at 15 ^{o}C, at 632.2 nm, is [CRC, 2000]:

$$n_{15} - 1 \; = \; 2.7656 \times 10^{-4}. \tag{6.3}$$

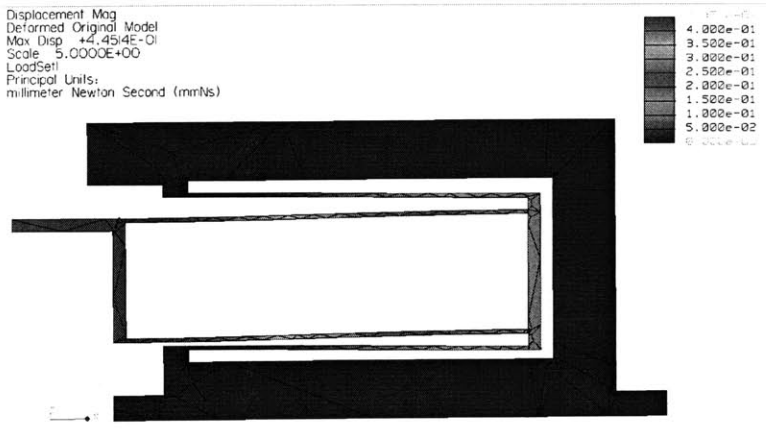

Figure 6.7 Deflection of Super Invar flexure

The refractive index must be multiplied by the following dimensionless factor, which depends on the surrounding temperature and air pressure:

$$K = \frac{p[1 + p(61.3 - t) \times 10^{-10}]}{96095.4(1 + 0.003661t)}. \tag{6.4}$$

Therefore, a change in the refractive index of the deadpath of air (153.4 mm) between the reference beam in the interferometer optics, and the test piece under measurement, will case a change in the measured (as opposed to actual) displacement of Δl:

$$\Delta l = \Delta n \cdot l_d \cdot 2, \tag{6.5}$$

where l_d is the deadpath of the interferometer and Δl is the change in the measured path. Δn is the change in refractive index, given by:

$$\Delta n = (n_{15} - 1)(K - 1), \tag{6.6}$$

where n_{15} is the refractive index of air at 15 ^{o}C. In the current experimental setup, a one degree change in air temperature results in a change in the measured displacement of 287 nm. This strongly motivates a measurement technique, for example capacitive measurement, that is referenced directly to the boundaries of the Nanogate gap, as opposed to the interferometer cube located 6" away. This sensitivity also serves to explain why air cur-

rents, which cause minute changes in temperature (and hence refractive index) in the path of the interferometer beam, cause such a disturbance in the measurement of the gap.

6.3 Determining Liquid Leak Rate

Extremely small liquid leaks are not often a subject of commercial interest; for this reason, commercial leak rate detectors do not have adequate sensitivity to measure the leak rates that are observed in the Nanogate. The technique of observing a bubble in a capillary or microchannel was instead adopted. A serpentine microchannel was fabricated at the outlet of the Nanogate as shown in Figure 6.9 and Figure 6.8. A microscope and illumination system were mounted to observe the progress of the meniscus through the microchannel. The volume of the microchannel (determined by optical profilometry), divided by the time for it to be filled, gives the average flowrate over the measurement interval:

$$Q_{liquid} = \frac{V_{outlet}}{t_{meniscus}}. \tag{6.7}$$

A second bypass microchannel was also fabricated, which permits the serpentine measurement channel to be flushed. The measurement can thus be restarted. Small, passive flow restrictions were put in place to prevent backflow of test liquid into the flush channel during the test interval. A more sophisticated implementation of this structure could, for example, use a capacitance measurement across the microchannel to determine exactly when the meniscus has passed the start and end positions. In the current implementation, this is done manually.

When the meniscus is observed to pass the start position, the start time, and gate position are both recorded. During the course of the measurement, uncertainties in the measurement of the Nanogate opening lead to significant uncertainties when attempting to correlate the measured data to theoretical predictions. Therefore, an optimization parameter is the length, in time, of the expected measurement. A shorter measurement time will reduce the uncertainty in the position measurement over the course of the flowrate measurement.

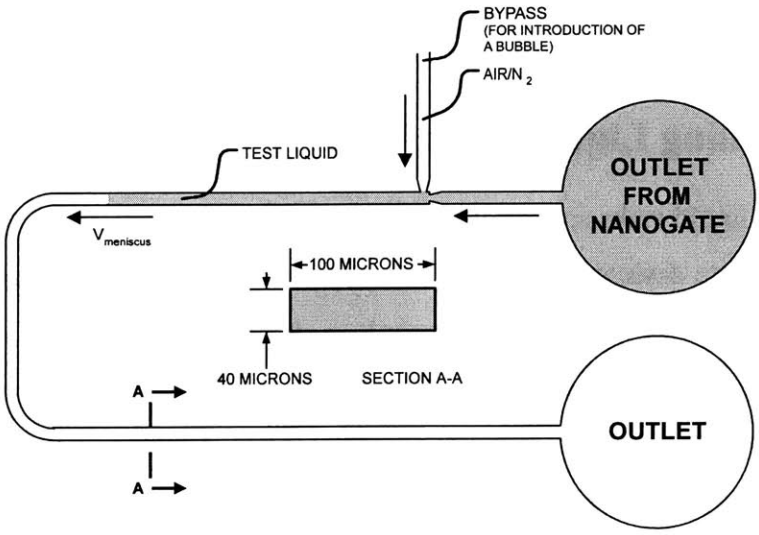

Figure 6.8 Schematic of Nanogate Flowrate Test Structure

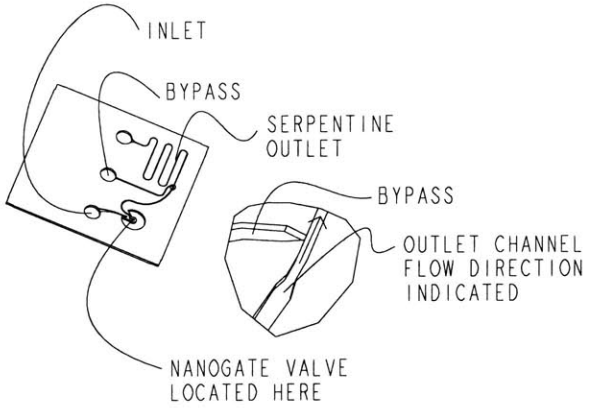

Figure 6.9 Detail of outlet channel.

However, the uncertainty in the determination of start and end-points of the flowrate measurement will also impose a practical constraint on the minimum channel size. Another constraint is imposed by the minimum linewidth resolution of the fabrication technique. For this reason, a nominal channel dimension of 100 microns wide x 45 microns deep was chosen. The measurement time for a typical (~100 nm) Nanogate opening and pressure drop of 40 psi is on the order of 30 minutes. Qualitatively, this matches well to the stability of the Nanogate measurement apparatus, on the order of 10 nm within a half-hour interval.

However, the measurement time scales as the cube of the flowrate, thus for very small openings of the Nanogate, the measurement intervals become excessively long.

Chapter 7

TESTING

7.1 Characterization of the Macro Nanogate

To test the sensitivity of the displacement measurement, a simple test of the transmission ratio was performed. The data is summarized in Figure 7.1 below. This test indicated a transmission ratio of 16.8, identical to that predicted by theory in Section 3.1.1. However,

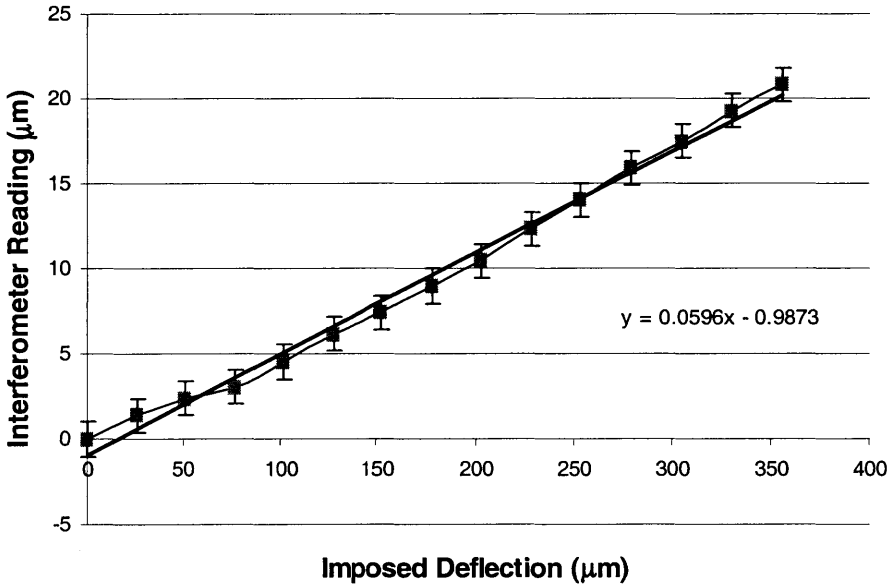

Figure 7.1 Nanogate transmission ratio

the anticipated nonlinear dependence of the transmission ratio on the applied load is not observed. This is due to the manner in which the preload force is applied -- it is not uniform, nor well constrained, so the model does not conform rigorously to reality. In addition, the Nanogate was exposed to thermal fluctuations during the test, which add to measurement errors. Furthermore, the micrometer was actuated manually which adds to potential errors.

7.2 Bubble Test

To determine if the macro-Nanogate (Section 4.4) was leak tight, the input gas line was pressurized with dry nitrogen, and the assembly was immersed in deionized water. If bubbles were observed in this preliminary test, then further flowrate tests were not pursued. This test was a rapid and effective means of determining the required preload pressure, and the suitability of various materials and flexure designs in actual use. However, it suffered from the limitations that the entire Nanogate assembly had to be immersed in water. The vacuum seal between the frame and base plate was simply a bare metal-to-metal seal which relied on highly polished surfaces to seal effectively. When immersed in water, this caused the vacuum pump to draw small quantities of water, which detracted from its performance. Furthermore, the Nanogate had to be inverted which often caused the alignment pins to fall out, leading to excessive tilting and other effects. Despite the effects introduced by the test setup, the bubble test was effective at determining which designs were potential candidates for sealing. While each design ultimately failed utterly, the overall results confirmed the relationship between sealing and preload force, and also motivated the search for sufficiently flat wafers which would not only seal, but which would allow the gap to be opened controllably. The results of the series of bubble tests are summarized in Table 7.1 below.

TABLE 7.1 Results of bubble tests

Test Flexure	Description of Result
Single-side polished silicon, light preload spring applied directly to backside.	No sealing. Free-flowing bubbles.
Single-side polished silicon, heavy preload spring applied directly to backside.	No sealing. Subsequent breakage of wafer during disassembly.
Single-side polished silicon, heavy preload spring applied through foam disc.	Marginal sealing. Can support back pressure of 10 mm H_2O with minor leakage.
2" diameter optical flat.	Seals fully with heavy preload. Stiffness precludes useful measurements and opening. Tilting is problematic since the seal is unstable with small vibrations etc.
Double-side polished silicon, heavy preload spring applied through foam disc.	Moderate sealing. Can support back pressures of 10 psi with minor leakage. Flexure is prone to breakage due to nonuniform application of preload. Tilting is uncontrolled however, and significant leakage from the outside of the flow region is observed.
Double-side polished silicon wafer with diamond-turned Spectralon$^{(TM)}$ sealing layer.	No sealing observed, due to uncontrolled tilting of Spectralon layer.

7.3 Characterization of MEMS Nanogate

The MEMS Nanogate was a substantially more sophisticated, yet in many respects simpler, design than the Macro Nanogate. The testing was therefore divided into testing of the basic flexure and interferometer setup, mechanical testing of the first generation MEMS Nanogates to verify their operation, in collaboration with graduate student Hong Ma, and then final testing of the MEMS Nanogate with integrated microfluidics.

7.4 Mechanical Characterization of Flexure Assembly

The flexure assembly was characterized by interferometry. A silicon reflector was mounted on the end of the flexure in place of the Nanogate. The flexure, picomotor and interferometer assembly were enclosed in an insulated foam box, and allowed to settle

overnight to eliminate transient effects. This setup had short-term (1 hr) thermal drift of 30 nm/hr which was sufficient for all subsequent tests, though not as low as would have been desired. The reason for the higher thermal drift is thermal effects on the deadpath in the interferometer. The Zygo single-point interferometer that was used for testing had a 6-inch long deadpath; the refractive index of air is a function of temperature, therefore a 1-degree change in the ambient air temperature would cause a 30-nm drift in the interferometer measurement, as shown in Figure 7.2. The best way to reduce this drift is to shorten the deadpath, or use an interferometer that uses a much closer reference plane. However, this was not practical in the context of the MEMS Nanogate due to size constraints (the MEMS Nanogate is far smaller than the interferometer).

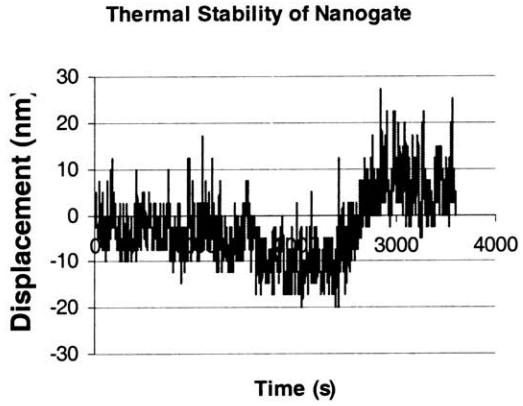

Figure 7.2 Short-term (1 hr) thermal stability of Nanogate system.

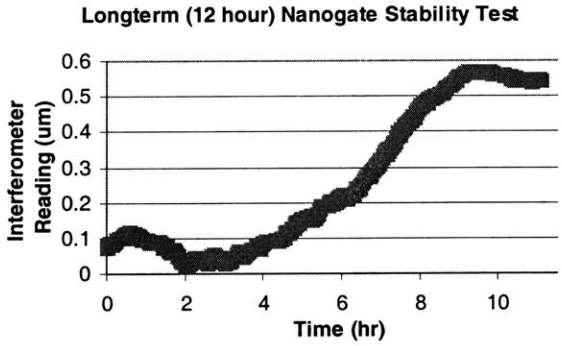

Figure 7.3 Long-term (12-hr) thermal stability of Nanogate system.

Second, the typical step size of the Picomotor[1] was characterized. Since the Picomotor is a friction drive-based device, its response depended on the pulse speed and loading. Furthermore, the response was not entirely repeatable. Therefore, it was necessary to characterize the Picomotor to determine the typical response of the actuator and flexure assembly. This is shown in Figure 7.4. The nominal displacement per applied pulse was 12 nm when the flexure was displaced about its rest position. For a given transmission

1. New Focus, Inc. http://www.newfocus.com

ratio of 16, the displacement of the Nanogate per applied pulse would be 0.75 nm. In the final implementation of the Nanogate, as shown in Figure 7.6, the Nanogate displacement per applied pulse was approximately 0.20 nm, indicating that the Picomotor displacement per applied step dropped significantly under load, to approximately 3.2 nm.

7.5 Mechanical Characterization of MEMS Nanogate

The first prototype MEMS Nanogates, without microfluidic interconnections, were tested

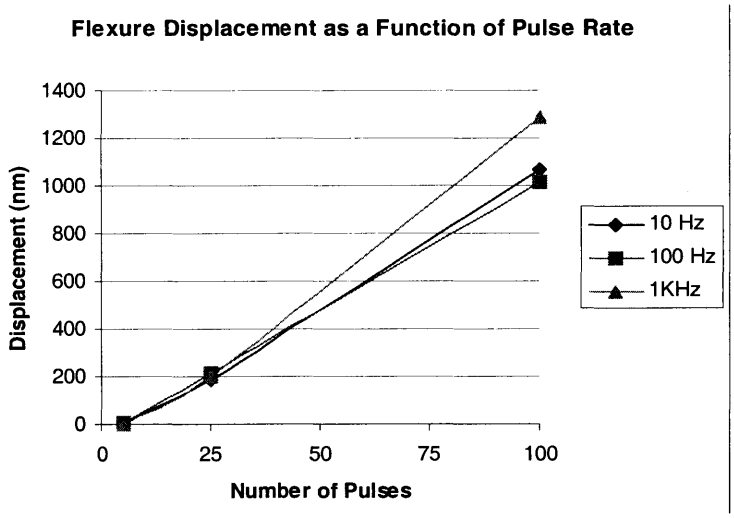

Figure 7.4 Characterization of Picomotor and flexure actuator, unloaded, without Nanogate.

to determine their mechanical response, the minimum step size, repeatability and to see if there was any evidence of stiction or pull-in. The first test was to determine the response of the Nanogate to a single applied picomotor pulse. The Nanogate die was mounted in its holder, and the flexure assembly was fixed in place. The picomotor was manually advanced until some displacement was registered on the interferometer. At this point, it was determined that the O-ring and flexure were in contact with the Nanogate diaphragm. The Nanogate would then be advanced by a given number of steps, and then immediately retreat by the same number of steps. The starting and resting position of the Nanogate were recorded. The results of the repeatability test are shown in Figure 7.5. From this

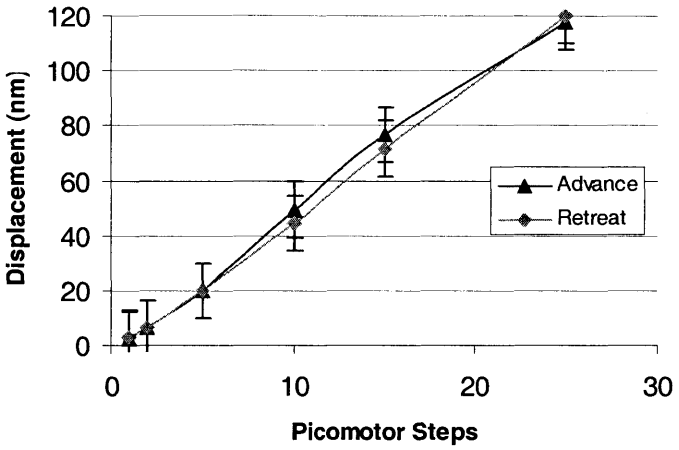

Figure 7.5 Nanogate Repeatability Test

chart, it is apparent that thermal drifts cause the measurement, to have some non-repeatable motion. It is speculated that the gap displacement itself remains stable since, for example, observed flowrates do not vary appreciably over long (30 min.) time scales. In some cases, a thermal drift of 5 nm was observed over the course of the measurement.

Testing of the second-generation MEMS Nanogates revealed a better correlation between the mechanical response and theoretical predictions. The difference between the first and second-generation Nanogates is the bonding of the fulcrum -- more care was taken to preserve the integrity of the bare silicon surface of the fulcrum during processing, and this in turn made the anodic bonding process much more reliable. This is also essential to making a sealed fluid device which can withstand pressure and vacuum applied to the inlet port. The mechanical characterization of the second-generation MEMS Nanogate is shown in Figure 7.6. The measured transmission ratio is 25, and the position change of the gate per applied Picomotor step is 2 Angstroms.

7.6 Helium Leak Test

Helium leak tests were performed using a Varian 979 Helium Leak Tester, which uses a mass spectrometer to determine the leak rate, with mass flow sensitivity of 10^{-10} atm.cc/s. Helium leak tests were performed at room temperature (22 ^{o}C). The machine is self-cali-

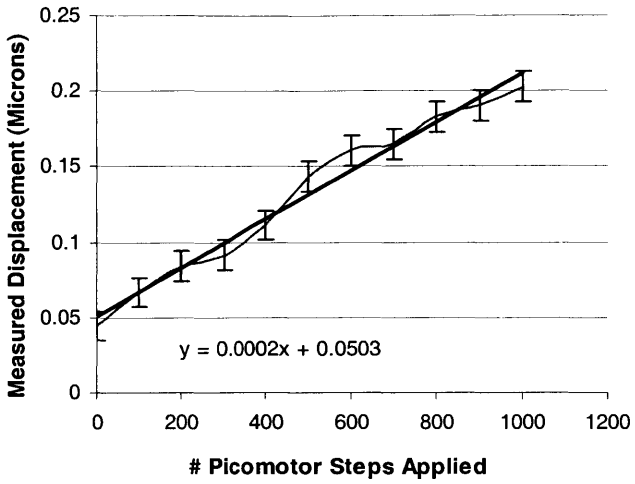

Figure 7.6 Mechanical characterization of MEMS Nanogate

brating, and before any tests are performed, the inlet is sealed, and the machine determines the baseline ('zero') leak rate. The outlet of the Nanogate valve was connected to the inlet of the helium leak tester using a 1/4"x24" flexible stainless steel tube with VCR-4 fittings on each end. The leak rate was then measured, at a given pressure drop, for a range of valve openings. The data (for a given Nanogate artifact), is summarized in Figure 7.7. The

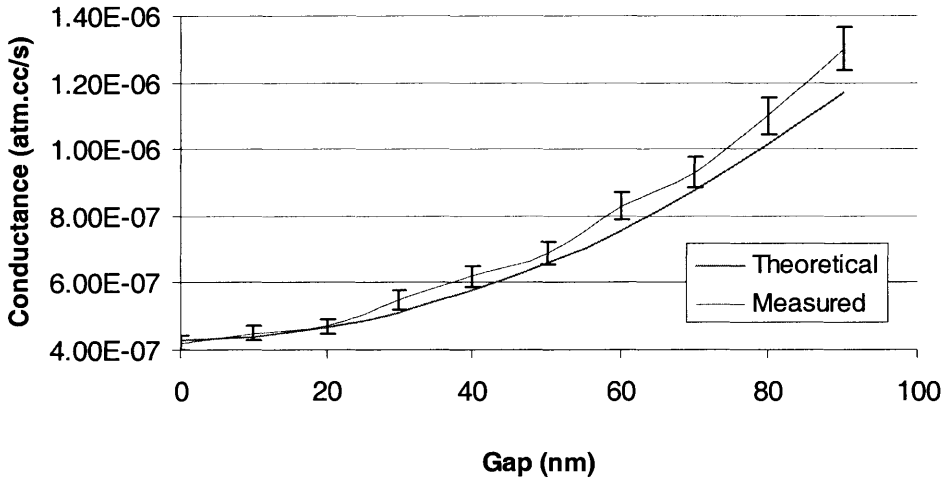

Figure 7.7 Results of Helium Flow Test (Theoretical curve corrected for observed baseline leak rate, 4.1 x 10^{-7} atm.cc/s).

minimum observed leak rate, for "zero" opening, was 4.1 x 10^{-7} atm·cc/s; this quantity is expected to be a function of the artifact under test. However, the baseline leak rate is also increased by gas leaks from the surrounding ambient air through the three metal Swagelok fittings used to connect between the outlet of the Nanogate and the Helium leak tester. After eliminating the baseline leak, the dependence of the flowrate on Nanogate displacement conforms very closely to the theory of molecular flow presented in Section 2.1. Fully open, the helium leak rate is greater than 1 x 10^{-3} atm·cc/s, which exceeds the upper-end of the measurement capability of the helium leak tester.

7.7 Liquid Leak Test

Leak tests with various liquids were also performed. Test liquids were deionized water and methanol. A syringe pump[1] was used to inject liquid into the inlet port of the Nanogate. The inlet line was connected to a pressurized manifold, thereby regulating the inlet pressure and preventing pressure surges or spikes. The outlet channel of the Nanogate was directly observed with an optical microscope, and flowrate information was inferred from the movement of the meniscus within the outlet microchannel, as discussed in Section 6.3. The entire setup is shown conceptually in Figure 7.8. The data for methanol is summarized in Figure 7.9, which shows no departure from the expected (theoretical) prediction for methanol for channel heights down to 150 nm. The flow conditions for methanol were room temperature (22 ^{o}C) and a pressure drop of 20 psi. Liquid flow tests were also performed for water for channel heights down to 80 nm, with a pressure drop of 40 psi, also at room temperature. These results are summarized in Figure 7.10. A final test was to evaluate the baseline leak rate of water through the Nanogate when it was entirely closed. Water at a pressure of 40 psi was applied to the inlet for 7 days, but no flow could be observed. Thus, the Nanogate is regarded as having excellent sealing properties for liquid flows, although more elaborate tests, possibly using a mass spectrometer to detect any small leakage of liquid, would be required to further substantiate this assertion.

1. Razel, Inc. Model A-99C

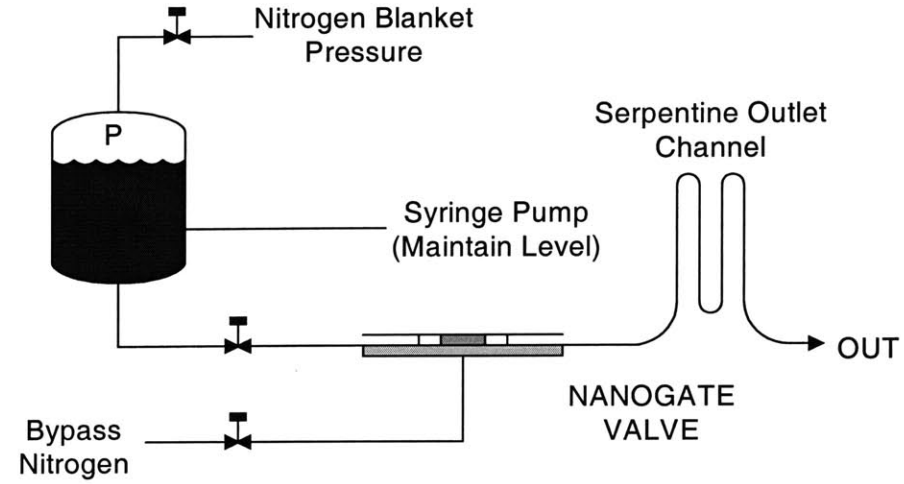

Figure 7.8 Schematic of Liquid Flow Apparatus

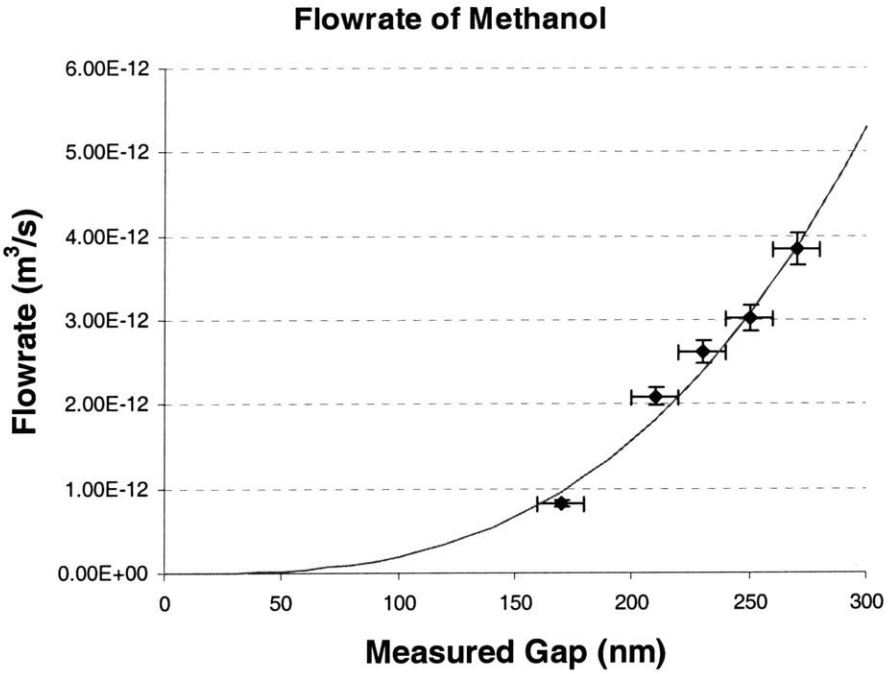

Figure 7.9 Flowrate of Methanol, 22 °C, pressure drop 20 psi.

7.8 Comparison to Existing Technologies

An honest comparison to competing technologies requires the examination of both MEMS-based valves as well as macroscopic, "conventional" proportional valves. The per-

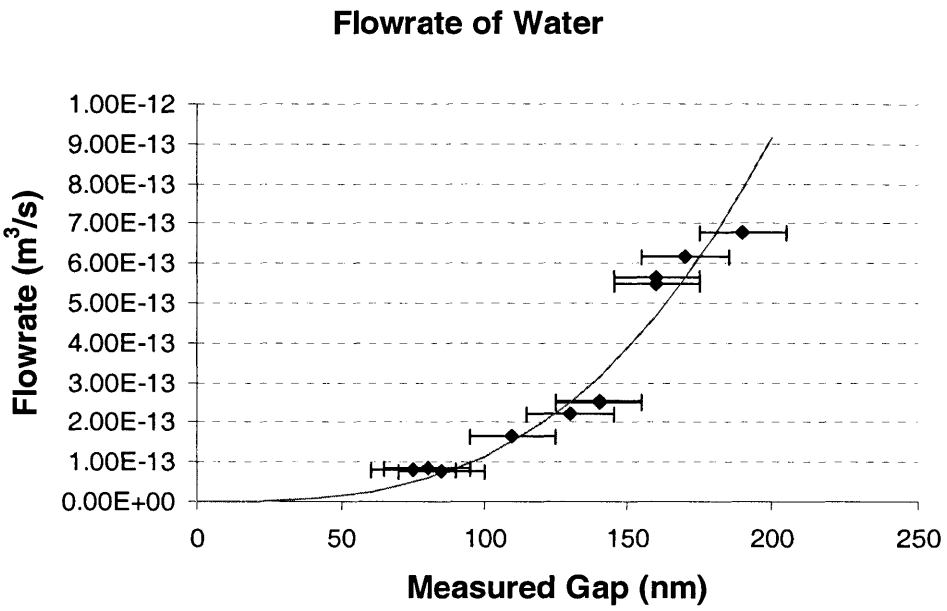

Figure 7.10 Flowrate of water, 22 °C, pressure drop 40 psi.

formance characteristics of the Nanogate that are of interested to end users are minimum leak rate, maximum flowrate, flowrate resolution, and size. To be useful, the comparison shown in Table 7.2 is made to valves which are presently available in the marketplace. It should also be noted when comparing the minimum leak rate that further developments in the packaging of the Nanogate are expected to significantly improve the off-state leak rate of the device by up to two orders of magnitude. This improvement would place the Nanogate among the highest precision mass-production vacuum valves in the world. It should also be emphasized that the ability to integrate multiple valves on a single die will increase the potential functionality far beyond any competing technology.

TABLE 7.2 Comparison of Nanogate to existing technologies

Parameter	Current Nanogate	Varian[a] Variable Leak Valve	Redwood Microsystems[b] MFC
Minimum Leak Rate (Helium at 1 bar into vacuum)	2.7 x 10^{-7} atm.cc/s	< 10^{-10} atm.cc/s	~ 10^{-7} atm.cc/s
Maximum Flowrate	> 10^{-3} atm.cc/s	> 10^{-3} atm.cc/s	0.017 to 33.3 atm.cc/s (depending on model)
Minimum Controllable Flowrate	10^{-9} atm.cc/s	10^{-10} atm.cc/s	10^{-3} atm.cc/s
Packaged Size	1.0" x 1.0" x 1.5" (not including control electronics)	4.5" x 4.5" x 2.5"	1.5" x 4.5" x 4.9" (with drive electronics)
Control Method	Electrical (Piezo-electric)	Manual	Electrical (Thermo-pneumatic)
Valve Position Feedback	Yes	No	No
Particle Free Operation	Yes	Yes	Yes
Multiple Valves per Package Possible?	Yes	No	Yes
"Hard" sealing materials (low Helium permeability)?	Yes (gold on Pyrex)	Yes (sapphire on metal)	No (elastomer seat)
Actuation Mechanism	MEMS fulcrum and diaphragm	Fine pitch screw thread / Lever	Thermo-pneumatic fluid
Sealing Mechanism	Conformal gold and Pyrex surfaces	Metal gasket against optically flat sapphire	Silicon boss against elastomer seat

a. Varian Inc, Lexington MA

b. Redwood Microsystems, Menlo Park CA

Chapter 8

FUTURE WORK

The basic principle and operation of the Nanogate has led to the creation of a platform technology that has been conclusively demonstrated. Two-angstrom control of the plate separation, control of liquid flows, control of helium flowrates within 10^{-9} atm.cc/s and near-perfect mating of the "hard" (non-elastomeric) valve boss and valve land plates have been shown. It is now appropriate to envision applications of the Nanogate which rely on the extremely fine flow and position control that is possible with this device. It is also worthwhile to envision greater levels of integration and more robust packaging which will allow the Nanogate to be used in a broad range of applications. Future work, described herein, will focus on integrating the actuation and metrology functions which will improve the ease-of-use and robustness of the device. Additional development will concentrate on demonstrating the separation and filtering capabilities of the Nanogate.

8.1 Integrated Actuation

Two actuation methods have been proposed for a fully-integrated Nanogate device: piezo-electric and electrostatic. A piezoelectric actuator could comprise either a piezoelectric stack, or a bonded piezoelectric bimorph are used to apply deflections directly to the top diaphragm. These would be especially useful in cases where high actuation forces are required -- for example in controlling liquid flows where forces due to surface tension in a narrow slit have been observed to cause pull-in. A piezoelectric stack, as in Figure 8.1,

would require a precisely machined package in order to accurately locate the piezo actuator against the Nanogate diaphragm. This would represent an increased cost. The actuation voltages required for a piezoelectric stack depend entirely on the stack that is specified, although low voltage piezoelectric stacks can be purchased with actuation voltages in the range of 100 to 150 V.

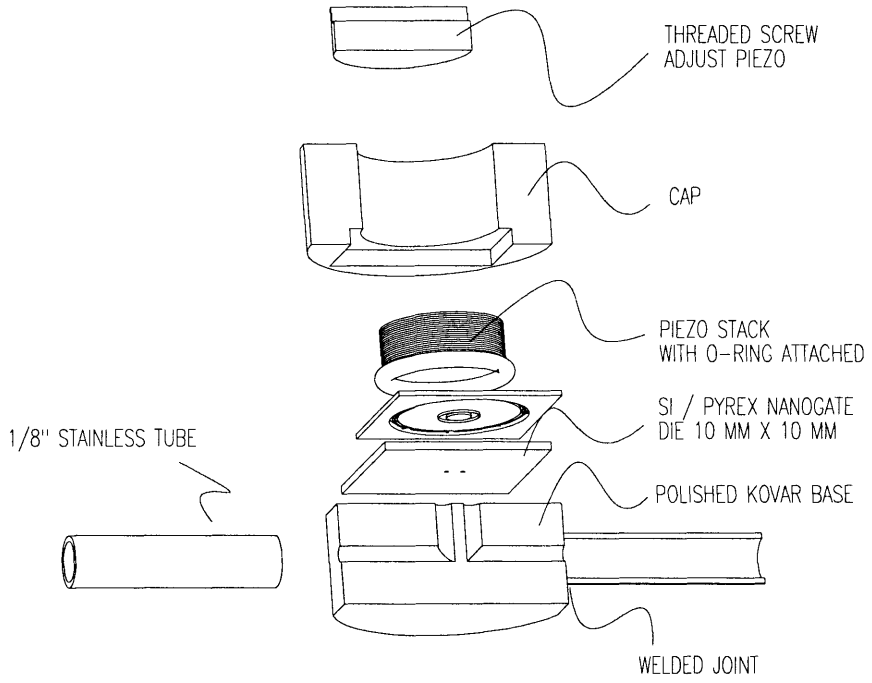

Figure 8.1 Concept for integrated Nanogate, 1/2" x 1/2" (Drive electronics not shown).

A more technically challenging approach, that represents a higher level of integration, would involve bonding a piezoelectric disk directly to the top diaphragm of the Nanogate. The topside of this disk would be silvered, and wirebonded from its center to a terminal on the package, and the top of the Nanogate diaphragm, also conductive, would likewise be connected to a ground terminal. This would then form a piezoelectric bimorph actuator with one active and one elastic layer. The actuation voltages required for an assembly of this type would also be on the order of 100 - 150 V, depending on the thickness of the piezoelectric layer.

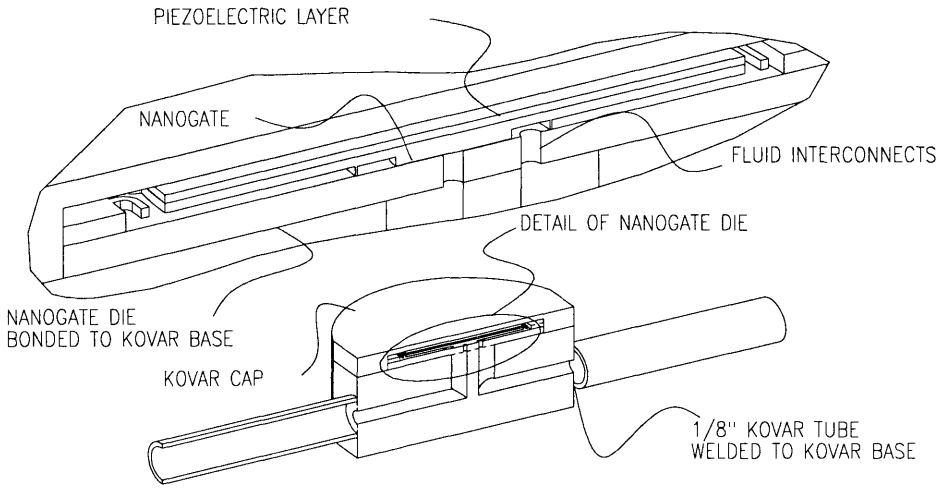

Figure 8.2 Packaged Nanogate with bonded piezoelectric disk actuator.

One important aspect of either of these solutions is that a separate, stable, high-voltage power supply would also be required to obtain fine actuation and control. This would, naturally, add substantial size to the device, and motivates the search for a more easily integrated actuator.

Electrostatic actuators are typically characterized as having either a short stroke and high force, or a long stroke but very weak forces. However, a class of electrostatic actuators which exploit the 'pull-in' effect can obtain both high forces and long strokes. These "zipper" actuators have been successfully demonstrated by [Branebjerg, 1992]. This type of actuator is comprises two parallel plates, where one (or both) plates are compliant, conductive and one (or both) plates are coated with a dielectric film, as in Figure 8.3. The mode of operation involves increasing the voltage between these two plates to the point at which the pull-in instability is reached (i.e. the rate of change of electrostatic force exceeds the linear spring constant), and the plates pull together. Further increasing the voltage beyond this pull-in voltage causes the compliant plates to bend and enlarges the region of the actuator which has been pulled together, as in Figure 8.4. The high forces necessary to continue the 'zipping' behaviour are due to the large electric fields in the immediate vicinity of the line of contact between electrode and ground. However, due to the several order-of-magnitude smaller forces exerted by electrostatic actuators, when

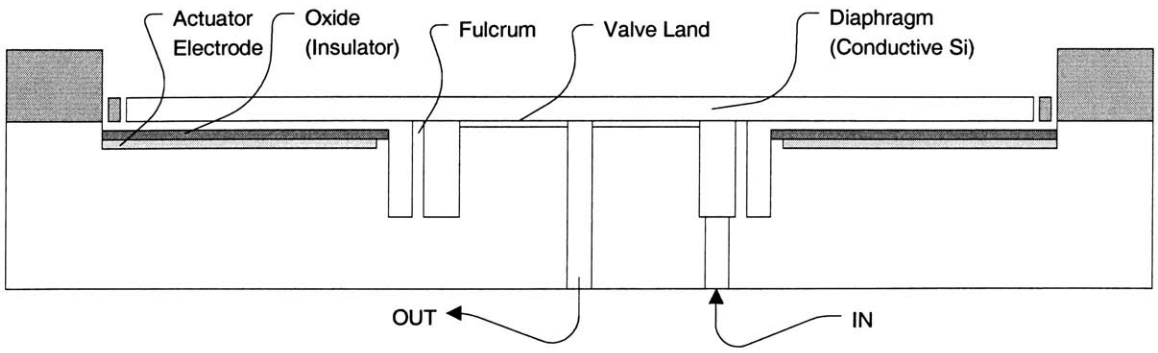

Figure 8.3 Electrostatically actuated gas flow control valve, undeflected.

compared to piezoelectrics, electrostatics are not indicated for use in applications where substantial pressures or stiction forces may be present.

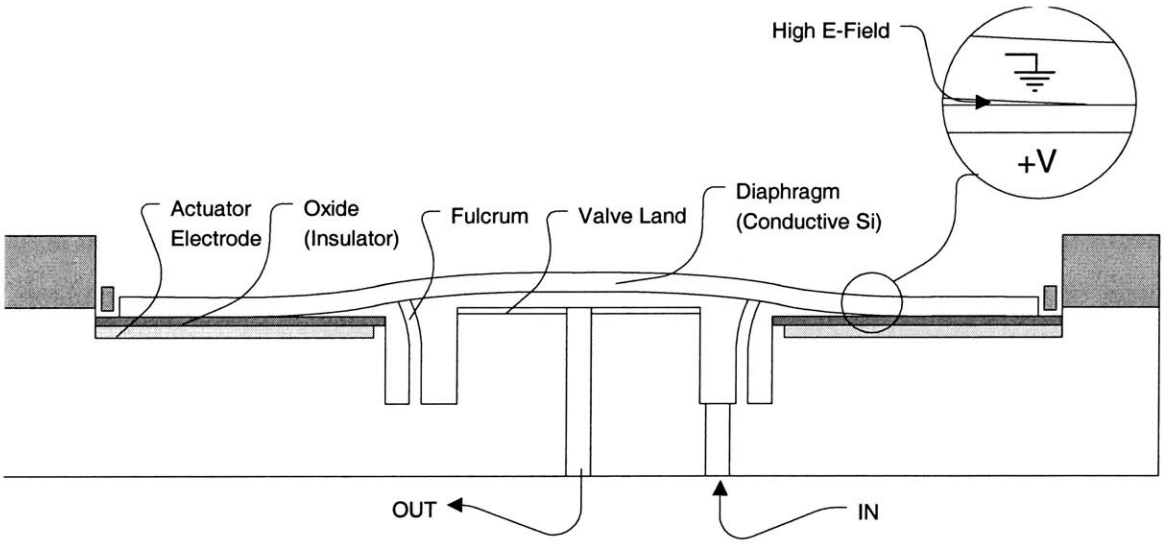

Figure 8.4 Electrostatically actuated gas flow control valve, deflected.

8.2 Integrated Metrology

Present implementations of the Nanogate have successfully demonstrated the utility of external optical metrology. However, this solution cannot be applied to any integrated device since it is much too large and would represent an excessive challenge to miniaturize. In addition, the long deadpath of the current interferometer causes large amounts of

measurement noise, typically on the order of 10 nm during actual use although this can be reduced in special cases. Two other approaches that have been investigated to replace interferometry: capacitance sensing and diffraction-based optical displacement sensors.

A diffraction optical displacement sensor, as demonstrated by N. Loh et al uses the relative deflection of two interdigitated optical diffraction gratings to sense displacement as shown in Figure 8.5 [Loh, 2002]. This design represents a small departure from the design of N. Loh but operates in an identical fashion. The performance of this optical technique is a significant improvement over interferometry in that the reference plane of the measurement is very close to the measurement target, and therefore the effect of thermal noise on the optical signal is minimized. Thermal noise would still, of course, affect the photodiode used for measurement but this can be minimized electronically. The electronics required to power the laser diode, chopper, and condition the signal output from the photodiode are, of course, extensive, and miniaturization would not be an insignificant challenge.

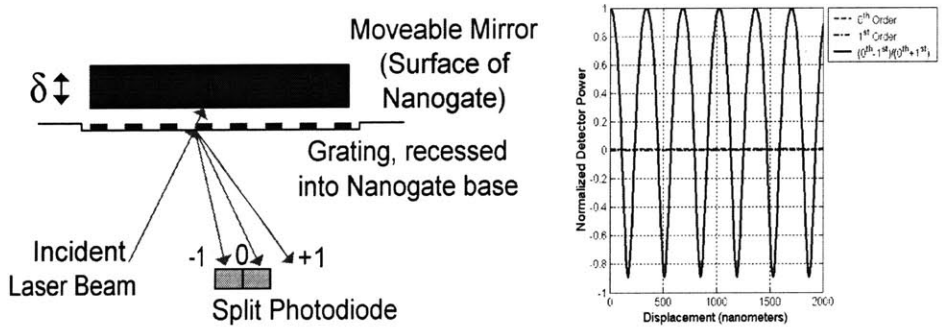

Figure 8.5 Diffraction-based optical sensor

The Nanogate is very naturally suited to capacitive measurement of the gap, given its symmetric geometry and linear force-displacement characteristics. Furthermore, capacitance can be easily measured using conventional electronics, and devices based on capacitive measurement have frequently been demonstrated; this is the basis a very large number of MEMS sensors. Thus capacitance measurement represents a very low-risk approach to

integrating metrology into the Nanogate, with widely known techniques for integration and miniaturization of the sensing circuitry.

8.3 Sorting and separations

Gas flow in the Nanogate is governed by the Boltzmann equations as described in Section 2.1. The flowrate of a gas molecule is dependent on its molecular weight, the temperature and the height of the gap squared. Thus, for a given inlet gas composition, the outlet gas composition will be governed by:

$$Q_n = C_n \Delta P \tag{8.1}$$

Where C_n is the conductance of each species n, and ΔP is the pressure drop across the gap. The conductance is given by:

$$C_n = \frac{1}{\sqrt{\rho_1} W}, \tag{8.2}$$

where ρ_1 is proportional to the molecular mass as in Equation 2.6. The difference in gas flow rates must be accounted for when a mixture of gases is flowing continuously through the Nanogate. However, this effect could also be used for separation, allowing the Nanogate to perform the function of a separation column in a gas chromatograph. As an example, consider a sample composed of benzene (M.W. 78.1 g/mol) and toluene (M.W. 92.1 g/mol), with a volume of 2.5 pL, injected into the Nanogate gap, as in Figure 8.6. As the gases flow through the Nanogate, the sample will become separated due to the different conductance of each gas. The minimum column length for separation, calculated in Appendix C, is approximately 500 microns, at which point the analytes are separated by 20 microns ("separation" distance is calculated as $\xi_2 - \xi_1$), and therefore could be distinguished from each other by a detector. The residence time of the sample in the Nanogate is much less than a millisecond, indicating that the separation event is also extremely fast. This also raises the possibility of conducting repeated, high speed measurements. The true gas concentration distribution in the Nanogate would, of course, be better modeled by a

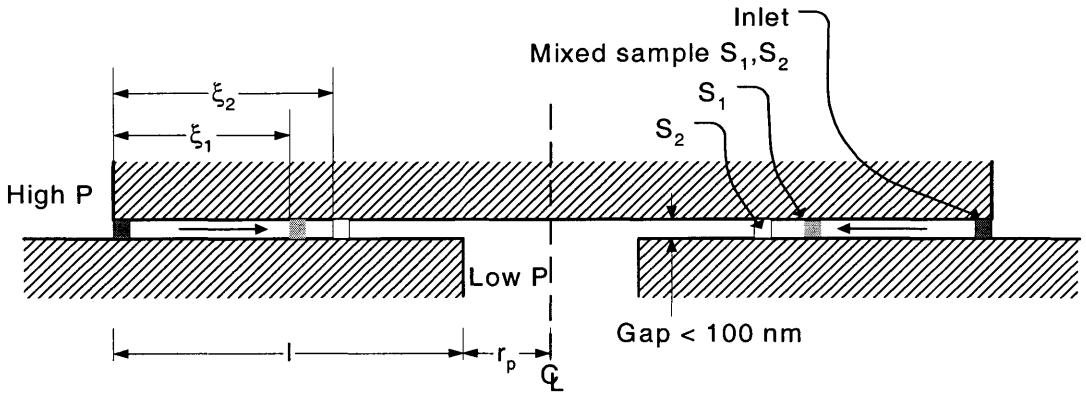

Figure 8.6 Diagram of inlet of mixed sample comprised of analytes S_1 and S_2, and subsequent separation.

Monte Carlo simulation, so that any interdiffusion effects, and the effect of the surrounding carrier gas, could be more rigorously evaluated.

The physics governing the flow of liquids in the Nanogate, and in particular suspensions of large molecules, for example proteins or DNA, are substantially different than gas flows. The adsorption properties of the wall will determine, to a large extent, the mobility of a protein in the Nanogate gap. Clearly, adsorption will occur. However, there will be a finite quantity of protein that adsorbs to the channel surfaces, at which point the surfaces will reach saturation. After saturation, some molecules will migrate through the gap and into the outlet channel, where they can be analyzed by a mass spectrometer, for example. Thus, the mobility of proteins in the Nanogate will be affected by not only the geometric parameters, but also the condition and 'history' of the walls. Coatings such as PEG, thiol- or silane-based monolayers, and other wall coatings will be applied to counter some of the adsorption effects, however it is not likely that any one coating will be found that will counter nonspecific adsorption in all cases. For specific molecules, e.g. DNA, and for certain pH ranges, buffer concentrations etc., it may be possible to counter adsorption entirely, but these flow conditions remain the subject of future study.

Last, the effluent from a Nanogate liquid chromatography column could be readily interfaced into a mass spectrometer, using a range of well-known ionization techniques, such

as electrospray ionization or atmospheric pressure chemical ionization. Mass spectrometry is already well established for the analysis of proteins, polymers and, in fact, a huge range of molecules. Modern mass spectrometers can sense femto-mole concentrations of molecules [Rossi, 2002], and are ideally suited to handling the very small quantities of analyte that would flow from the Nanogate. Thus, the Nanogate would provide yet another means of sorting and separation, which when interfaced to a mass spectrometer, would create a new and versatile scientific instrument for protein analysis and drug discovery.

Chapter 9

CONCLUSIONS

The design, development and characterization of the Nanogate have been presented in detail. Two-angstrom control over the slit aperture (gap opening) and extremely fine control of gas and liquid flows have been conclusively demonstrated. Furthermore, the validity of the no-slip boundary condition and the Navier-Stokes equations have been confirmed for water and methanol flowing past glass and gold surfaces separated by only 80 nm. Rarefied gas theory has been confirmed to describe atmospheric pressure gas flows in nanometer-scale channels. The minimum measured gas flowrate, for Helium at a pressure drop of 6.35 psi into vacuum, was 4.1×10^{-7} atm.cc/s, which represented an improvement by a factor of almost 10^4 over comparable MEMS proportional valves[1], and was similar to commercially available MEMS shutoff valves [Henning, 1997]. Furthermore, no MEMS devices have been reported with the exceptionally fine control of gas flowrates (on the order of 1×10^{-9} atm.cc/s) that has been demonstrated with the Nanogate, although large-scale valves manufactured by Varian, Inc.[2] have comparable resolution. The smallest measured flowrate of water was 0.1 nL/s, at a 40 psi drop, and the smallest measured flowrate of methanol was 1 nL/s, for a 20 psi drop. It should be noted that the values for liquid flow do not represent the smallest controllable liquid flowrates but rather the practical limitations of the flow measurement technique. A leak test for water at 40 psi indicated

1. Redwood Microsystems, Menlo Park CA
2. Varian, Inc., Lexington MA

no measurable leakage over a period of seven days. The sealing and flow control properties of the Nanogate were therefore excellent.

A simplified MEMS-based manufacturing process, capable of creating mass-produced Nanogates has been successfully demonstrated. The process creates bonded, hermetically sealed valve and microchannel systems. Additionally, plastic deformations of the valve seats during fabrication ensure a near-perfect seal in operation.

In future work, higher levels of integration, more sophisticated actuators and further miniaturization can all be envisioned. More robust packaging techniques must also be investigated. Applications of the Nanogate in ultra-fine flow control, high complexity microfluidic systems, and manifolds, can all be envisioned as a direct application of this work. Further applications in gas chromatography and liquid separations are also indicated by theory but not yet demonstrated experimentally. More broadly, the Nanogate can be regarded as a basic scientific instrument for extensive new research on the properties of highly confined, molecular-scale liquid systems.

REFERENCES

[Timoshenko, 1940] Timoshenko, S., *Theory of Plates and Shells*, McGraw-Hill, New York, 1940.

[Demirel, 2001] Demirel, A. L. and Granick, S., *Origins of solidification when a simple molecular fluid is confined between two plates*, J. Chem. Phys., v. 115 n. 3, p. 1498-1512.

[Chen, 1985] Chen, D.Y.C. and Horn, R.G., *The drainage of thin liquid films between solid surfaces*, J. Chem. Phys., 83 (10), 15 Nov. 1985, p. 5311-5323.

[Zhu, 2001] Zhu, Y. and Granick, S. *Rate Dependant Slip of Newtonian Liquid at Smooth Surfaces*, PRL v. 87 no. 9, 27 Aug. 2001.

[Zhu, 2002] Zhu, Y. and Granick, S. *Limits of the Hydrodynamic No-slip Boundary Condition,* PRL v.88 no. 10, 11 Mar. 2002.

[Loeb, 1934] Loeb, L.B., *The Kinetic Theory of Gases*, Dover Publications, New York, 1961.

[Arkilic, 1997] Arkilic, E.B., *Measurement of the Mass Flow and Tangential Momentum Accomodation Coefficient in Silicon Micromachined Channels*, MIT Ph.D Thesis, 1997.

[Quake, 1998] Quake, S. et. al., *Disposable Microdevices for DNA Analysis and Cell Sorting*, Proc. Solid State Sensor and Actuators, Hilton Head SC, June 8-11, 1998.

[Ehrlich, 1992] Ehrlich, C. D. and Basford, J. A., *Recommended practices for the calibration and use of leaks*, J. Vac. Sci. Tech. A 10(1), Jan/Feb 1992.

[Roark, 1943] Roark, R.J., *Formulas for Stress and Strain*, McGraw-Hill, New York, 1943.

[Lindsay, 2000] Lindsay, S., *Scanning Tunneling Microscopy and Related Techniques*, ed. D. Bonnell, John Wiley, 2000.

[Heuberger, 1998] Heuberger, M. et. al., J. Phys. Chem. B, 102, 1998, 5038-41.

[Senturia, 2001] Senturia, S. D., *Microsystem Design*, Kluwer Academic Publishers, Boston, 2001.

[Ayon, 1998] Ayon, A.A. and Mirza, A.R., *Silicon Wafer Bonding: Key to MEMS High-*

Volume Manufacturing, Sensors Magazine, Dec. 1998.

[Roberts, 2002] Roberts, D.C., *Design, modeling, fabrication and testing of a piezoelectric microvalve for high pressure, high frequency hydraulic applications*, MIT Ph.D Thesis, 2002.

[Duffy, 1998] Duffy, D.C. et al, *Rapid Prototyping of Microfluidic Systems in PDMS*, Anal. Chem., 70 (23), 4974-4984.

[Branebjerg, 1992] Branebjerg, J. and Gravesen, P., *A New Electrostatic Actuator Providing Improved Stroke Length and Force*, MEMS '92, Travemunde, DE, Feb. 4-7 1992, 6-11.

[Rossi, 2002] Mass Spectrometry in Drug Discovery, D.T. Rossi and M. W. Sinz eds., Marcel Dekker: New York, 2002.

[Slocum, 1999] US Patent #5,964,242: *Method of and apparatus for substance processing with small opening gates actuated and controlled by large displacement members having fine surface finishing*, Oct. 12 1999.

[Loh, 2002] N.C. Loh, M.A. Schmidt, and S.R. Manalis, *Sub-10 cm3 interferometric accelerometer with nano-g resolution*, IEEE Journal of Microelectromechanical Systems, 11 182 (2002).

[Dubois, 2001] Dubois, P.H. et al, *Electrostatically actuated gas microvalve based on a Ta-Si-N membrane*, Proceedings of MEMS'2001, pp.535-538, 2001.

[Henning, 1997] A. K. Henning, J. Fitch, E. Falsken, D. Hopkins, L. Lilly, R. Faeth, and M. Zdeblick, *A thermopneumatically actuated microvalve for liquid expansion and proportional control.* In Proceedings, TRANSDUCERS '97: 1997 International Solid State Sensors and Actuators Conference, pp. 825-828.

[Maillefer, 1999] D. Maillefer et al., *A High Performance Silicon Micropump for an Implantable Drug Delivery System*, Technical Digest MEMS'99, p.541, Orlando, FL, January 1999.

[Harrison, 1993] D.J. Harrison, K. Fluri, K. Seiler, Z. Fan, C.S. Effenhauser and A. Manz, *Micromachining a Miniaturized Capillary Electrophoresis-Based Chemical Analysis System on a Chip*, Science, 1993, 261, 895-897

Appendix A

PDMS PROCESS FLOW

The standard process for casting PDMS parts in soft lithography processes is given below, courtesy of Hang Lu, MIT.

1. Place the mold and a drop of silanizing agent into a vacuum chamber. The silanizing agent prevents the PDMS from sticking to the mold.

2. Mix Prepolymer and Initiator (10:1)

3. Degas mixture in vacuum for 20 minutes

4. Pour the PDMS mixture onto the mold substrate.

5. Cure the PDMS at 65^{o}C for 2 hours.

6. Carefully peel PDMS from wafer when ready to bond to the substrate wafer.

7. Clean PDMS and glass surfaces (methanol, or tape for the PDMS).

8. Plasma ash PDMS and glass substrates for ~10s. Excessive ashing of the PDMS will (irreversibly) prevent bonding.

9. Press surfaces together. You should be able to observe the bond front propagating.

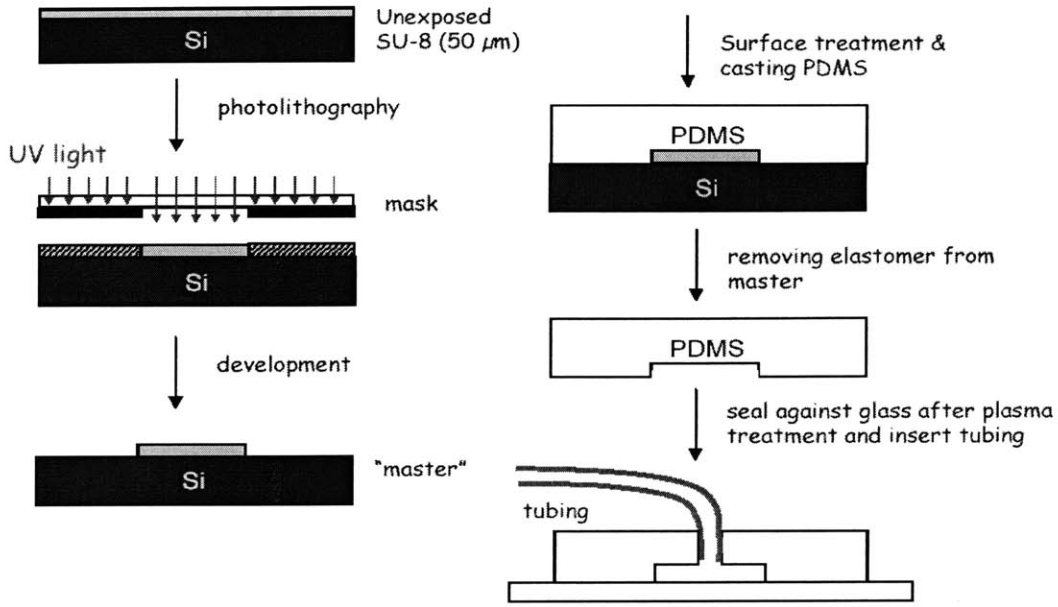

Figure A.1 Generic process flow for creating an SU-8 master, replicated with PDMS

Appendix B

DIE LAYOUTS AND MASKS

The layout of individual dies is shown here in Figure B.1 to Figure B.3. The entire mask

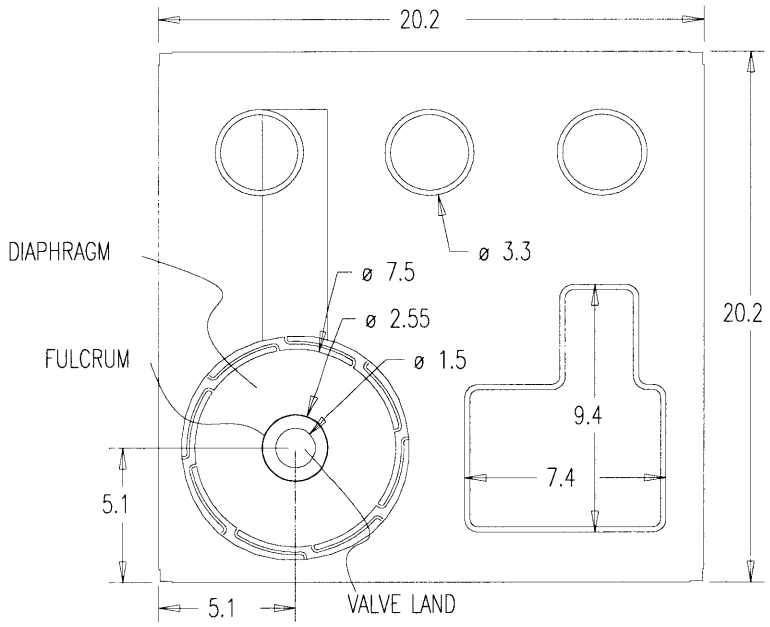

Figure B.1 Nanogate die layout. All dimensions mm.

layouts, and manufacturing drawings for the Pyrex wafers are shown in Figure B.4 to Figure B.8.

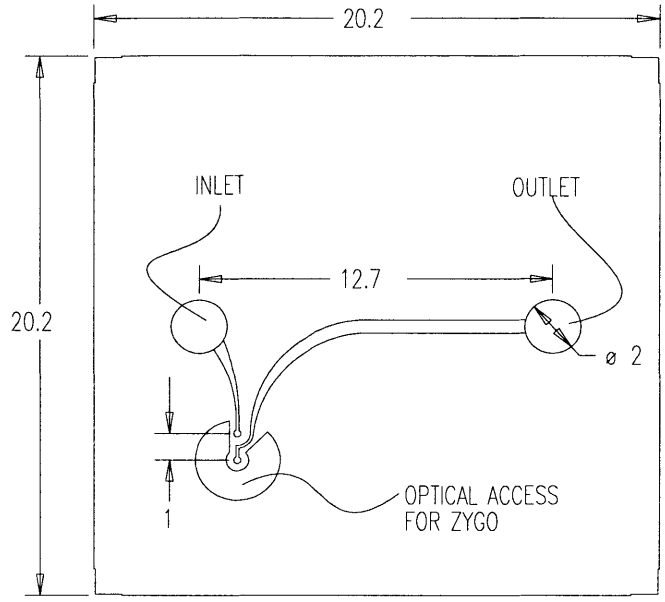

Figure B.2 Two-port Nanogate base die (for gas flow tests). All dimensions mm.

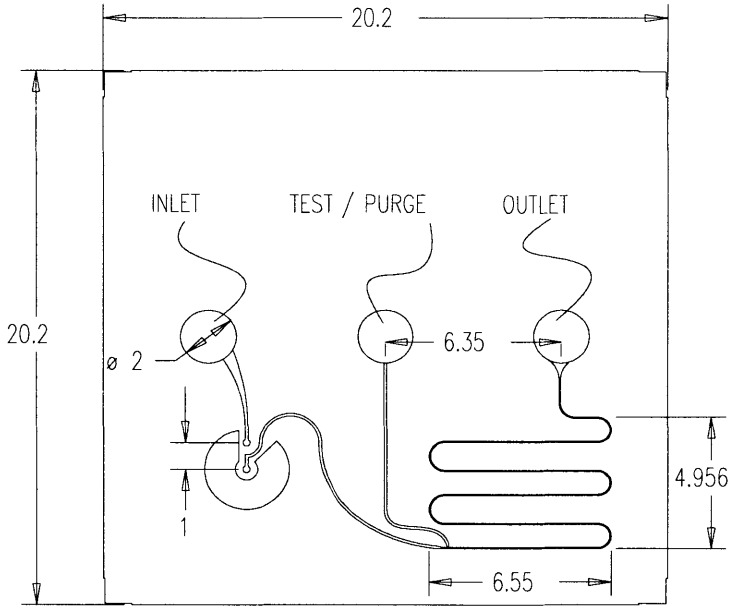

Figure B.3 Three-port Nanogate base die with serpentine outlet microchannel. All dimensions mm.

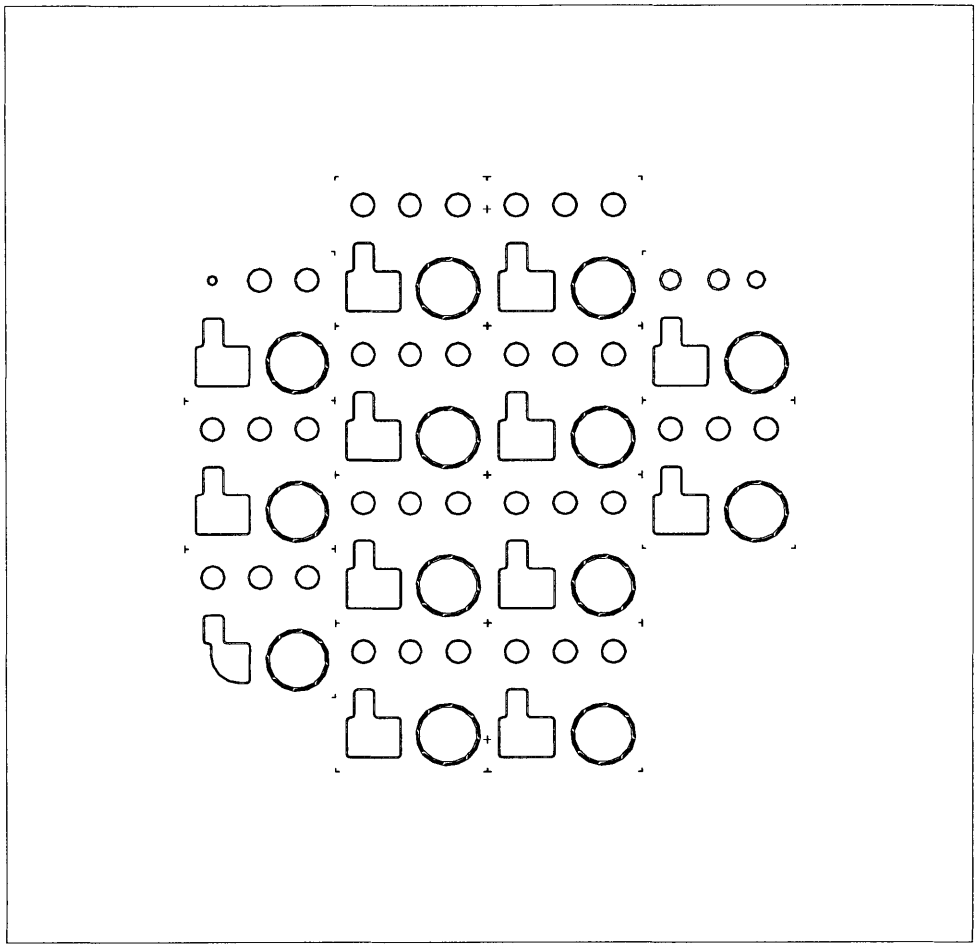

Figure B.4 Nanogate frontside mask (0.5 micron resolution, chrome on soda lime glass). Final detailing by H. Ma

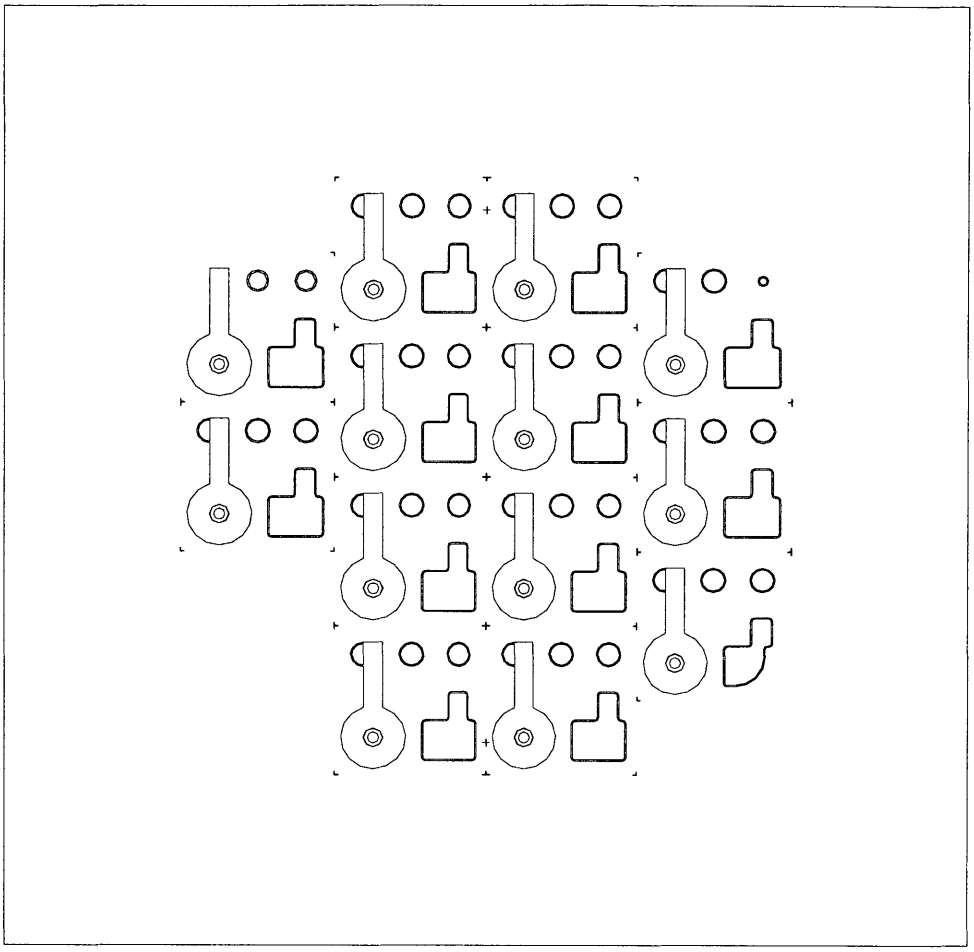

Figure B.5 Nanogate bottomside mask (0.5 micron resolution, chrome on soda lime glass). Final detailing by H. Ma

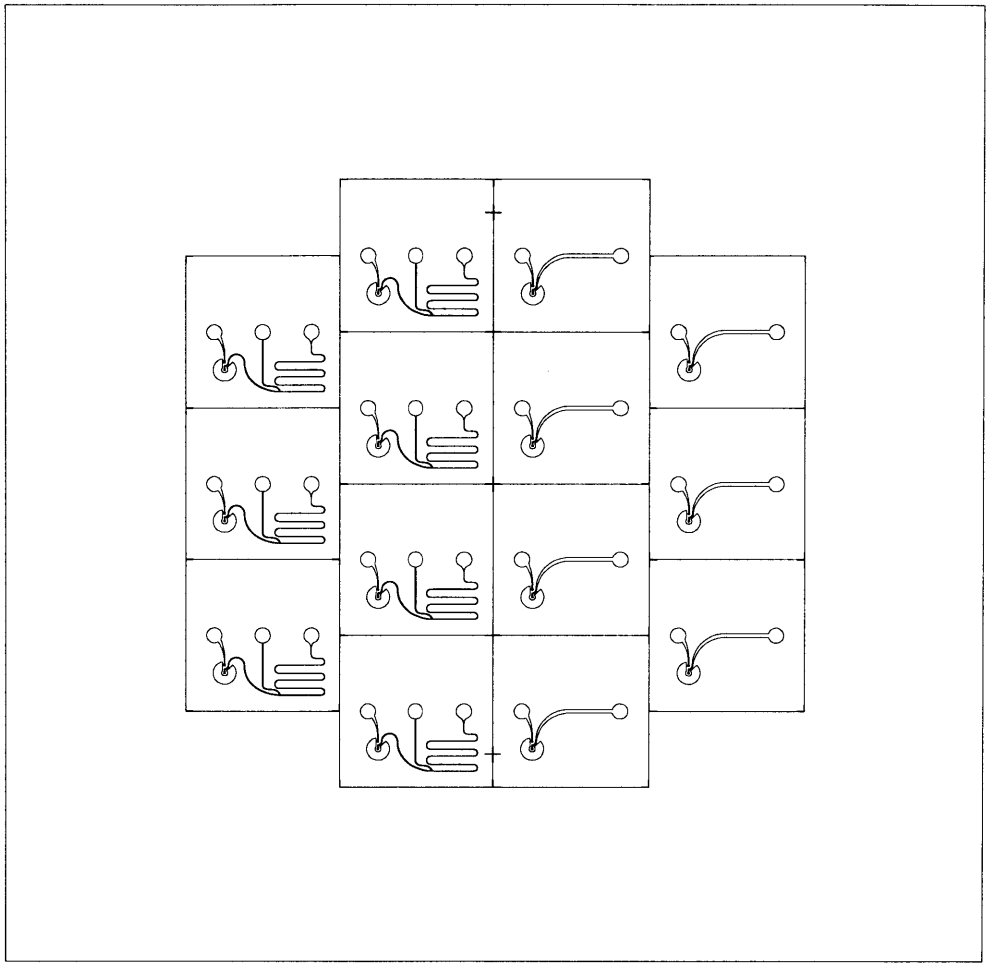

Figure B.6 Nanogate microchannel mask, frontside (transparency mask, 25 micron resolution, transferred to chrome on soda-lime glass).

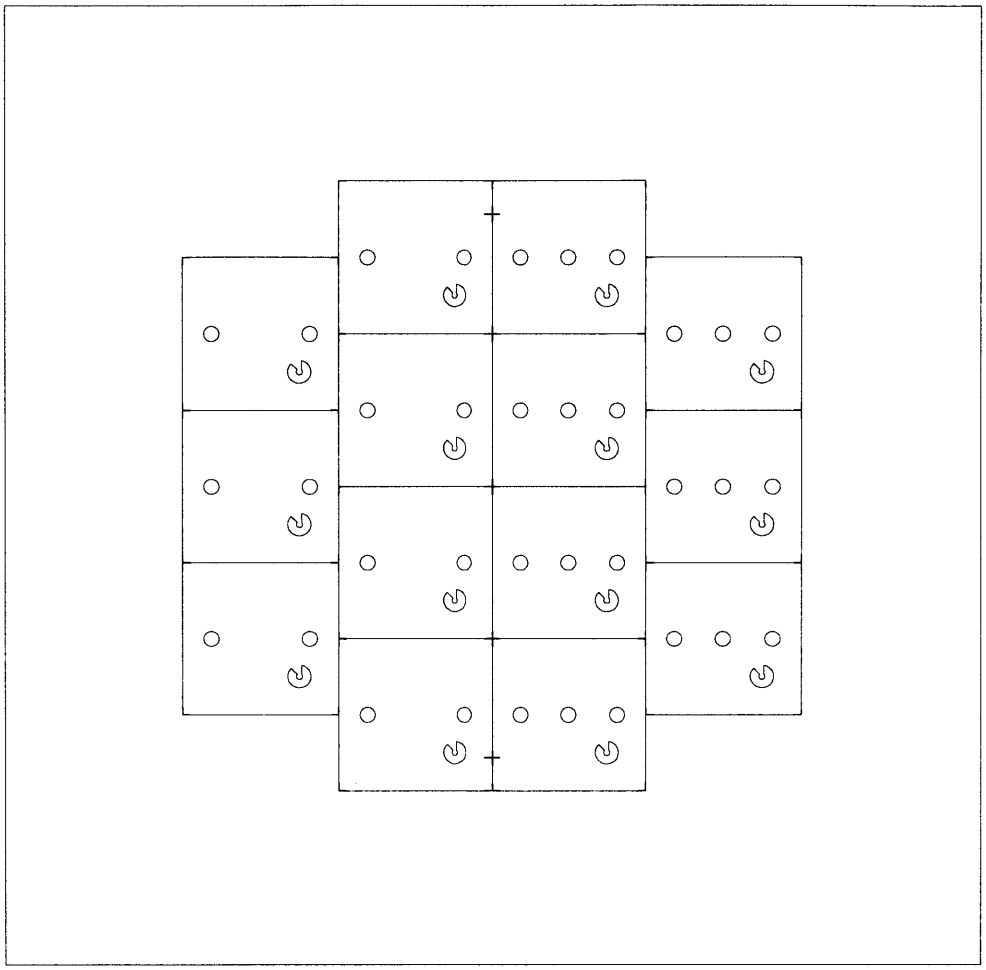

Figure B.7 Nanogate microchannel mask, backside (transparency mask, 25 micron resolution, transferred to chrome on soda-lime glass).

Figure B.8 Manufacturing drawing for Pyrex glass wafer (attached).

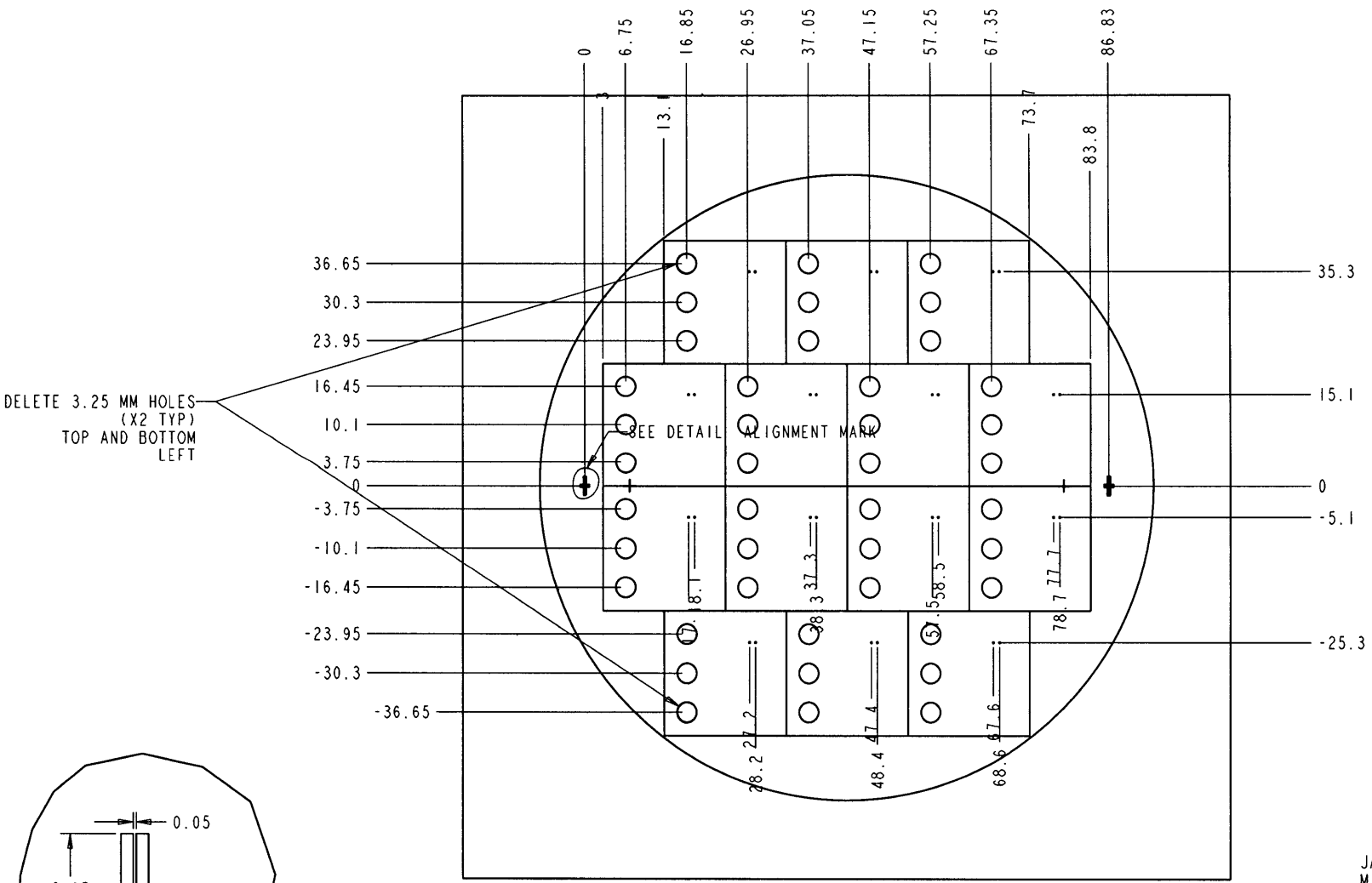

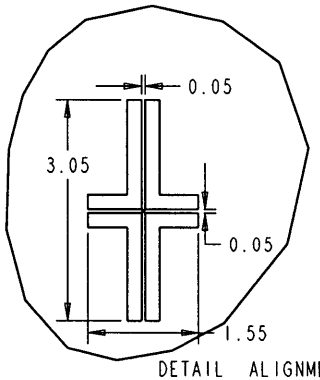

DETAIL ALIGNMENT MARK
SCALE 20.000

SCALE 2.000

JAMES WHITE
MIT RM. 3-438A
617-258-0726
1/3/02
NANOGATE_PYREX_BULLEN
ALL DIMENSIONS MM

Appendix C

SEPARATION CALCULATIONS

A graph of the separation distance between analytes as a function of time.

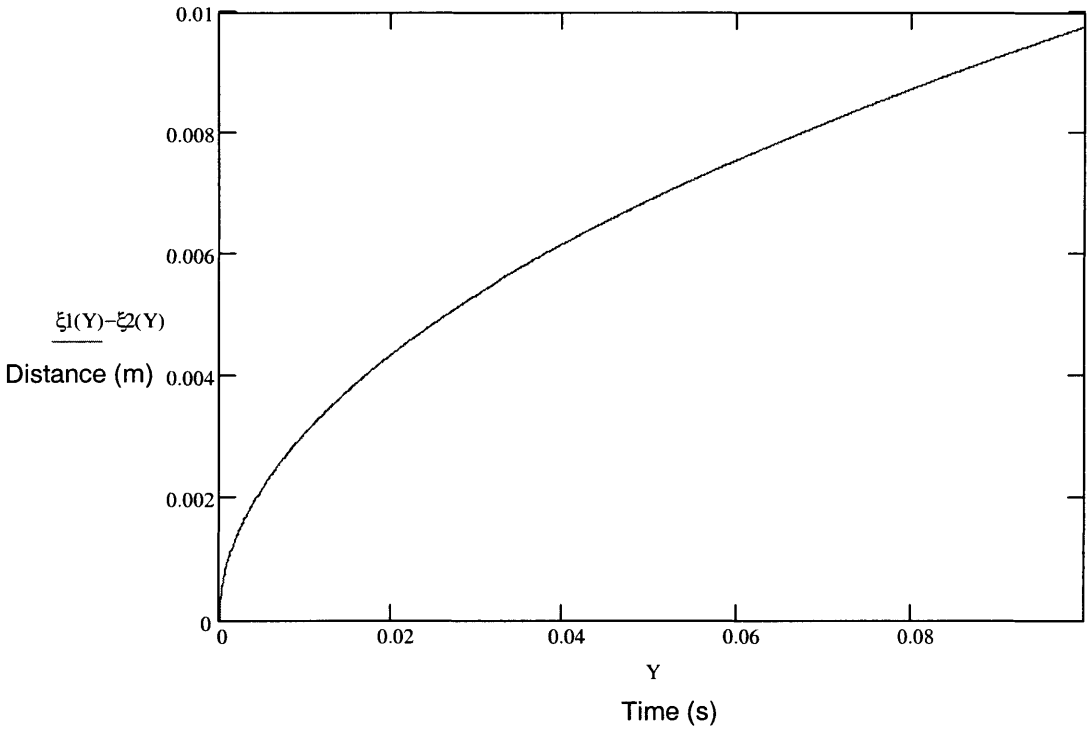

Calculation of conductance
for a given M.W.

$$\rho 1(M) := \frac{M}{8.314 \cdot 287}$$ Specific density for each gas

$r2 := 625 \cdot 10^{-6}$ $b := 125 \cdot 10^{-6}$ Dimensions of the Nanogate

$r1 := 125 \cdot 10^{-6}$ $s := 20 \cdot 10^{-6}$ Minimum separation of samples.

$$W(h) := \frac{8 \cdot \sqrt{2 \cdot \pi} \cdot h^2}{3 \cdot \ln\left(\frac{r2}{r1}\right)}$$ Form factor for the toroidal Nanogate geometry.

$$C(M,h) := \frac{W(h) \cdot 1000000}{\sqrt{\rho 1(M)}} \text{ in cc/s}$$ Conductance

$$\xi(Q,t,h) := \sqrt{\frac{Q \cdot t}{\pi \cdot h} + b^2}$$ Position of each analyte as a function of time.

$$\xi 1(\tau) := \xi\left(C\left(78.1, 80 \cdot 10^{-9}\right), \tau, 80 \cdot 10^{-9}\right)$$

$$\xi 2(\tau) := \xi\left(C\left(92.1, 80 \cdot 10^{-9}\right), \tau, 80 \cdot 10^{-9}\right)$$

$\upsilon := .00001$

$T := \text{root}(\xi 1(\upsilon) - \xi 2(\upsilon) - s, \upsilon)$

$T = 4.453 \times 10^{-7}$ s Minimum residence time in the gap.

$\xi 1(T) = 5.253 \times 10^{-4}$ Distance that analyte #1 (Benzene) travels in that tim

$\xi 2(T) = 5.053 \times 10^{-4}$ Distance that analyte #2 (Toluene) travels in that time

Minimum aspect ratio of channels:

$$A := \frac{\xi 1(T)}{80 \cdot 10^{-9}}$$

$A = 6.566 \times 10^{3}$

$2500 \cdot 10^{-18} = 2.5 \times 10^{-15}$ m3
inj. vol

Appendix D

MANUFACTURING DRAWINGS

Manufacturing drawings detailing the test bed, Kovar packaging, and pyrex packaging are attached.

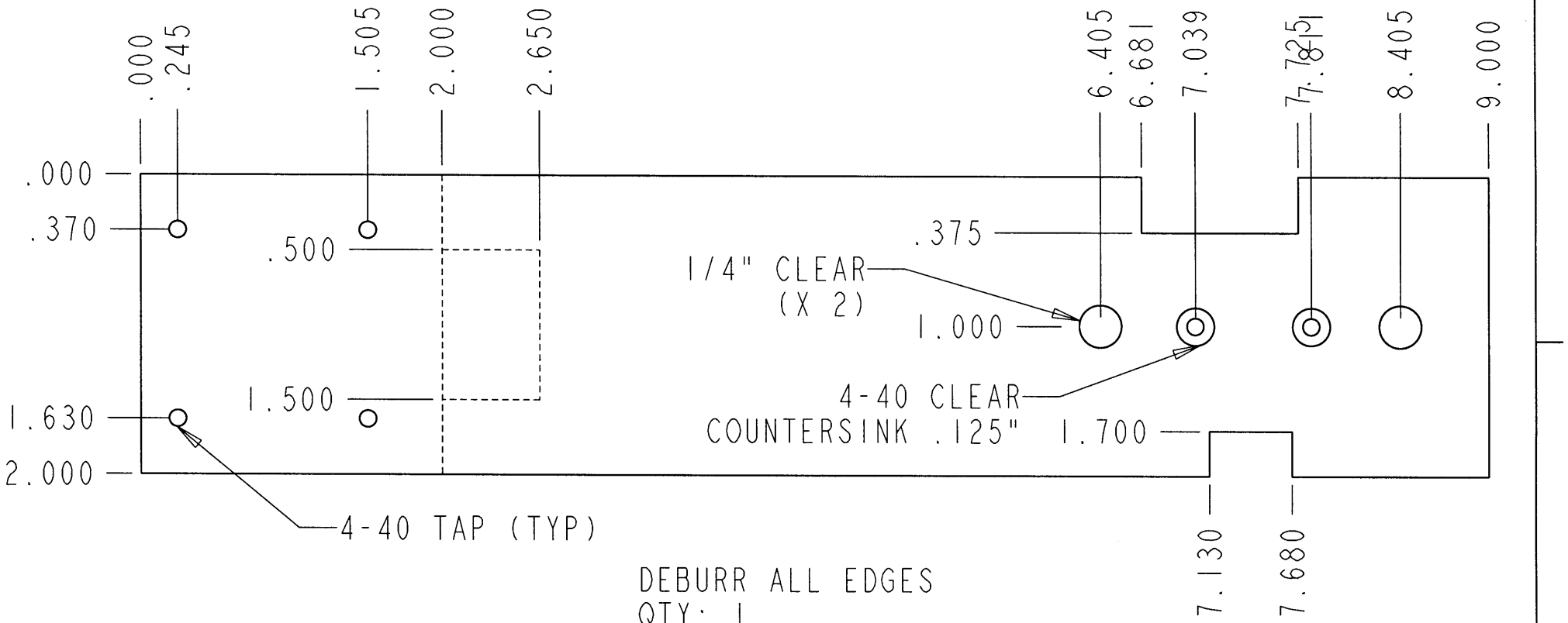

DEBURR ALL EDGES
QTY: 1

ZYGO BASE SUPER INVAR 5/2/02 JAMES WHITE	P E R G MIT RM. 3-438A 617-258-0726

SCALE 1.000

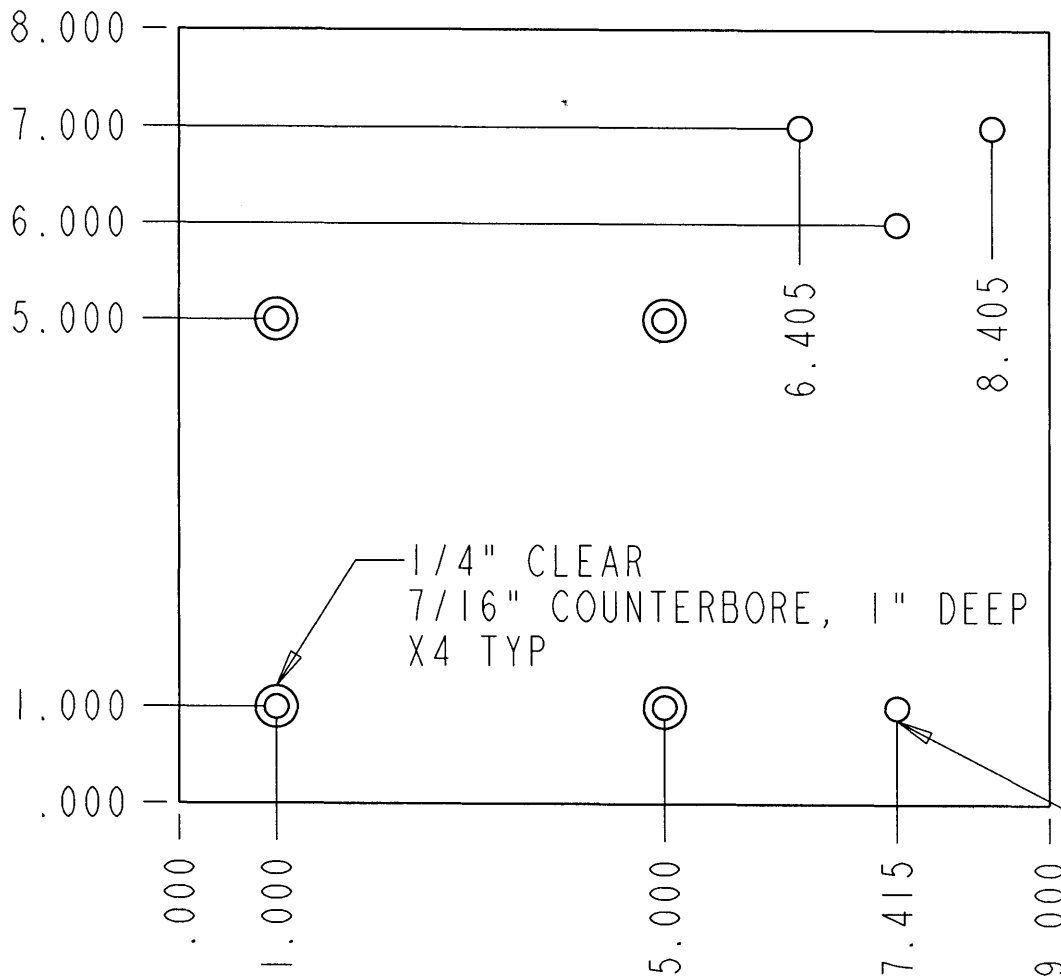

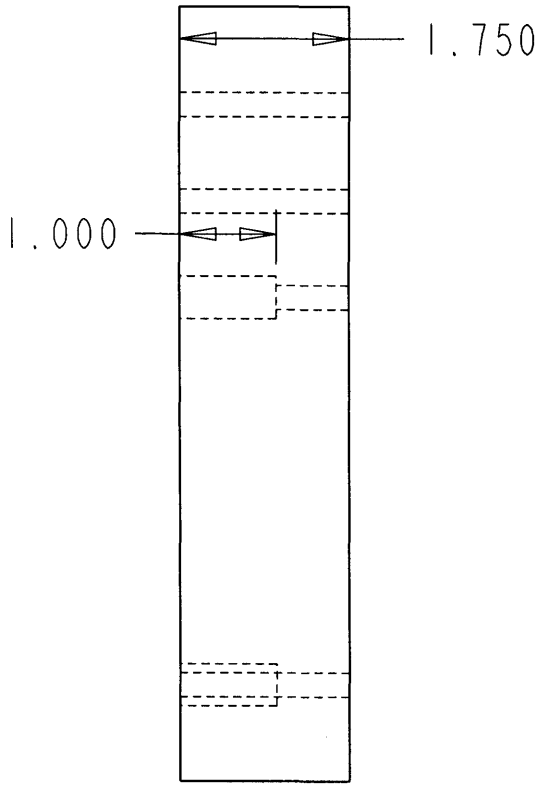

JAMES WHITE
MOUNTING BLOCK
ALL DIMENSIONS IN.

MIT RM. 3-438A
77 MASSACHUSETTS AVE.
CAMBRIDGE, MA 02139
617-258-0726

MATERIAL: ALUMINUM

QTY: 1

SCALE 0.500

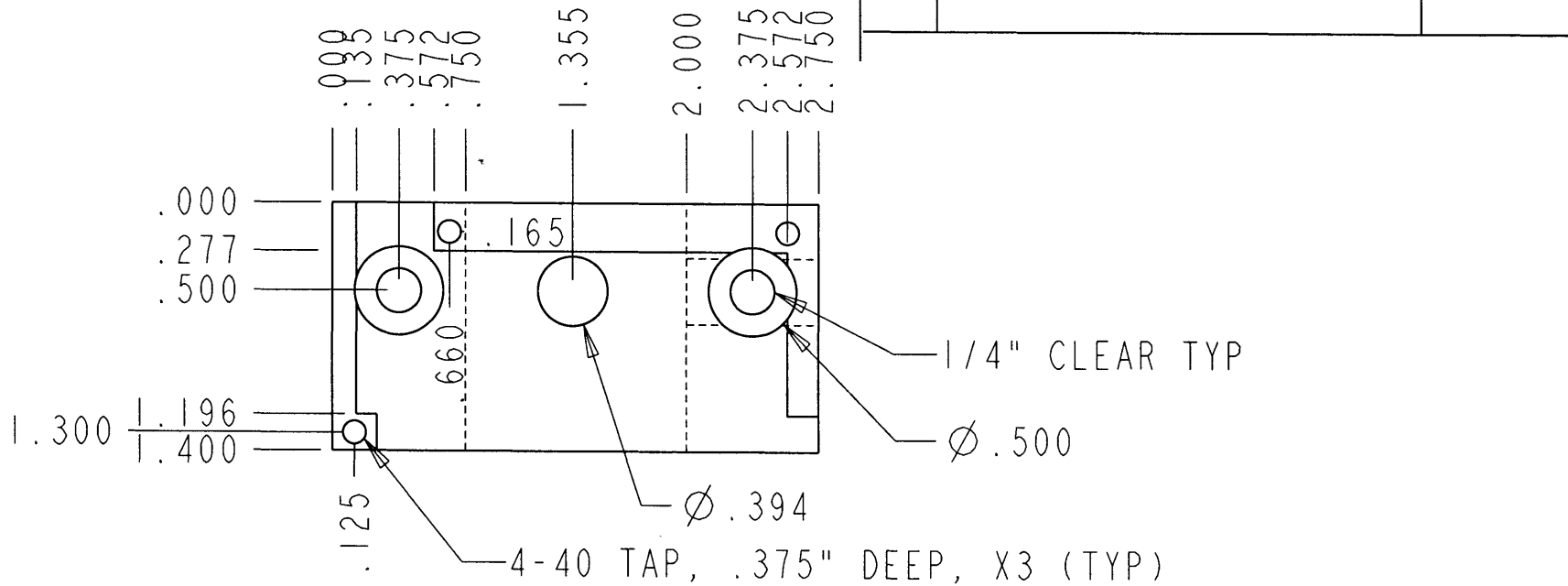

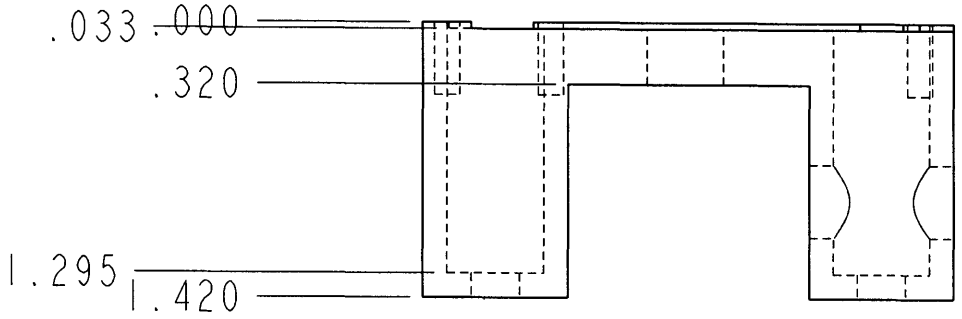

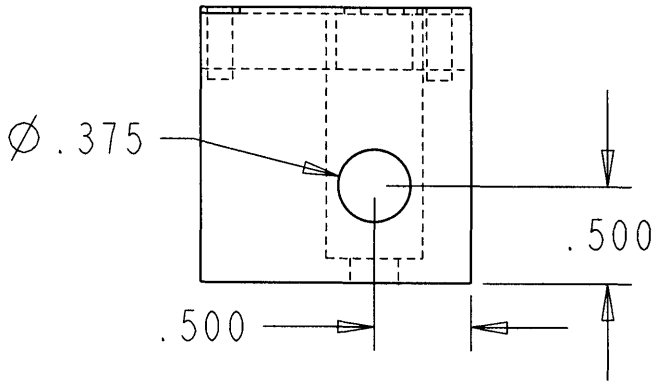

DEBURR EDGES
1/16" DIA. RELIEF CUT
ON INSIDE CORNERS)
QTY: 1

INTEGRATED PKG HOLDER
MATERIAL: SUPER INVAR
4/22/02
JAMES WHITE

PRECISION ENGINEERING RESEARCH GROUP
MIT RM. 3-438A
617-258-0726

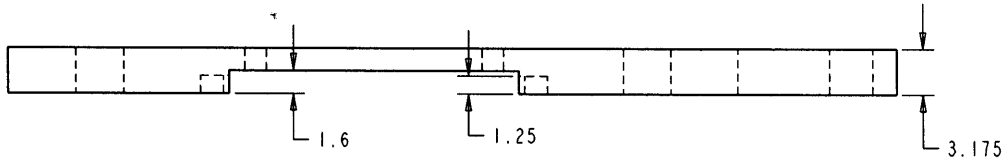

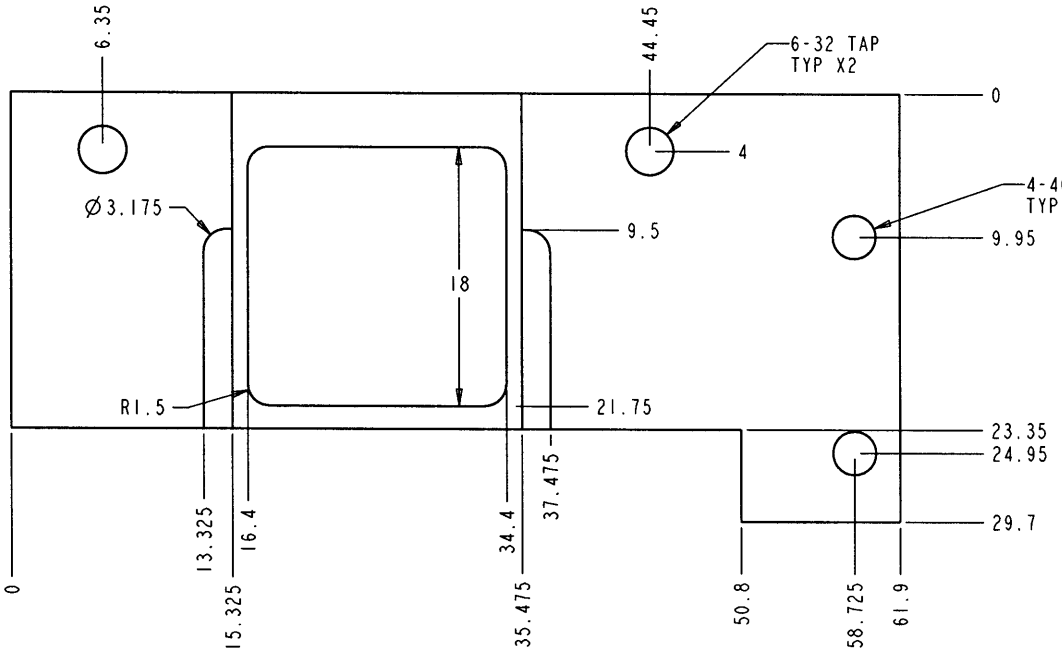

SCALE 4.000

DEBURR ALL EDGES
QTY: 1

NANOGATE BASE KOVAR 4/22/02 JAMES WHITE	P E R G MIT RM. 3-438A 617-258-0726

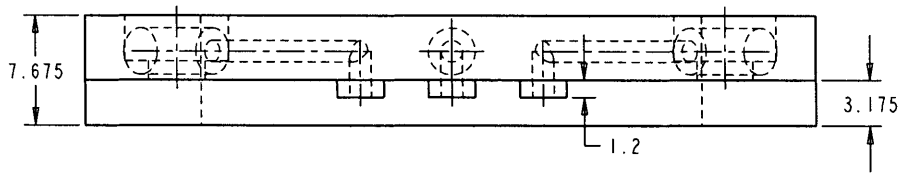

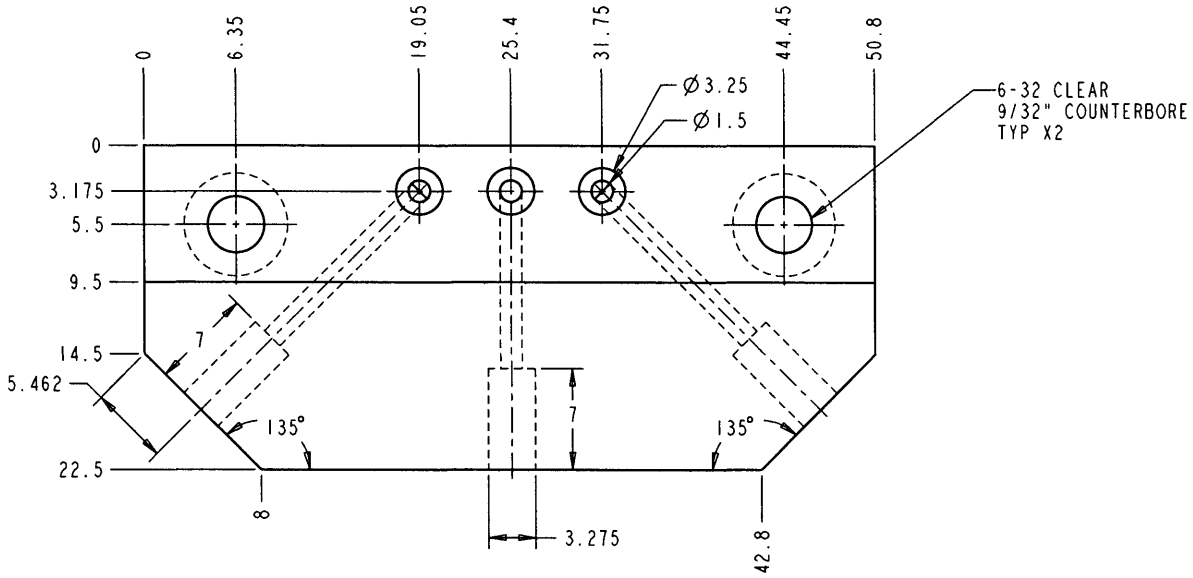

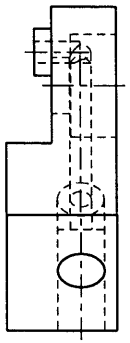

ALL DIMENSIONS MM
QTY: 1

NANOGATE MANIFOLD 4 MATERIAL: KOVAR 5/2/02 JAMES WHITE	PRECISION ENGINEERING RESEARCH GROUP MIT RM. 3-438A 617-258-0726

SCALE 4.000

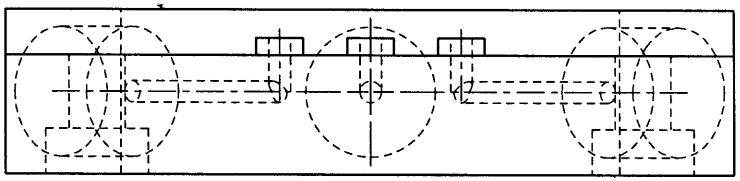

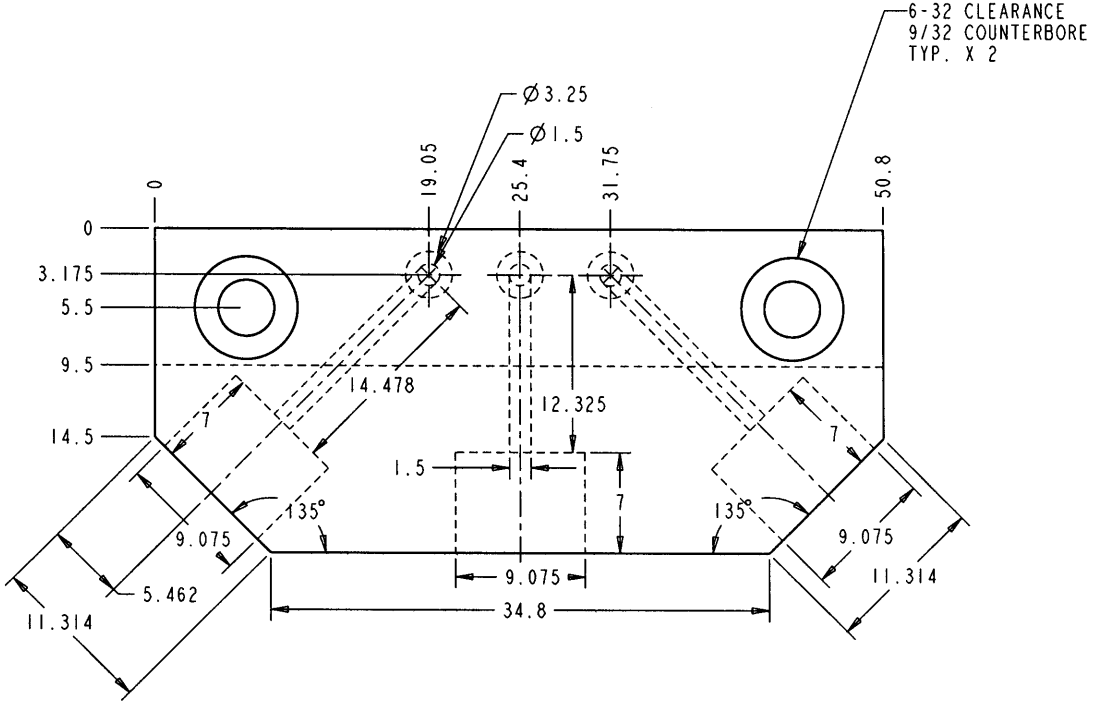

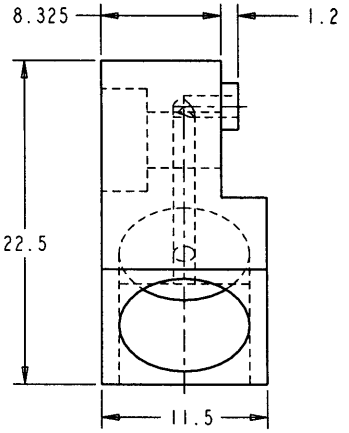

SCALE 4.000

NANOGATE MANIFOLD 3 MATERIAL: KOVAR 4/22/02 JAMES WHITE	PRECISION ENGINEERING RESEARCH GROUP MIT RM. 3-438A 617-258-0726

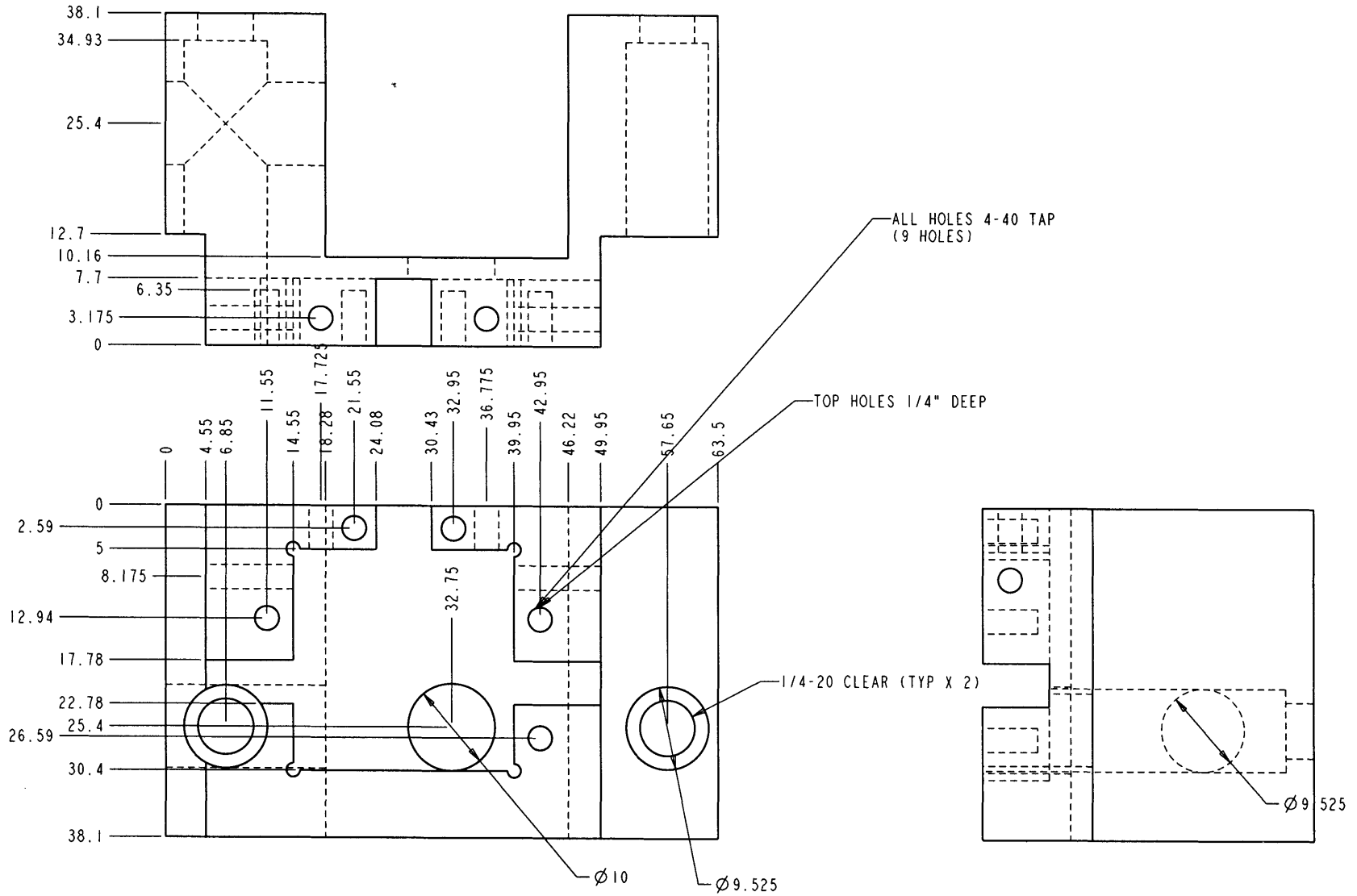

SCALE 3.000

JAMES WHITE
7/30/2002
617-258-0726
MATERIAL: SUPER INVAR
QTY: 1
INVAR BASE THICK PYREX

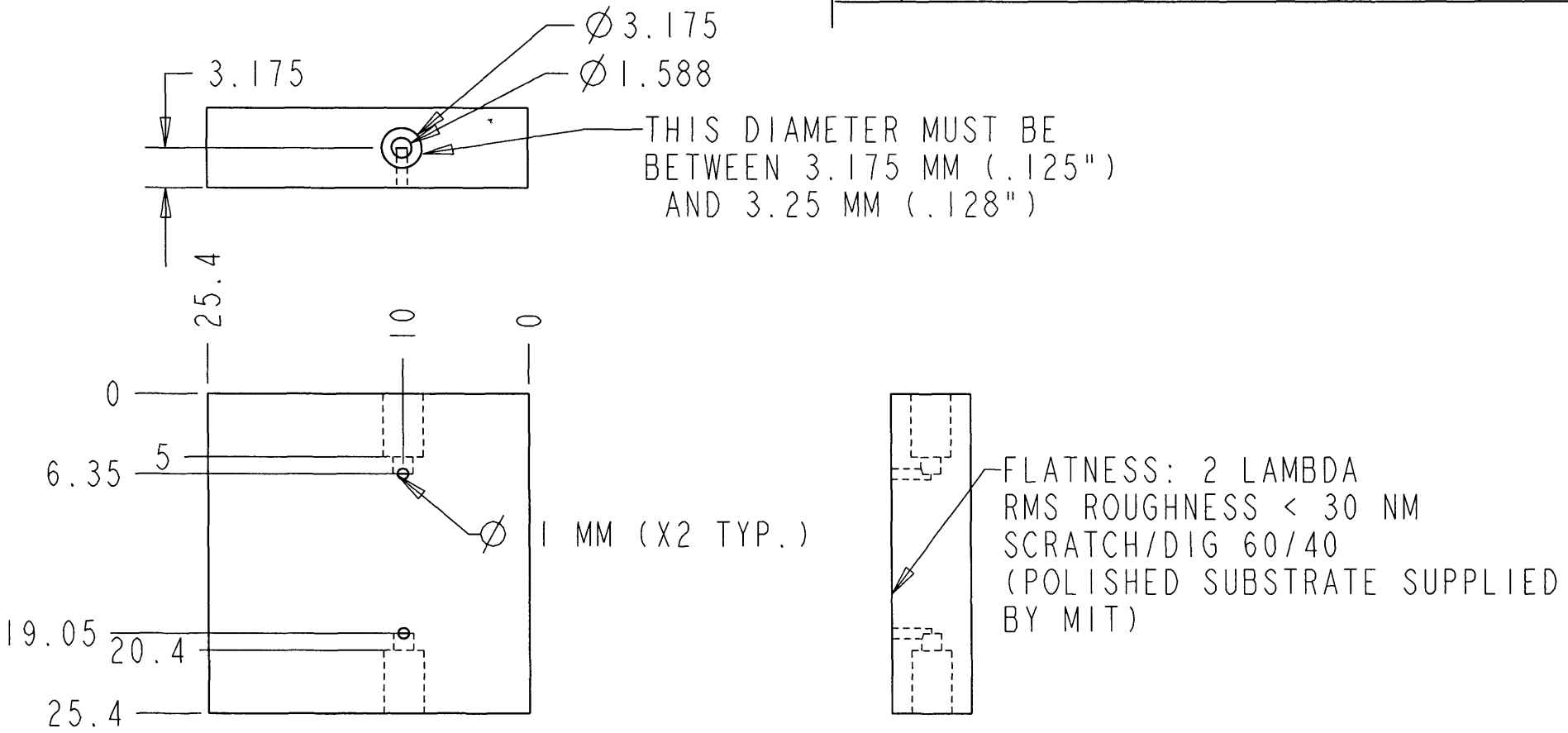

JAMES WHITE TWO PORT PYREX BASE ALL DIMENSIONS MM NOM. TOL. .1 MM	PRECISION ENGINEERING RESEARCH GROUP
	MIT RM. 3-438A 77 MASS. AVE, CAMBRIDGE MA 02139 617-258-0726

SCALE 2.000

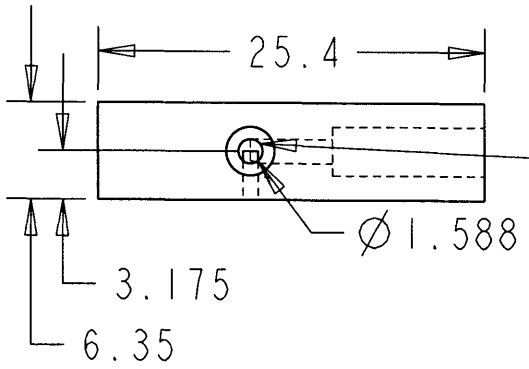

THIS DIAMETER MUST BE
BETWEEN 3.175 MM (.125")
AND 3.25 MM (.128")

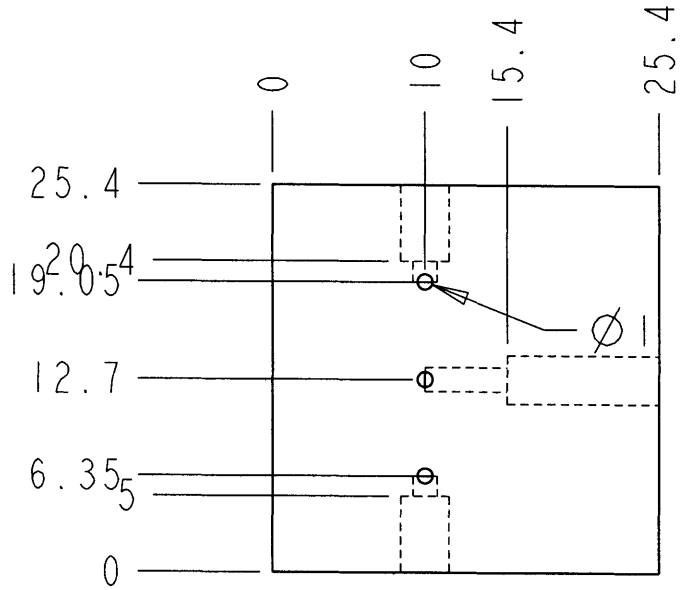

FLATNESS: LAMBDA / 2
RMS ROUGHNESS < 20 NM
SCRATCH/DIG 60/40
(POLISHED SUBSTRATE PROVIDED)

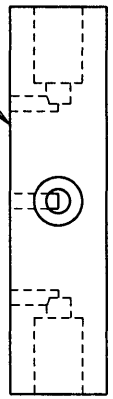

JAMES WHITE
THREE PORT PYREX BASE
ALL DIMENSIONS MM
NOM. TOL. .1 MM

PRECISION ENGINEERING RESEARCH GROUP
MIT RM. 3-438A
77 MASS. AVE, CAMBRIDGE MA 02139
617-258-0726

SCALE 2.000